Aerodynamic Analysis of a Scramjet Inlet and Isolator

Inês Micaela da Costa Cardoso

Thesis to obtain the Master of Science Degree in

Aerospace Engineering

Supervisor: Prof. Mário António Prazeres Lino da Silva

Examination Committee

Chairperson: Prof. Filipe Szolnoky Ramos Pinto Cunha
Supervisor: Prof. Mário António Prazeres Lino da Silva
Member of the Committee: Prof. José Carlos Fernandes Pereira

January 2021

“Study hard what interests you the most in the most undisciplined,
irreverent and original manner possible.”
- Richard Feynman

Declaration

I declare that this document is an original work of my own authorship and that it fulfills all the requirements of the Code of Conduct and Good Practices of the Universidade de Lisboa.

Acknowledgments

First of all, I would like to thank my supervisor, Professor Mário Lino, for motivating me to study the fascinating topic of scramjet propulsion. I would also like to express my sincere gratitude to Duarte Gonçalves, who continuously guided me through the usage of SPARK and never failed to answer a request for help. There are also certainly a handful of Professors I have encountered in my academic life who have pushed me towards Physics, even when I thought I wasn't at all gifted in that subject. To those, I would also like to leave a thankful note.

Secondly, I would like to thank my parents, who not only always pushed me to be my best, but also stood by me when, halfway through my degree in Mechanical Engineering, I decided to not only change degrees but Institution. In that note, I would also like to express my gratitude to my aunt, for her unwavering enthusiasm towards my academic path and my future prospects.

Thirdly, I would like to thank my most dearest friends, Nelson and Mariana. While they claim to not understand my eagerness to pursue an academic path, I cannot overlook their continuous advice and worry, as well as the endless times they put up with my frustrations. My greatest thank you and admiration goes to you.

Lastly, I leave a heartfelt note to the person who, through laughs and kind words, has turned such a stressful time into a rather pleasant journey.

Resumo

Motores *airbreathing*, como o motor de combustão supersónica (scramjet), apresentam uma solução mais sustentável para voo hipersónico que os motores de foguete, visto que não precisam de transportar oxidante a bordo. Neste trabalho utilizou-se o código CFD SPARK, mantido pelo Instituto de Plasmas e Fusão Nuclear, para estudar o sistema de compressão de um scramjet, desenhado para um ponto de trajetória a Mach 10. A pré-análise de um caso de estudo bidimensional da literatura mostrou discrepâncias em termos da pressão obtida com recurso ao SPARK e a apresentada da literatura, porém o campo de escoamento obtido foi semelhante. Para além disso verificou-se que temperaturas de parede mais baixas beneficiam o desempenho, enquanto que uma parede adiabática conduz a temperaturas excessivas. Mostrou-se ainda que a dissociação química pode ser negligenciada, mas que o não equilíbrio térmico existe e afeta moderadamente o desempenho. Fizeram-se estudos semelhantes para uma geometria axisimétrica com o mesmo rácio de compressão e contração, tendo sido retirada a conclusão de que o desempenho é menor para esta geometria. Um estudo paramétrico foi ainda efetuado por forma a estabelecer a afetação do número de rampas, do rácio de compressão, do comprimento do *isolator*, do rácio de contração e ainda da forma do canto de expansão no desempenho, tendo-se verificado a ocorrência de *unstart* para o caso bidimensional com maior rácio de contração. Simularam-se ainda ambas as configurações a um ponto de trajetória de Mach 7, tendo-se verificado que é possível operar neste regime, porém com menor desempenho do veículo.

Palavras-chave: Hipersónico, Scramjet, Mecânica de Fluídos Computacional, Aerotermodinâmica

Abstract

Airbreathing engines, such as the supersonic combustion ramjet (or scramjet), promise a more sustainable solution for hypersonic flight than rocket powered engines, simply because they do not need to carry on-board oxidizer. This work uses the hypersonic CFD SPARK code, maintained by the Institute for Plasmas and Nuclear Fusion, to study the compression system of a scramjet engine designed for a trajectory point of Mach 10. An initial pre-analysis of a two-dimensional case study from the literature evidenced some discrepancies between the obtained values for pressure and those presented therein, but with a similar overall behaviour of the flow. It was found that lower wall temperatures benefit performance, whereas an adiabatic wall leads to impractically high temperatures. Chemical dissociation was found to be negligible, while the deployment of a two-temperature model showed that thermal non-equilibrium exists in a scramjet compression system, moderately impacting performance. Similar studies were then conducted for an axisymmetric geometry with the same compression and contraction ratios, with the main conclusion being that performance was worse for the axisymmetric case. Geometry parametric studies were conducted to verify how the number of ramps, the compression ratio, the isolator length, the contraction ratio and the expansion corner edge affected performance. An increased contraction ratio was found to favour inlet unstart for the two-dimensional geometry. Simulations at a trajectory point of Mach 7 were also conducted for both configurations and showed that it is possible to have a started inlet in this off-nominal regime, albeit at a decreased performance.

Keywords: Hypersonic, Scramjet, Computational Fluid Dynamics, Aerothermodynamics

Contents

Declaration . . . v
Acknowledgments . . . vii
Resumo . . . ix
Abstract . . . xi
List of Tables . . . xvii
List of Figures . . . xix
Nomenclature . . . xxiii
Glossary and Acronyms . . . xxvii

1 Introduction 1
- 1.1 Hypersonic Airbreathing Propulsion . . . 1
- 1.2 Historical Overview . . . 1
- 1.3 The Scramjet Engine . . . 3
  - 1.3.1 Compression System . . . 4
  - 1.3.2 Isolator . . . 5
  - 1.3.3 Combustion chamber . . . 5
  - 1.3.4 Expansion system . . . 5
- 1.4 Objectives . . . 6
- 1.5 Thesis Outline . . . 6

2 Literature Review 9
- 2.1 Scramjet Operating Conditions . . . 9
  - 2.1.1 Trajectory Point . . . 10
- 2.2 Case Study . . . 11
  - 2.2.1 Axisymmetric compression system . . . 12

3 Mathematical Formulation 13
- 3.1 Non-equilibrium Chemically Reacting Flow . . . 13
  - 3.1.1 Gas Mixture . . . 13
  - 3.1.2 Chemical Non-equilibrium . . . 14
  - 3.1.3 Thermal Non-equilibrium . . . 14
  - 3.1.4 Governing Equations . . . 16

3.1.5 Transport Coefficients . . . 17
3.2 Oblique Shock Wave Theory . . . 19
3.2.1 Application to axisymmetric flow . . . 20
3.3 Compression System Performance . . . 21

4 Numerical Implementation 25
4.1 Computational Fluid Dynamics Solver . . . 25
4.1.1 SPARK Input File . . . 26
4.2 Boundary Conditions . . . 26
4.2.1 Upstream Conditions . . . 26
4.2.2 Wall Boundary Condition . . . 26
4.2.3 Outlet Boundary Condition . . . 27
4.3 Mesh and Convergence Study . . . 27
4.3.1 Grid Convergence Study . . . 28
4.3.2 Axisymmetric geometry . . . 29
4.4 Simulation Strategy . . . 31
4.5 Flow Visualization and Data Treatment . . . 32
4.6 Model Shortfalls . . . 32

5 Results 35
5.1 Two-dimensional Configuration . . . 35
5.1.1 Frozen Flow solution . . . 35
5.1.2 Impact of Wall Temperature . . . 38
5.1.3 Non-Equilibrium Chemically Reacting Flow Solution . . . 40
5.2 Axisymmetric Configuration . . . 43
5.2.1 Frozen Flow solution . . . 43
5.2.2 Non-Equilibrium Chemically Reacting Flow Solution . . . 45
5.3 Geometry Parametric Study . . . 47
5.3.1 Two-Dimensional Configuration . . . 47
5.3.2 Axisymmetric Configuration . . . 56
5.4 Off-Design Conditions . . . 59
5.4.1 Off-design trajectory point: Mach 7 . . . 59

6 Conclusions 67
6.1 Achievements . . . 67
6.2 Future Work . . . 69

Bibliography 71

A Physical Models **75**

A.1 Thermodynamic Relations 75

A.1.1 Gas Mixture 75

A.1.2 Equation of State 76

A.1.3 Internal Energy 76

A.1.4 Enthalpy 77

A.1.5 Specific Heats 77

A.1.6 Gas Constants 79

List of Tables

2.1 Baseline design for the two-dimensional compression system. 12

3.1 Multi-temperature models. 16
3.2 Definition of the dissipative fluxes, corresponding gradients and transport coefficients. . . 18

4.1 Upstream conditions at an altitude of 33km and a dynamic pressure of 50kPa. 26
4.2 Design parameters for the baseline axisymmetric compression system. 30

5.1 Performance parameters obtained for the frozen flow solution for the two-dimensional configuration. 38
5.2 Performance parameters obtained for the considered wall temperatures for the two-dimensional configuration. 39
5.3 Performance parameters obtained for the reactive flow solution for the two-dimensional configuration. 41
5.4 Performance parameters obtained for the thermal equilibrium and non-equilibrium solutions for the two-dimensional configuration. 42
5.5 Performance parameters obtained for the two-dimensional and axisymmetric frozen flow solutions. 44
5.6 Performance parameters obtained for the thermal equilibrium and non-equilibrium solutions for the axisymmetric configuration. 47
5.7 Design parameters for a two-dimensional compression system with three ramps. 47
5.8 Performance parameters obtained for the different number of ramps, for the two-dimensional configuration. 49
5.9 Design parameters for a two-dimensional compression system with a compression ratio of 5 across each of the first two oblique shock waves. 49
5.10 Performance parameters obtained for the different number of ramps, for the two-dimensional configuration. 50
5.11 Performance parameters obtained for the different isolator lengths, for the two-dimensional configuration. 52
5.12 Design parameters for a compression system with a contraction ratio of 15, for the two-dimensional configuration. 53

5.13 Performance parameters obtained for different expansion corners, for the two-dimensional configuration. 56
5.14 Design parameters for the considered cowl heights for the axisymmetric configuration. . . 57
5.15 Performance parameters for the considered cowl heights for the axisymmetric configuration. 58
5.16 Upstream conditions for off-design trajectory points, for freestream Mach numbers ranging from 6 to 10, for a dynamic pressure of 50kPa. 59
5.17 Performance parameters obtained for different trajectory points, for the adapted grid, for the two-dimensional configuration. 62
5.18 Performance parameters obtained for different trajectory points, for the adapted grid, for the axisymmetric configuration. 65

List of Figures

1.1 Ramjet development in the first half of the 20th century. 2
1.2 Development of scramjet technology in the 20th and 21st centuries. 2
1.3 Stages of a ramjet and scramjet engines. 3
1.4 Operating conditions of a scramjet inlet. 4
1.5 Schematics of the different compression systems. 4
1.6 Structure of an oblique shock wave train inside an isolator. 5

2.1 Characteristic flight trajectories for different aerospace vehicles 9
2.2 Flight corridor for an hypersonic airbreathing engine as function of Mach number, altitude and dynamic pressure 10
2.3 Schematics of a mixed compression system 12

3.1 Thermal energy modes. 15
3.2 Schematic of the change in the velocity components, when the flow crosses an arbitrary oblique shock wave. 19

4.1 Particle recombination according to wall catalycity. 27
4.2 Two-dimensional compression system mesh and boundary conditions. 28
4.3 Velocity and temperature profiles as a function of the normal distance from the lower wall, at the isolator exit, for the different two-dimensional grid resolutions considered. 28
4.4 Pressure and temperature profiles as a function of the vertical distance from the second ramp wall, at x=1.1m, for the different two-dimensional grid resolutions considered. 29
4.5 Velocity and temperature profiles as a function of the normal distance from the lower wall, at the isolator exit, for the different axisymmetric grid resolutions considered. 30
4.6 Pressure and temperature profiles as a function of the vertical distance from the second ramp wall, at x=1.2m, for the different axisymmetric grid resolutions considered. 31
4.7 Residual root-mean-square and CFL condition as a function of the iteration number . . . 31

5.1 Pressure, density and temperature fields obtained for the viscous (Navier-Stokes) frozen-flow simulation of the two-dimensional compression system. 36
5.2 Pressure variations across the first two oblique shock waves and at the cowl tip and pressure profile at the isolator exit, for the two-dimensional configuration. 37

5.3 Density field obtained for the inviscid frozen flow simulation, for the two-dimensional configuration. 38
5.4 Pressure and temperature profiles at the isolator exit for different wall boundary conditions, for the two-dimensional configuration. 39
5.5 Temperature field obtained for the adiabatic wall boundary condition, for the two-dimensional configuration. 39
5.6 O and NO mass fraction distribution at the isolator exit, for the the two-dimensional configuration. 40
5.7 Pressure and temperature profiles of the reactive flow solution at the isolator exit compared against the frozen flow solution, for the two-dimensional configuration. 41
5.8 Pressure and temperature profiles of the reactive flow solution, at the isolator exit, compared against the case where thermal non-equilibrium was considered, for the two-dimensional configuration. 42
5.9 Pressure, density and temperature fields obtained for the viscous (Navier-Stokes) frozen-flow simulation of the axisymmetric compression system. 43
5.10 Comparison of the pressure and temperature profiles at the isolator exit for the two-dimensional and axisymmetric configurations. 44
5.11 O and NO mass fraction distribution at the isolator exit for the axisymmetric configuration. 45
5.12 Pressure and temperature profiles of the reactive flow solution compared against the frozen flow solution for the axisymmetric configuration. 45
5.13 Pressure and temperature profiles of the reactive flow solution in thermal equilibrium at the isolator exit compared against the case where thermal non-equilibrium was considered for the axisymmetric configuration. 46
5.14 Detail of the pressure field obtained for the two-dimensional three ramp compression system, at the isolator entry. 48
5.15 Pressure and temperature profiles at the isolator exit, for different number of ramps, for the two-dimensional configuration. 48
5.16 Pressure and temperature profiles at the isolator exit, for different compression ratios, for the two-dimensional configuration. 50
5.17 Flow separation and recirculation zones at the isolator exit for different compression ratios, for the two-dimensional configuration. 50
5.18 Pressure variations along the centreline of the isolator, at y=0.2375m, for an isolator length of 1m, for the two-dimensional configuration. 51
5.19 Pressure and temperature profiles at the isolator exit, for different isolator lengths, for the two-dimensional configuration. 52
5.20 Schematics of the oblique shock wave structure for different contraction ratios, for the two-dimensional geometry (not to scale). 53
5.21 Detail of the pressure and temperature fields, at the isolator entry, over one time period, for a two-dimensional configuration with a contraction ratio of 15. 54

5.22 Detail of the velocity field, at the isolator entry, with and without an expansion corner edge, for the two-dimensional configuration. 55
5.23 Pressure and temperature profiles at the isolator exit, with and without an expansion corner edge, for the two-dimensional configuration. 55
5.24 Pressure variations along the centreline of the isolator for different contraction ratios, for the axisymmetric configuration. 57
5.25 Pressure and temperature profiles at the isolator exit, for different compression ratios used in the axisymmetric geometry. 57
5.26 Flow separation and recirculation zones at the isolator entry for different contraction ratios. 58
5.27 Adapted grid configuration used to assess performance at different freestream conditions, for the two-dimensional configuration. 60
5.28 Pressure and temperature profiles, at x=1.1m, for the baseline and adapted grid for the two-dimensional configuration. 60
5.29 Pressure and temperature profiles at the isolator exit for the baseline and adapted grid, for the two-dimensional configuration. 60
5.30 Pressure, density and temperature fields obtained for the viscous (Navier-Stokes) frozen-flow simulation of the two-dimensional compression system, at a trajectory point of Mach 7. 61
5.31 Pressure and temperature profiles at the isolator exit, for different trajectory points, for the two-dimensional configuration, obtained from the adapted grid. 62
5.32 Pressure and temperature profiles, at x = 1.2m, for the baseline and adapted grid, for the axisymmetric configuration. 63
5.33 Pressure and temperature profiles at the isolator exit for the baseline and adapted grid, for the axisymmetric configuration. 63
5.34 Pressure, density and temperature fields obtained for the viscous (Navier-Stokes) frozen-flow simulation of the axisymmetric compression system, at a trajectory point of Mach 7. 64
5.35 Pressure and temperature profiles at the isolator exit, for different trajectory points, for the axisymmetric configuration, obtained from the adapted grid. 65

ϑ

Nomenclature

Greek symbols

β	Oblique shock wave angle.
η_c	Compression efficiency.
η_KE	Kinetic energy efficiency.
ε	Particle energy.
ε_0	Species zero-point energy.
γ	Ratio of specific heats.
μ	Dynamic viscosity coefficient.
ν'	Stoichiometric coefficient associated with a reactant.
ν''	Stoichiometric coefficient associated with a product.
$\dot{\Omega}$	Energy exchange source term.
ω_e	Fundamental vibrational frequency.
$\dot{\omega}$	Rate of formation or consumption.
ϕ	Scale factor used in the Wilke/Blottner/Eucken model.
π_c	Total pressure ratio.
φ	Azimuthal angle.
ρ	Density.
$[\tau]$	Viscous stress tensor.
θ	Flow turn angle.
ϑ	Polar angle.

Roman symbols

A	Cross sectional area.

c	Mass fraction.
c_p	Specific heat at constant pressure.
c_v	Specific heat at constant volume.
D	Mass diffusion coefficient.
h	Enthalpy or Planck’s constant.
$(\Delta \mathrm{h}_s)^\circ$	Effective zero-point energy of species s.
H	Compression system freestream capture height.
h	Compression system throat height.
$[\mathrm{I}]$	Identity matrix.
J	Mass diffusion flux vector.
k	Thermal conductivity.
k_B	Boltzmann constant.
k_b	Backward reaction rate constant.
k_f	Forward reaction rate constant.
Kn	Knudsen number.
L	Isolator length.
$\dot{m}$	Mass flow rate.
M	Molar mass.
Ma	Mach number.
N	Number of particles.
N_A	Avogrado’s constant.
n	Number of moles.
p	Pressure.
p_t	Total or stagnation pressure.
$\mathbf{q}$	Heat-flux vector.
q	Dynamic pressure.
R	Universal gas constant.
r	Radial coordinate.

T	Temperature.
t	Time.
$\mathbf{u}$	Velocity vector.
u	Velocity magnitude.
V	Volume.
$[X]$	Species concentration.
X'	Reactant.
X''	Product.
x	Mole fraction.

Subscripts

c	Conditions at combustor entry (or isolator exit).
el	Electronic energy mode.
∞	Freestream conditions.
k	Thermal energy mode index.
n	Normal component.
R	Radiative term.
r	Reaction index.
r	Radial component.
rot	Rotational energy mode.
s	Species index.
ϑ	Angular component.
t	Tangential component.
trans	Translational energy mode.
vib	Vibrational energy mode.

Superscripts

T	Transpose.

Glossary and Acronyms

CFD	Computational Fluid Dynamics is a branch of fluid mechanics that uses numerical methods and algorithms to solve problems that involve fluid flows.
CFL	The Courant–Friedrichs–Lewy condition is a necessary condition for convergence while solving certain partial differential equations numerically.
HRE	The Hypersonic Research Engine was a project conducted by the National Aeronautics and Space Administration with the goal of designing, developing, and constructing a high-performance hypersonic research ramjet/scramjet engine for flight tests over the speed range of Mach 4 to 8.
IPFN	The Institute for Plasmas and Nuclear Fusion, or Instituto de Plasmas e Fusão Nuclear, is a research unit of Instituto Superior Técnico.
NASA	The National Aeronautics and Space Administration is an independent agency of the U.S. Federal Government responsible for the civilian space program, as well as aeronautics and space research.
SPARK	The Software Package for Aerothermodynamics, Radiation and Kinetics is a Computational Fluid Dynamics code for hypersonic flow, maintained by the University of Illinois and by the Institute for Plasmas and Nuclear Fusion, at Instituto Superior Técnico.

Chapter 1

Introduction

This chapter contextualizes this thesis by introducing the concept and importance of an airbreathing propulsion vehicle, presenting an historical overview on the topic, and outlining the objectives of the present work.

1.1 Hypersonic Airbreathing Propulsion

Rule of thumb dictates that hypersonic flow is that at which the Mach number Ma is greater than 5. However, because there is no clear transition from supersonic to hypersonic flow, this regime is better described by the presence of high pressure and temperature gradients, thin shock layers and viscous interaction. Moreover, as speed increases, high-temperature effects arise, and with it physical phenomena such as chemical dissociation and ionization, as well as vibrational and chemical non-equilibrium, occur [1].

Among the vehicles capable of travelling in such a complex flow field, those equipped with airbreathing propulsion present a more sustainable choice for hypersonic flight than rocket powered engines. As the name suggests, these vehicles use the enveloping atmospheric air as oxidizer for the combustion processes, generating thrust [2], and thus eliminating the need to carry an on-board oxidizer and significantly increasing payload capabilities. While this is not an entirely new concept, having seen its successful application for both supersonic and hypersonic flight, faster than sound travel, as well as space access, is still not available for the common passenger. This can be explained by the fact that these vehicles typically require additional propulsive systems to reach their operating range, resulting in a complicated aggregation of dependable components, and an overall reduction of reliability.

1.2 Historical Overview

In 1913, René Lorin first introduced the concept of a ramjet when he recognized the possibility of using ram pressure, the pressure exerted by a fluid on a moving body, to propel a vehicle [2]. Because this means no thrust can be produced while the vehicle is standing still, its application to subsonic speeds was limited and the concept was, at the time, disregarded. In fact, it wasn't until 1949, after the end of the second world war, that René Leduc, flew the Leduc 010, the first ramjet powered aircraft.

While Leduc's aircraft showed promise for flight at higher speeds, it still needed to be piggybacked on a parent aircraft to take off (figure 1.1a). To avoid this complication, the Nord Aviation's Griffon, built shortly after, was equipped with a dual-mode engine: half turbojet, half ramjet (figure 1.1b).

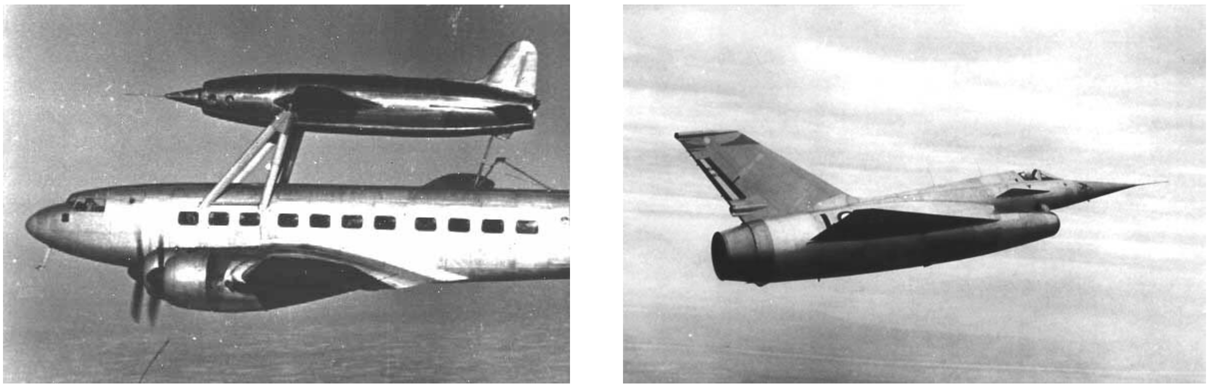

(a) The Leduc 010 mounted atop its parent aircraft [3]

(b) Nord Aviation's Griffon 1500 [4]

Figure 1.1: Ramjet development in the first half of the 20th century.

Despite their successful flights, both the Leduc and Griffon series were abandoned in the early 1960s due to overheating, and ramjet technology was mainly studied for military purposes, with focus in the development of supersonic missiles.

Around the same time period, ramjet propulsion was deemed unfit for higher hypersonic velocities, due to the impracticality of decelerating air to subsonic speeds. This led to the creation of programs such as the National Aeronautics and Space Administration's (NASA's) Hypersonic Research Engine (HRE), founded in 1964, which focused on the development of a ramjet engine capable of supersonic combustion (scramjet).

(a) The X-15A-2 research plane. Adapted from [5]

(b) Boeing X-51A concept art [6]

Figure 1.2: Development of scramjet technology in the 20th and 21st centuries.

Fry [7] describes the HRE as the most extensive of the early scramjet development programs in the United States. The goal of this project was to develop a complete hydrogen-fueled, flight-weight scramjet engine, that was to be tested on board the rocket powered X-15A-2 research plane (figure 1.2a). While the X-15 program was terminated before any flight-tests were conducted, comprehensive data was collected on scramjet inlet and combustor performance for flight Mach numbers 5, 6 and 7.

Several years passed between the X-15 program and the first scramjet powered flight, with adversities such as the difficulty of igniting and burning hydrocarbons and the necessity of a cooling system becoming more evident through the years. Finally, on July 30th 2002, the University of Queensland in Australia conducted, under the HyShot flight program, the first successful flight where supersonic combustion was observed [8]. More recently, in 2010, the Boeing X-51 Waverider performed the longest scramjet-powered flight, with fuel burn lasting for over 200 seconds (figure 1.2b).

Interest in hypersonic airbreathing propulsion and, particularly, in scramjet technology continues to this day, with tools such as Computational Fluid Dynamics (CFD) playing a major a role in predicting these vehicles' behaviour at high hypersonic velocities.

1.3 The Scramjet Engine

The present section serves to describe the flowpath inside a scramjet engine. Because the scramjet is a direct descendant of the ramjet, working under the same principles, the schematic of ramjet engine is firstly described and the geometrical changes necessary for supersonic combustion are highlighted.

A ramjet engine (figure 1.3a) stands apart from a turbine engine, such as the turbojet, due to the absence of moving parts. Instead, a diffuser compresses the freestream air from supersonic to subsonic speeds, by means of a normal shock wave system, resulting in an increase of both ram pressure and temperature. Fuel is then mixed with the compressed air and subsonic combustion takes place. Finally the high temperature exhaust is accelerated through a nozzle, generating thrust.

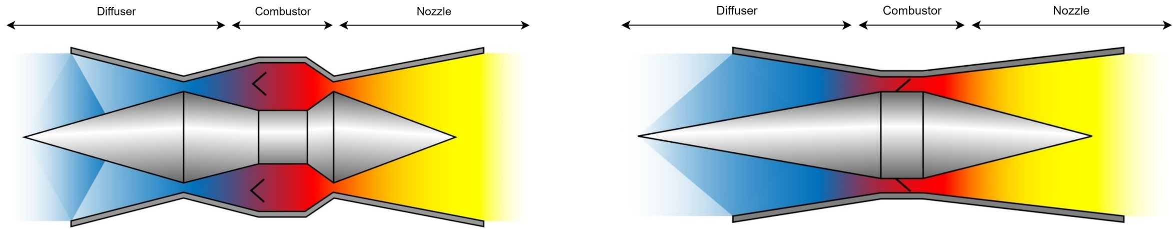

(a) Schematic of a ramjet engine

(b) Schematic of a scramjet engine

Figure 1.3: Stages of a ramjet (a) and scramjet (b) engines. Adapted from [9].

As speed is increased above Mach 6, the airflow temperature becomes so high, that dissociation begins to occur, causing a significant reduction in the amount of energy available to generate thrust. Because of this, it is no longer advantageous to decelerate the supersonic freestream velocity to the subsonic regime, and the resulting alternative is to slow the flow to an acceptable supersonic speed, where combustion takes place. Figure 1.3b presents the schematic of a scramjet engine, where the absence of a physical throat evidences that the flow is never subsonic.

1.3.1 Compression System

The compression components have the role of providing, at the combustor entrance, the conditions necessary for efficient fuel combustion, with minimum aerodynamic losses. This is achieved through a series of oblique shock waves, that, when operating at the Mach number they were designed for (figure 1.4a), all converge onto the tip of the engine cowl, meeting the designated *shock-on-lip* condition. Figure 1.4 presents the different operating conditions, while figure 1.5 presents the schematics of the different types of compression systems.

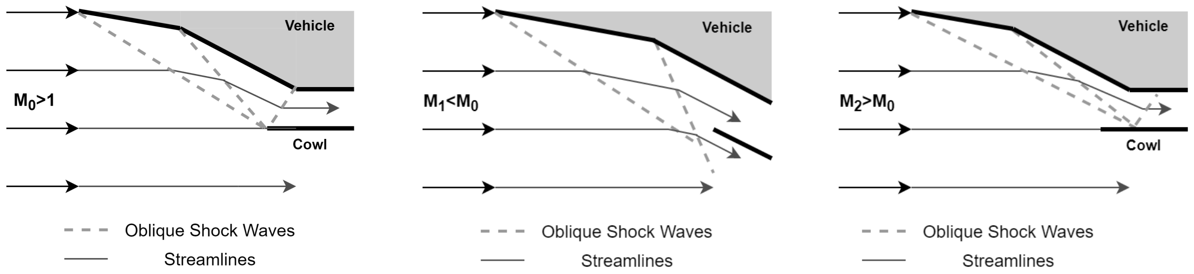
Vehicle
$M_0>1$
Cowl
Oblique Shock Waves
Streamlines
Vehicle
$M_1<M_0$
Oblique Shock Waves
Streamlines
Vehicle
$M_2>M_0$
Cowl
Oblique Shock Waves
Streamlines

(a) Shock-on-lip ($M_0 = M_{design}$)   (b) Flow spillage ($M_0 < M_{design}$)   (c) Flow instability ($M_0 > M_{design}$)

Figure 1.4: Operating conditions of a scramjet inlet. Adapted from [2].

External compression systems (figure 1.5a) are self-starting and offer the possibility to operate at Mach numbers which are smaller than that for which they were designed for. This is accomplished through the spillage of flow when the shock-on-lip condition is not met (figure 1.4b), and is a desirable feature, since it offers a wider operational range. On the other hand, because of the angle between the freestream flow direction and the lip, these systems have high cowl drag.

In the case of internal compression systems (figure 1.5b), a series of symmetrical oblique shock waves is formed, that results in a uniform and parallel internal flow, and allows for a shorter axial length than that of external compression systems. Spillage is, however, not possible for internal compression, which means that, for a fixed geometry, these systems cannot stray far from their design Mach number.

Mixed compression systems (figure 1.5c) are usually preferred, since they take advantage of both internal and external compression, and result in a design that can operate below the design Mach number, with significantly less cowl drag than that of external compression systems. They present, however, an axial length that must be greater than that of the other two types of compression systems.

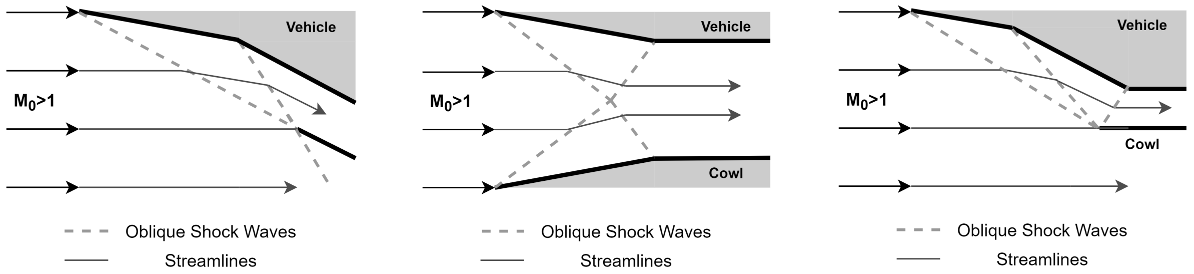
Vehicle
$M_0>1$
Oblique Shock Waves
Streamlines
Vehicle
$M_0>1$
Cowl
Oblique Shock Waves
Streamlines
Vehicle
$M_0>1$
Cowl
Oblique Shock Waves
Streamlines

(a) External compression system   (b) Internal compression system   (c) Mixed compression system

Figure 1.5: Schematics of the different compression systems. Adapted from [2, 10].

It is important to notice that neither of the compression systems presented above should operate above their design Mach number (figure 1.4c), since this operating condition results in high heat loads and flow instabilities, thus presenting the risk of material failure [10].

1.3.2 Isolator

The isolator is a constant area diffuser placed between the compression system and the combustion chamber. Inside this component, pressure increases in a controlled manner by means of an oblique shock train that continuously interacts with the boundary layer (figure 1.6), allowing the flow to adjust to the back pressure imposed by the downstream components [2].

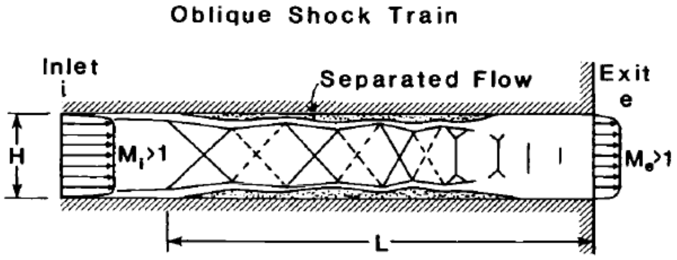

Figure 1.6: Structure of an oblique shock wave train inside an isolator [2].

The main consideration regarding this component is therefore that it should be long enough to contain the entire shock train and provide the necessary conditions for supersonic combustion to occur. As will be discussed in the following chapter, if these conditions are not met, the inlet will unstart. Furthermore, this component ultimately determines the combustor entry profiles. Reference [11] suggests that while there is little information regarding what constitutes an ideal combustor entry profile, an uniform profile is expected to aid in fueling.

1.3.3 Combustion chamber

As the air leaves the isolator it enters the combustion chamber. Here, fuel is injected, appropriate mixing is achieved, and supersonic combustion takes place, all of which must be accomplished within a reasonable length [2, 12].

Aside from requiring a feasible design, other challenges arise at this component. Namely, the short flow time of the mixture inside the burner leads to a difficulty in maintaining the flame, as well as, more often than not, to incomplete combustion. Properties of the airflow at the combustor entry, propellant, stoichiometry and method chosen for fuel injection can all greatly affect the amount of mixing and combustion that can be achieved, and therefore dictate engine performance.

1.3.4 Expansion system

At the expansion system, or nozzle, the exhaust is accelerated to high velocities, generating forward thrust. Not unlike the compression system, this component typically has an internal flow, that then continues to expand in the vehicle aftbody, in an unconfined external flow.

1.4 Objectives

As stated in 1.2, Computational Fluid Dynamics plays an important role in determining the behaviour of the flow within an hypersonic airbreathing vehicle. Therefore, the aim of this thesis was, first and foremost, to assess the capabilities of the Software Package for Aerothermodynamics, Radiation and Kinetics (SPARK) for predicting the flowpath within a scramjet compression system. This was achieved by comparing the results provided by SPARK against a case study present in the literature, at an operating point of Mach 10.

Having established a baseline methodology for correctly calculating the properties of the flow inside a scramjet diffuser, a series of other objectives were proposed, namely:

1. Assess the relative importance of non-equilibrium and high-temperature effects within the compression system;
2. Compare the performance of the two dimensional inlet present in the case study, with that of an axisymmetric inlet with the same pressure and area ratios;
3. Numerically assess the influence of the different geometric parameters on the behaviour of the flow within the compression system.

Lastly, operation at off-design conditions is also considered of importance to assure correct performance any vehicle, and the capability of the designed vehicle to operate at a trajectory point of Mach 7 was assessed.

1.5 Thesis Outline

The present document is organized into six main chapters. Chapter 1 introduced the concept of hypersonic airbreathing propulsion, presented an historical overview on the topic and described for the reader the several components that constitute a supersonic combustion ramjet.

Chapter 2 presents a review of the available literature, conducted to aid in the choice of a trajectory point of interest, determine the applied operating restrictions, and find a baseline case study to be replicated.

Chapter 3 presents to the reader the relevant mathematical formulation and physical models, necessary to solve the problem at hand.

Chapter 4 briefly describes the SPARK code, and then focuses on the numerical implementation of the problem, the mesh convergence study and the simulation strategy employed. Shortfalls to the modelled problem are also identified in this chapter.

Chapter 5 presents the obtained results, their interpretations, and guides the reader through the different geometric changes considered.

Lastly, chapter 6 concludes this work by identifying what was accomplished and by providing some recommendations for future work.

Chapter 2

Literature Review

The present chapter serves to map the literature surveyed to identify the flight conditions at which an hypersonic airbreathing vehicle is expected to operate. Additionally, a case study from the literature was identified as a baseline for the rest of the work developed.

2.1 Scramjet Operating Conditions

While literature states that scramjet operating limits range from Mach 4 to Mach 15 [7], Urzay [13] suggests that hypersonic cruising trajectories which take place at lower Mach numbers, ranging from 6 to 10, lead to more manageable loads (both thermal and mechanical), as well as reduced high temperature effects. Furthermore, Urzay states that, at speeds above Mach 10, the decrease in specific impulse with the freestream Mach number results in an increase of velocity per unit mass flow of propellant, that may no longer be advantageous. Lastly, Urzay shows that most mission profiles may be accomplished with a vehicle whose operating range is only as high as Mach 10. Figure 2.1 presents the characteristic flight trajectories for different aerospace vehicles.

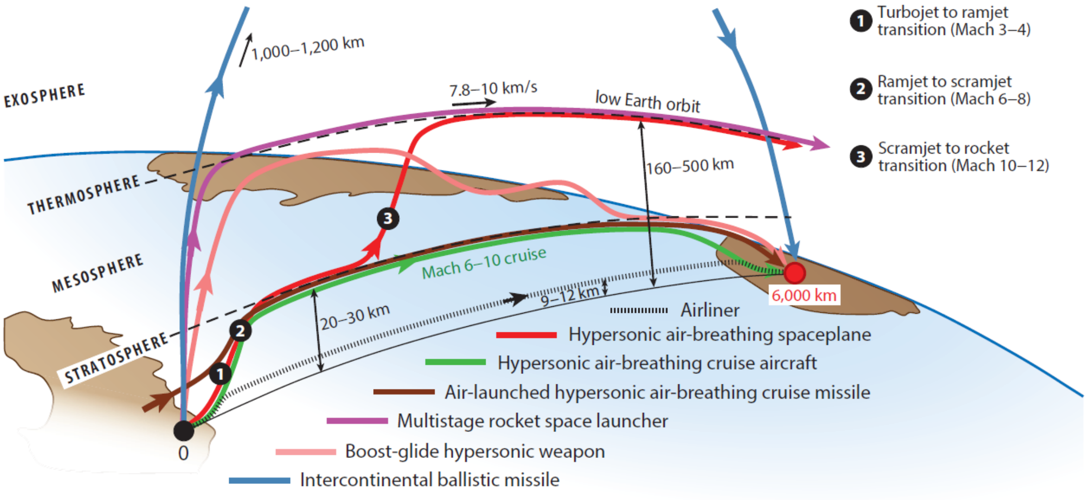

EXOSPHERE
THERMOSPHERE
MESOSPHERE
STRATOSPHERE
1,000–1,200 km
7.8–10 km/s
low Earth orbit
160–500 km
Mach 6–10 cruise
20–30 km
9–12 km
6,000 km
0
1
2
3
1 Turbojet to ramjet transition (Mach 3–4)
2 Ramjet to scramjet transition (Mach 6–8)
3 Scramjet to rocket transition (Mach 10–12)
Airliner
Hypersonic air-breathing spaceplane
Hypersonic air-breathing cruise aircraft
Air-launched hypersonic air-breathing cruise missile
Multistage rocket space launcher
Boost-glide hypersonic weapon
Intercontinental ballistic missile

Figure 2.1: Characteristic flight trajectories for different aerospace vehicles [13].

Consider the hypothetical flight mission which requires transition to low Earth-orbit, where oxygen is no longer available for supersonic-combustion, thus resulting in the need to use rocket-propulsion to accelerate the vehicle across the mesosphere. Figure 2.1 implies that the transition from scramjet to rocket should occur at Mach numbers of around 10 to 12. This once more suggests that the required threshold for scramjet operability should not be far beyond Mach 10.

2.1.1 Trajectory Point

The previous section presented the reasoning for not considering a vehicle designed to travel at speeds higher than Mach 10, whereas section 1.3.1 stated that while an hypersonic airbreathing vehicle cannot operate at freestream velocities that are higher than that for which it was designed for, it can, however, operate at freestream Mach numbers which are lower than its design Mach number, as long as spillage can occur. Therefore the vehicle should be designed for flight conditions correspondent to the maximum Mach number at which it is expected to operate - in this case, Mach 10. The present section serves to explicitly determine the trajectory point at which the freestream Mach number is 10.

The set of feasible trajectory points, or flight corridor, for airbreathing propulsion engines are limited by the severe flight conditions that arise due to high mechanical and thermal loads. One parameter that serves to assess whether a given trajectory point is within the flight corridor is the dynamic pressure q. On the one hand, if the dynamic pressure is too low, the wing area required for sustainable flight is unreasonably high; on the other hand, if q is too high, the aerodynamic and/or structural forces acting on the vehicle may lead to material failure. Figure 2.2 identifies the limits of the flight corridor for an hypersonic airbreathing engine, as function of the freestream Mach number, altitude and dynamic pressure.

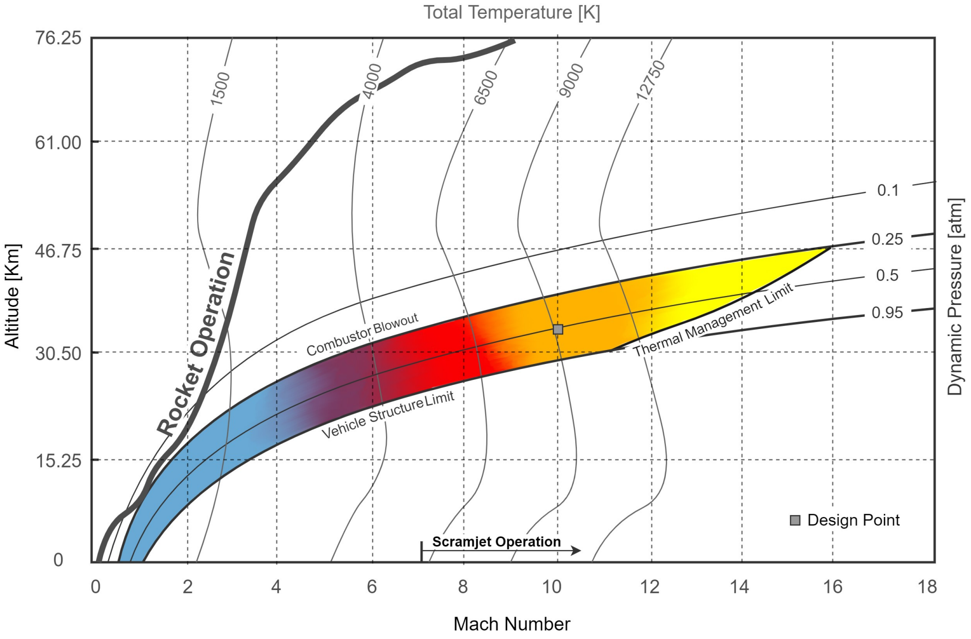

Figure 2.2: Flight corridor for an hypersonic airbreathing engine as function of Mach number, altitude and dynamic pressure. Identification of the trajectory point selected. Adapted from [14].

The figure above shows that the set of feasible trajectory points has an upper bound of low dynamic pressure, which is characterized by low combustion efficiency. On the other hand, the lower bound, characterized by high dynamic pressure, is limited by mechanical loads. Lastly, the flight corridor is cut off at high Mach numbers due to the presence of non-equilibrium effects and high thermal loads. This results in a very narrow set of feasible points, which respect all three restrictions. The trajectory point selected, for a freestream Mach number of 10, is within the feasible region, at a dynamic pressure of 50kPa, a compromise between the low and high dynamic pressures that bound the flight corridor, and an altitude of 33km.

Thermal management limit

In the present section a trajectory point characterized by a dynamic pressure which was a compromise between the lower and upper bounds was identified. This point was selected to assure sufficient combustor efficiency, while not falling into the risk of material failure. However, the thermal management limit, presented in figure 2.2 was not properly quantified. While Fry [7] describes this limit as a region of high dissociation levels, where chemical and thermal non-equilibrium ultimately affect the performance of the different components, the question remains of how high can the temperature inside an hypersonic airbreathing engine be. The answer to this question comes down to the material selected, and while it is beyond the scope of this work to study the properties of the different materials available, it is important to keep in mind a maximum value of wall temperature allowed in order to assess the feasibility of the different compression systems considered.

Gonçalves [15] also addresses this issue in his master thesis, and presents a series of possible materials for use in hypersonic airbreathing vehicles [16]. Among these materials, Gonçalves considers Polymer Matrix Composites (PMC), such as the carbon-carbon composites used by NASA in the Space Shuttle orbiter design; Metallic Matrix Composites (MMC), which provide increased toughness and strength; and Ceramic Matrix Composites (CMC), which are typically used in thermal protection systems. These are expected to withstand cyclic thermal loads of temperatures that can go up to 1500K, hence this was set as the maximum allowed value for wall temperature.

2.2 Case Study

Having established a key trajectory point at which an hypersonic airbreathing engine is expected to operate, the currently available literature was surveyed to find a case study that would provide a baseline geometry for the compression system. Reference [10] provides a methodology for a compression system design, based on oblique-shock theory, as well as its application to a compression system whose operating design point corresponds to Mach 10.

While the work developed on reference [10] focuses solely on the comparison between compression systems with different numbers of oblique shock waves, for the purpose of this work, other geometric changes will be considered. The geometry consists of a mixed compression inlet, of the form presented in figure 2.3, where θ_1 is the angle of the first ramp with respect to the freestream flow direction, θ_2 is the angle of the second ramp, with respect to the first ramp, H is the freestream capture height and h is the throat height.

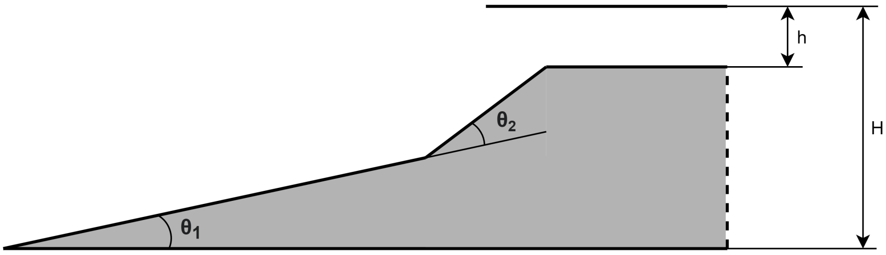

Figure 2.3: Schematics of a mixed compression system.

For the baseline design presented in reference [10], the values of θ_1, θ_2, H and H/h, are the ones given in table 2.1.

$\theta_1[^\circ]$	$\theta_2[^\circ]$	H [m]	H/h
6.5	8.4	0.250	10

Table 2.1: Baseline design for the two-dimensional compression system [10].

Additionally, reference [10] considers an isolator length, L, of 0.5m. As stated in section 1.3.2, this component allows the flow to adapt to the back pressure imposed by the downstream components, thus preventing inlet unstart. This back pressure is essentially determined by the necessary conditions at the combustor entry for ignition to occur, and, for a combustor entry velocity of 2400m/s, and temperatures above 1000K, reference [17] shows that a back pressure of 50kPa results in an acceptable combustor length required for the combustion reaction. On the other hand, reference [18] shows that supersonic combustion can occur for combustor entry pressures as low as 20kPa, while it considers that circa 50kPa is merely an ideal value for maximum combustion efficiency. For the purpose of this work, it was considered that the 50kPa should be a desired value at the isolator exit, however slightly lower pressures at this location will be assumed to not impede supersonic combustion, as proposed by reference [18].

2.2.1 Axisymmetric compression system

While the case study considered in the previous section is two-dimensional, several of the early experimental supersonic combustion ramjets were axisymmetric [19]. This geometry is typically shorter and lighter weight, when compared to the two-dimensional layout, however its integration in the vehicle is made through a pod-mounted engine, which results in a high drag configuration [7].

In this work, the integration of the engine in the vehicle and the resulting external forces are not being considered, and interest lies mainly on assessing the compression system's performance parameters and capability for providing the necessary conditions to the combustor entry. For this reason, a comparison between the two-dimensional and axisymmetric geometries, for the same operating point, was considered pertinent.

Chapter 3

Mathematical Formulation

This chapter presents the fundamental equations that establish a foundation for the numerical work developed. From Chapter 1, section 1.1, it became clear that, to account for all phenomena that characterize hypersonic flow, additional considerations needed to be made.

For starters, the presence of chemical dissociation requires that the gas be treated as a mixture of different chemical species, that may be in a state of chemical non-equilibrium. Additionally, high-temperature effects may result in the excitation of the different internal degrees of freedom of the gas, indicating that thermal non-equilibrium should also be accounted for. Lastly, the use of the Navier-Stokes equations is applied under the assumption of a continuum medium without any rarefaction effects. Section 3.1 addresses these issues, section 3.2 presents the equations of oblique shock theory, used in the design of the compression systems, and section 3.3 presents the available parameters to assess compression system performance.

3.1 Non-equilibrium Chemically Reacting Flow

3.1.1 Gas Mixture

In any hypersonic airbreathing engine, chemical reactions are expected to occur. These can be a result of the combustion process, but can also take place earlier in the engine, if the temperatures in the boundary layer of the compression system are sufficiently high for oxygen to dissociate. For this reason, it is important to consider the gas as a mixture of several chemical species, assumed to be mixed into a single phase, allowing for the treatment of its macroscopic properties to be a function of the local chemical composition. The detailed overview of the thermodynamic relations used to describe the properties of a gas mixture has been included in Appendix A.

In this work, the gas flowing inside any compression system was considered to be a mixture of N_2, O_2, N, O and NO. The temperatures inside an hypersonic airbreathing engine are not expected to be so high that ionization occurs, hence, to reduce computational costs, no ionized species were considered for the conducted simulations.

3.1.2 Chemical Non-equilibrium

A gas mixture is said to be in chemical equilibrium when its chemical composition is only subject to variations due to temperature gradients. However, as aforementioned, the more typical case inside an hypersonic airbreathing engine's combustion chamber, is that the characteristic times for the flow are of the order of magnitude of the characteristic times for combustion processes, resulting in chemical non-equilibrium. In this state, chemical composition is not only a function of the temperature gradients, but also of the finite rate at which chemical reactions try to achieve a new state of equilibrium.

Chemical non-equilibrium is accounted for by chemical-kinetic models, which determine the rate of formation for each of the chemical species of the gas mixture. Consider the generic chemical reaction given by equation 3.1,

$$\sum_i \nu_i' X_i' \underset{k_b}{\overset{k_f}{\rightleftharpoons}} \nu_i'' X_i'', \tag{3.1}$$

where ν_i' represents the stoichiometric coefficient of the reactants (X_i'); ν_i'' represents the stochiometric coefficients of the products (X_i''); and k_f and k_b are, respectively, the forward and backward reaction rate constants. The net rate of formation, of each of the species i, present in the chemical reaction of equation 3.1, is given by equation 3.2,

$$\frac{\mathrm{d}[X_i]}{\mathrm{d}t} = (\nu_i'' - \nu_i') \left\{ k_f \prod_i [X_i]^{\nu_i'} - k_b \prod_i [X_i]^{\nu_i''} \right\}, \tag{3.2}$$

where $[X_i]$ is the concentration, or number of moles per unit volume, of species i. Now considering every reaction r taking place within the gas mixture, the rate of formation or consumption, $\dot{\omega}_s$, of each species s of the mixture, is given by equation 3.3, where M_s is the molar mass of species s.

$$\dot{\omega}_s = M_s \frac{\mathrm{d}[X_s]}{\mathrm{d}t} = M_s \sum_r (\nu_{s,r}'' - \nu_{s,r}') \left\{ k_{f_r} \prod_s [X_s]^{\nu_{s,r}'} - k_{br} \prod_s [X_s]^{\nu_{s,r}''} \right\}. \tag{3.3}$$

3.1.3 Thermal Non-equilibrium

To properly understand the thermal behaviour of a chemically reacting flow, it becomes relevant to account for the microscopic particles that constitute the gas, that is, to consider that it is made up of atoms, molecules, electrons and ions. Inside an hypersonic airbreathing engine, these microscopic particles' coherent kinetic energy is converted into thermal energy through the excitation of their internal degrees of freedom, which, depending on the particle, can be stored into four different thermal energy modes: translational, rotational, vibrational and electronic. Figure 3.1 illustrates each of these modes.

Consider the molecule presented in figure 3.1, which can possess all types of energy modes. The translational energy mode corresponds to the kinetic energy associated with the molecule's centre of mass; the rotational energy mode portrays the molecule's rotation in space; the vibrational energy mode represents the movement of the atoms with respect to an equilibrium position within the molecule; and the electronic energy mode is given by the motion of electrons with respect to the nucleus of the molecule's atoms. The total energy of the molecule, ε, is then the sum of the energy stored in each mode with the zero-point energy of the species, ε_0, as given by equation 3.4a.

$$\varepsilon = \varepsilon_{\text{trans}} + \varepsilon_{\text{rot}} + \varepsilon_{\text{vib}} + \varepsilon_{\text{el}} + \varepsilon_0. \tag{3.4a}$$

For the case of atomic particles the rotational and vibrational modes are not present, and equation 3.4a is reduced to equation 3.4b,

$$\varepsilon = \varepsilon_{\text{trans}} + \varepsilon_{\text{el}} + \varepsilon_0. \tag{3.4b}$$

Considering a macroscopic point of view, it is also possible to define the total internal energy per unit mass, e, of a single-species s as the sum of the internal energy associated with each thermal energy mode with the effective zero-point energy of the species, $(\Delta \mathsf{h}_s)^\circ$, as given by equation 3.5.

$$e_s = e_{\text{trans},s} + e_{\text{rot},s} + e_{\text{vib},s} + e_{\text{el},s} + (\Delta \mathsf{h}_s)^\circ. \tag{3.5}$$

The expressions used to evaluate the specific internal energy of each mode, as well as other relevant thermodynamic properties, are discussed in more detail in Appendix A.

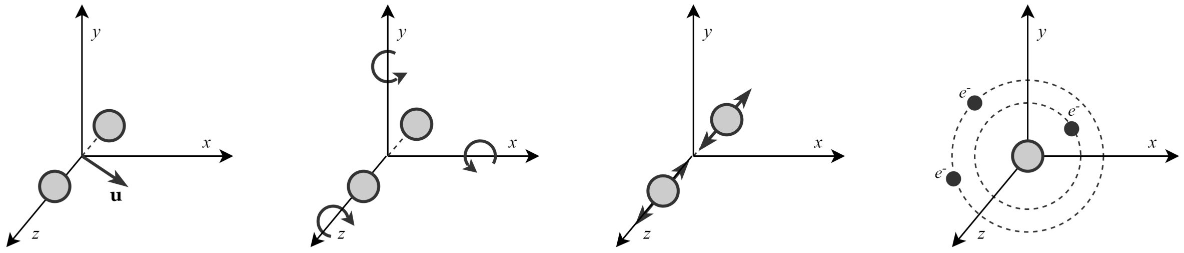

(a) Translational (b) Rotational (c) Vibrational (d) Electronic

Figure 3.1: Thermal energy modes. Adapted from [1].

Multi-Temperature Models

When all energy modes of a mixture are at the same characteristic temperature, T, the gas is said to be in thermal equilibrium. However, in the presence of high gradients, as the ones the flow is subject to inside an hypersonic airbreathing engine, it is more probable that each of the chemical species has their own energy modes excited differently in what is called thermal non-equilibrium. When this is the case, multiple temperatures must be used, each associated with the different species thermal energy modes, in a multi-temperature model approach.

One such model is the two-temperature model ($2T$), proposed by Park [20], which assumes that the temperature of the translational and rotational energy modes is the same, $T_{\text{trans-rot}}$, while the temperature of the vibrational energy mode, $T_{\text{vib-el}}$, is in equilibrium with the electronic energy mode. An extension to this model would be the three-temperature model ($3T$), which distinguishes between the temperatures of the vibrational energy mode, T_{vib}, and the electronic energy mode, T_{el}. Table 3.1 summarizes the differences between the different models, for different microscopic particles.

	Energy mode				
	Translational		Rotational	Vibrational	Electronic
	(Electrons)	(Heavy particles)	(Molecules)	(Molecules)	(Heavy)
Equilibrium	T	T	T	T	T
$2T$	$T_{\text{vib-el}}$	$T_{\text{trans-rot}}$	$T_{\text{trans-rot}}$	$T_{\text{vib-el}}$	$T_{\text{vib-el}}$
$3T$	T_{el}	$T_{\text{trans-rot}}$	$T_{\text{trans-rot}}$	T_{vib}	T_{el}

Table 3.1: Multi-temperature models.

For the purpose of this work, it was considered that the two-temperature model was sufficient to verify if thermal non-equilibrium is present within an hypersonic airbreathing engine, while the three-temperature model would result in an increased computational cost.

3.1.4 Governing Equations

Non-equilibrium chemically reacting flows are governed by a system of partial differential equations, corresponding to a description of Navier-Stokes conservation equations, applied to mass, momentum, total energy and thermal energy. As previously mentioned, the application of these equations is valid under the assumption of a continuum medium, which is true for freestream Knudsen numbers, Kn, that do not exceed 0.01. According to [2], the Knudsen number for the case of hypersonic airbreathing propulsion is always less than 10^{-5}, thus the assumption of a continuum medium and, therefore, Navier-Stokes conservation equations apply.

Mass conservation equation

For each of the chemical species s present in the mixture, a mass conservation equation, given by 3.6, is applied.

$$\frac{\partial(\rho c_s)}{\partial t} + \nabla \cdot (\rho c_s \mathbf{u}) = \nabla \cdot J_s + \dot{\omega}_s, \tag{3.6}$$

where ρ is the density, c_s is the mass fraction of species s, $\mathbf{u}$ is the flow velocity vector, J_s is the mass diffusion flux vector, given by Fick's law of diffusion (equation 3.7), and $\dot{\omega}_s$ is the rate of formation or consumption of species s, as defined in section 3.1.2.

$$J_s = \rho D_s \nabla c_s, \tag{3.7}$$

where D_s is the mass diffusion coefficient of species s.

Given that, for a given system, the total mass is conserved, the sum of all mass conservation equations yields the global continuity equation given by equation 3.8.

$$\frac{\partial \rho}{\partial t} + \nabla \cdot (\rho \mathbf{u}) = 0. \tag{3.8}$$

Momentum conservation equation

The momentum conservation equation is a result of the application of Newton's second law of motion to a fluid, and is given by equation 3.9, where $[\tau]$ is the viscous stress tensor and p is the pressure.

$$\frac{\partial(\rho\mathbf{u})}{\partial t} + \nabla\cdot(\rho\mathbf{u}\otimes\mathbf{u}) = \nabla\cdot[\tau] - \nabla p. \tag{3.9}$$

Total energy conservation equation

The total energy conservation equation (equation 3.11) takes into account the effects of diffusion through the heat-flux vector, $\mathbf{q}$, which is given by equation 3.10,

$$\mathbf{q} = -\sum_k k_k \nabla T_k + \sum_s J_s h_s + \mathbf{q}_R, \tag{3.10}$$

where k_k and T_k are, respectively, the thermal conductivity and temperature associated with the thermal energy mode k, h_s is the enthalpy of species s and $\mathbf{q}_R$ is the radiative heat flux vector, not considered in this work.

$$\frac{\partial(\rho e)}{\partial t} + \nabla\cdot(\rho\mathbf{u}e) = \nabla\cdot(\mathbf{u}\cdot[\tau]) - \nabla\cdot\mathbf{q} - \nabla\cdot(p\mathbf{u}), \tag{3.11}$$

where e is the total internal energy per unit mass, as defined in section 3.1.3.

Non-equilibrium thermal energy conservation equation

In addition to total energy conservation, thermal energy must also be conserved for all modes defined in section 3.1.3, according to equation 3.12,

$$\frac{\partial(\rho e_k)}{\partial t} + \nabla\cdot(\rho\mathbf{u}e_k) = \nabla\cdot\left(-k_k\nabla T_k + \sum_s J_s h_{s,k}\right) + \dot{\Omega}_k, \tag{3.12}$$

where $\dot{\Omega}_k$ is the energy-exchange source term associated with the thermal energy mode k.

3.1.5 Transport Coefficients

The dissipative fluxes present in the equations defined in section 3.1.4 model the transport of mass, momentum and energy, necessary to describe the behaviour of the flow with respect to concentration, velocity and temperature gradients, respectively. Table 3.2 provides a summary of the models used to define each of the dissipative fluxes, as well as the corresponding gradients and transport coefficients.

Of the table presented above, only the relationship between the viscous stress tensor, $[\tau]$ and its transport coefficient, μ, has not yet been defined. This is modelled assuming a Newtonian fluid, and is given by equation 3.13, where μ is the dynamic viscosity coefficient and $[\mathrm{I}]$ is the identity matrix.

$$[\tau] = \mu(\nabla\mathbf{u} + \left(\nabla\mathbf{u})^{\mathrm{T}}\right) - \frac{3}{2}\mu(\nabla\mathbf{u})[\mathrm{I}]. \tag{3.13}$$

Dissipative Flux	Equation	Model	Transport Coefficient	Gradient
J_s	Mass	Fick's Law	D_s	∇c_s
$[\tau]$	Momentum	Newtonian Fluid	μ	$\nabla \mathbf{u}$
$k_k \nabla T_k$	Energy	Fourier's Law	k_k	∇T_k

Table 3.2: Definition of the dissipative fluxes, corresponding gradients and transport coefficients.

Transport Models

While the transport coefficients, corresponding to each dissipative flux, have been identified, no equations have been established for the calculation of these terms. The classical solution which allows for the determination of the transport coefficients is the computationally expensive Chapman-Enskog solution of the Boltzman equation [21]. However, mixing rules which approximate the Chapman-Enskog solution, at a lower computational cost, are more often employed by computational fluid dynamics software.

In this work, the Wilke/Blottner/Eucken model, which is expected to yield reasonable results for low levels of ionization, and temperatures that do not exceed 10000K [22], has been used in all simulations. This model assumes that all binary interactions have the same, hard-sphere, cross-section, which results in the general expressions of equation 3.14 for the dynamic viscosity and thermal conductivity of a mixture, as a function of the species' mole fractions [22].

$$\mu = \sum_s \frac{x_s \mu_s}{\phi_s}, \tag{3.14a}$$

and,

$$k_k = \sum_s \frac{x_s k_{k,s}}{\phi_s}, \tag{3.14b}$$

where x_s is the mole fraction of species s and ϕ_s is a scale factor which depends on the dynamic viscosities and molar masses of the interacting species according to equation 3.15,

$$\phi_{s_i} = \sum_j x_{s_j} \left[1 + \left(\frac{\mu_{s_i}}{\mu_{s_j}} \right)^{\frac{1}{2}} \left(\frac{M_{s_j}}{M_{s_i}} \right)^{\frac{1}{4}} \right]^2 \left[8 \left(1 + \frac{M_{s_i}}{M_{s_j}} \right) \right]^{-\frac{1}{2}}, \tag{3.15}$$

where the viscosity of a given species is given by Blottner's curve fitting model [23], according to equation 3.16,

$$\mu_s(T_{\text{trans},s}) = 0.1 \exp(C_s) {T_{\text{trans},s}}^{(A_s \ln(T_{\text{trans},s}) + B_s)}, \tag{3.16}$$

where the curve-fitting coefficients A_s, B_s and C_s are given for each species s individually. The thermal conductivity is given by Eucken's relation [24], which accounts for each thermal mode according to the expressions of equation 3.17,

$$k_{k,s} = \frac{5}{2}\mu_s c_{v\,k,s}, \qquad \text{if } k = \text{trans} \tag{3.17a}$$

$$k_{k,s} = \mu_s c_{v\,k,s}, \qquad \text{if } k = \text{rot, vib, el.} \tag{3.17b}$$

where $c_{v\,k,s}$ is the specific heat at constant volume of the energy mode k of species s (Annex A.1.5).

Lastly, the mass diffusion coefficient is given by equation 3.18, and is assumed equal for all species.

$$D_s = D = \frac{\text{Le}\,k}{\rho c_p}, \tag{3.18}$$

where Le is the Lewis number, which measures the ratio of thermal diffusivity to mass diffusivity, and c_p is the gas mixture specific heat at constant pressure (Annex A.1.5).

3.2 Oblique Shock Wave Theory

Owing to its simplicity, oblique shock wave theory was used to dimension the different inlet compression systems. Nevertheless, it is important to keep in mind that this theory applies to the inviscid flow of a calorically perfect gas, while the flow within an hypersonic air breathing engine, is both viscous and subject to high temperature effects. The discrepancy between the predicted behaviour and the actual flowpath inside the diffuser will be further discussed in chapter 5.

Oblique shock waves, unlike normal shock waves, are two-dimensional. This results in the need to distinguish between the magnitude of the velocity component which is normal to the oblique shock wave, u_n, and the magnitude of the velocity component which is tangent to the oblique shock wave, u_t. Figure 3.2 presents a schematic of the change in the velocity components, when the flow crosses an arbitrary oblique shock wave. In the figure, θ and β are, respectively, the turn angle and the shock wave angle, measured with respect to the upstream flow velocity vector, and the indexes 1 and 2, stand, respectively, for conditions upstream and downstream the oblique shock wave.

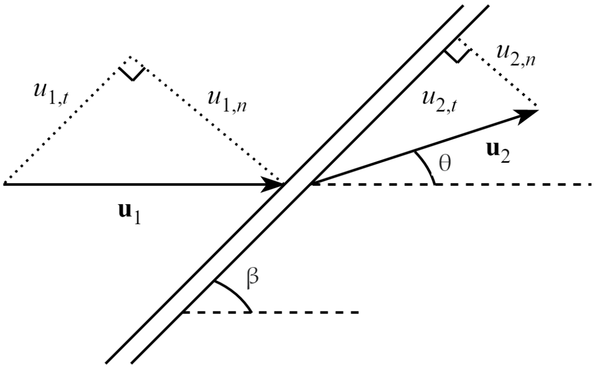

Figure 3.2: Schematic of the change in the velocity components, when the flow crosses an arbitrary oblique shock wave. Adapted from [25].

In compliance with the figure presented above, the magnitude of the upstream flow velocity which is normal to the oblique shock wave can be written as a function of the magnitude of the upstream flow velocity and the shock wave angle, according to equation 3.19a.

$$u_{1,n} = u_1 \sin\beta. \tag{3.19a}$$

Similarly, it is possible to write the component of the upstream flow Mach number which is normal to the oblique shock wave as a function of the upstream flow Mach number and the shock wave angle, as given by equation 3.19b.

$$\mathsf{Ma}_{1,n} = \mathsf{Ma}_1 \sin\beta. \tag{3.19b}$$

However, the shock wave angle β is not known *a priori* and must be first determined to find the conditions of the flow downstream the oblique shock wave. This angle can be iteratively calculated, as a function of the upstream flow Mach number and the turn angle, through what is known as the $\beta-\theta-$Ma relation, presented in equation 3.20,

$$\tan\theta = 2\cot\beta\left[\frac{\mathsf{Ma}_1^2\sin^2\beta - 1}{\mathsf{Ma}_1^2(\gamma+\cos 2\beta)+2}\right], \tag{3.20}$$

where γ is the ratio between the specific heat at constant pressure c_p and the specific heat at constant volume c_v, and is constant for a calorically perfect gas (Annex A.1.5).

Knowing β and provided that the conditions upstream the oblique shock wave are known, it is possible to obtain the conditions downstream the oblique shock wave as given by the relations presented in equation 3.21a through 3.21d.

$$\frac{p_2}{p_1} = 1 + \frac{2\gamma}{\gamma+1}(\mathsf{Ma}_{1,n}^2 - 1). \tag{3.21a}$$

$$\frac{\rho_2}{\rho_1} = \frac{(\gamma+1)\mathsf{Ma}_{1,n}^2}{(\gamma-1)\mathsf{Ma}_{1,n}^2 + 2} \tag{3.21b}$$

$$\frac{T_2}{T_1} = \frac{(p_2/p_1)}{(\rho_2/\rho_1)} \tag{3.21c}$$

$$\mathsf{Ma}_2 = \frac{1}{\sin(\beta-\theta)}\sqrt{\frac{1+\frac{\gamma-1}{2}\mathsf{Ma}_{1,n}^2}{\gamma\mathsf{Ma}_{1,n}^2 - \frac{\gamma-1}{2}}} \tag{3.21d}$$

3.2.1 Application to axisymmetric flow

In the case of a supersonic or hypersonic flow around a conical surface, the streamlines are not parallel due to the axysymmetric nature of the flow. This results in the variation of the properties with the distance to the cone surface, downstream an oblique shock wave, which can be solved using the Taylor-Maccoll analysis [26]. This section will present a brief description of this method.

Consider the coordinate system that passes through the vertex of the cone, and the coordinates r, ϑ and φ, corresponding, respectively, to the radial coordinate along a ray that passes through the vertex, the angle that the ray makes with the symmetry axis of the cone, and the angle measured around the axis. Because the flow is axisymmetric, the flow conditions do not vary with φ, and equation 3.22 is valid for all properties.

$$\frac{\partial}{\partial\varphi} = 0. \tag{3.22}$$

Furthermore, the Taylor-Maccoll analysis assumes that properties do not change along a ray, which yields,

$$\frac{\partial}{\partial \mathrm{r}} = 0. \tag{3.23}$$

Taking into account equations 3.22 and 3.23 into the equations of conservation of mass, momentum and energy, written in the polar coordinates defined above, Taylor and Maccoll derived the differential equations which describe the change in the flow velocity components behind an oblique shock wave originated at the vertex of a conical surface as set of equations 3.24,

$$\frac{\gamma-1}{2}\left[u_{max}^2 - u_\mathrm{r}^2 - \left(\frac{\mathrm{d}u_\mathrm{r}}{\mathrm{d}\vartheta}\right)^2\right]\left(2u_\mathrm{r} + \frac{\mathrm{d}u_\mathrm{r}}{\mathrm{d}\vartheta}\cot\vartheta + \frac{\mathrm{d}^2u_\mathrm{r}}{\mathrm{d}\vartheta^2}\right) - \frac{\mathrm{d}u_\mathrm{r}}{\mathrm{d}\vartheta}\left(u_\mathrm{r}\frac{\mathrm{d}u_\mathrm{r}}{\mathrm{d}\vartheta} + \frac{\mathrm{d}u_\mathrm{r}}{\mathrm{d}\vartheta}\frac{\mathrm{d}^2u_\mathrm{r}}{\mathrm{d}\vartheta^2}\right) = 0, \tag{3.24a}$$

$$u_\vartheta = \frac{\mathrm{d}u_\mathrm{r}}{\mathrm{d}\vartheta}. \tag{3.24b}$$

where u_{max}^2 is the velocity magnitude that the flow would attain if it were isentropically expanded to 0K, u_r is the magnitude of the radial component of the velocity and u_ϑ is the magnitude of the angular velocity component, perpendicular to the rays.

The equations presented above have no analytical solution, and must be solved iteratively to determine the oblique shock wave angle, after which the equations of oblique shock wave theory can be used to determine the flow turn angle as well as the flow conditions immediately after the oblique shock wave.

Because in reference [10] a ratio of specific heats of 1.4 was used to dimension the compression system, the same value was used, when dimensioning the axisymmetric compression system.

3.3 Compression System Performance

This section will present an overview of the available parameters to assess compression system performance, as they are presented in reference [2]. In this reference, the author simplifies the expressions by considering that it is reasonable to assume a mean, constant value for the specific heats ratio, and by considering that the flow does not interact with its surrounding, i.e., that there is no heat, work or mass exchange. Despite the fact that they are a simplification, these parameters will ultimately provide us with the means to compare the different geometries considered.

Furthermore, for the purpose of assessing performance, section averaged values of the different quantities were used, under the assumption that the flow is mixed to a uniform, one-dimensional state. According to [11], this assumption assumes a higher entropy than the actual entropy of the flow, and therefore, underestimates the true performance of a given compression system.

Total Pressure Ratio

A simple measure of inlet performance is the total pressure ratio between the conditions at the isolator exit and the freestream conditions, π_c, as given by equation 3.25.

$$\pi_c = \frac{p_{tc}}{p_{t\infty}} = \frac{p_c}{p_\infty}\left\{\frac{1+\frac{\gamma-1}{2}\mathsf{Ma}_c^2}{1+\frac{\gamma-1}{2}\mathsf{Ma}_\infty^2}\right\}^{\frac{\gamma}{\gamma-1}}. \tag{3.25}$$

In the equation above, p_{tc}, p_c and Ma_c are the total pressure, the static pressure and the Mach number at the combustor entry (or isolator exit), respectively; and $p_{t\infty}$, p_∞ and Ma_∞ are the total pressure, the static pressure and the Mach number, at freestream conditions, respectively.

Kinetic Energy Efficiency

Heiser [2] defines the kinetic energy efficiency as the ratio between the square of the velocity that the flow at the compression system exit would achieve if it were isentropically expanded to the freestream static pressure, V_X^2, and the square of the freestream velocity, V_∞^2, as given by equation 3.26a.

$$\eta_{\mathsf{KE}} = \frac{V_X^2}{V_\infty^2}. \tag{3.26a}$$

Recalling that, for the purpose of this analysis, the specific heats are assumed to be constant, and assuming that the flow does not interact with its surroundings, energy conservation allows rearranging the above equation as a function of the temperature that the flow would achieve if were isentropically expanded to the freestream static pressure, T_X, as given by equation 3.26b.

$$\eta_{\mathsf{KE}} = \frac{V_\infty^2 - 2c_p(T_X - T_\infty)}{V_\infty^2}. \tag{3.26b}$$

Furthermore, remembering that the velocity at any point of the flow may be written as a function of the local Mach number, as well as the ratio of specific heats and the universal gas constant, and that the specific heat at constant pressure is also a function of these variables, the expression above can be mathematically manipulated to be of the form of equation 3.26c.

$$\eta_{\mathsf{KE}} = 1 - \frac{2}{(\gamma-1)\mathsf{Ma}_\infty^2}\left\{\frac{T_X}{T_\infty} - 1\right\}. \tag{3.26c}$$

Lastly, taking into consideration that the ratio (T_X/T_c) is a result of the isentropic deceleration of the flow between the pressure at the combustor entry and the freestream pressure, equation 3.26d, of which all parameters are known, is also valid.

$$\eta_{\mathrm{KE}} = 1 - \frac{2}{(\gamma-1)\mathrm{Ma}_\infty^2}\left\{\frac{T_c}{T_\infty}\left(\frac{p_c}{p_\infty}\right)^{-\frac{\gamma-1}{\gamma}} - 1\right\}. \tag{3.26d}$$

The kinetic energy efficiency is considered to be a particularly useful parameter due to the fact that is referenced to the freestream conditions [2]. Furthermore, kinetic energy efficiency is directly related to engine specific impulse [11] and therefore constitutes a relevant performance parameter.

Compression Efficiency

The compression efficiency is the ratio of change in enthalpy that the flow at the combustor entry (or isolator exit) would incur if it were isentropically expanded to freestream static pressure, divided by the change in enthalpy that the flow is effectively put through, as given by equation 3.27a.

$$\eta_c = \frac{h_c - h_X}{h_c - h_\infty} = \frac{c_p(T_c - T_X)}{c_p(T_c - T_\infty)}. \tag{3.27a}$$

Recalling that, for the purpose of this analysis the specific heats are assumed to be constant, equation 3.27a can be rewritten as equation 3.27b.

$$\eta_c = \frac{(T_c/T_\infty) - (T_X/T_\infty)}{(T_c/T_\infty) - 1} \tag{3.27b}$$

Lastly, remembering that the ratio (T_X/T_c) is a result of the isentropic deceleration of the flow between the pressure at the combustor entry and the freestream pressure, equation 3.27c, of which all parameters are known, is also valid.

$$\eta_c = \frac{(T_c/T_\infty) - (T_c/T_\infty)(p_c/p_\infty)^{-\frac{\gamma-1}{\gamma}}}{(T_c/T_\infty) - 1}. \tag{3.27c}$$

Reference [11] indicates that the usage of a single performance parameter is insufficient, further claiming that the total pressure ratio and the kinetic energy efficiency are often used together for ideal gas problems. In this work it was chosen to also include the compression efficiency, as it represents the familiar formula used in the typical thermodynamic cycle analysis of a turbine engine.

In the calculation of all presented performance parameters, the average value of 1.36 for the ratio of specific heats will be used, as suggested in [2].

Mass Flow Rate Ratio

To quantitatively account for flow spillage, and for the amount of oxygen effectively available for the combustion process, it was deemed worthy to access the ratio of mass flow rate between the freestream capture area and the isolator exit. The mass flow rate, assuming section averaged quantities, is given by equation 3.28, where $\dot{m}$ is the mass flow rate and A is the cross-sectional area.

$$\dot{m} = \rho u A \tag{3.28}$$

For the two-dimensional geometry, A is simply equal to the height of each section (H for the freestream capture mass flow rate, and h for the mass flow rate at the isolator exit).

For the axisymmetric geometry, the freestream capture area is given by equation 3.29a while the area at the isolator exit is given by equation 3.29b.

$$A = \pi \mathsf{H}^2, \tag{3.29a}$$

$$A = \pi(\mathsf{H}^2 - (\mathsf{H} - \mathsf{h})^2). \tag{3.29b}$$

Chapter 4

Numerical Implementation

This chapter will begin by describing the main characteristics of the Computational Fluid Dynamics solver used, as well as the input file necessary to conduct a simulation within the solver environment. Similarly, it will briefly address the different boundary conditions chosen to solve the flow within the compression system and isolator components of an hypersonic airbreathing engine. Next, the grid convergence studies conducted for both the two-dimensional and axisymmetric geometries will be presented, and a proper grid configuration will be established for each case. Lastly, the simulation strategy used to reduce computational times will be presented.

4.1 Computational Fluid Dynamics Solver

The *Software Package for Aerothermodynamics, Radiation and Kinetics* (SPARK) is a Computational Fluid Dynamics code for hypersonic flows, maintained by the University of Illinois and by the Institute of Plasmas and Nuclear Fusion (IPFN), a research unit of Instituto Superior Técnico. Developed by Lopez *et al.*, SPARK uses object-oriented programming to implement different physical models and numerical methods in a unified framework, which allows for greater flexibility and maintainability than other available numerical tools [27]. The code itself is capable of performing 0D (temporal relaxation), 1D (post-shock relaxation) or 2D (planar or axisymmetric) simulations using Euler or Navier-Stokes compressible flow-formulations.

In terms of gas modelling, SPARK allows for the choice of perfect gas, frozen gas, or a chemically reacting gas mixture, which requires a chemical kinetic model. Different multi-temperature as well as state-to-state models may also be selected to address non-equilibrium effects. SPARK does not include, however, a turbulence model, hence the flow is assumed laminar throughout the entire fluid domain.

In terms of numerical solver, the code employs a cell-centered finite volume formulation, whereas, for the temporal discretization, both implicit and explicit second order schemes are available.

4.1.1 SPARK Input File

To launch a simulation in SPARK, an input file with the initialization parameters must be provided. It is mandatory that this file contains information about the gas model (perfect, frozen, or chemically reacting), the flow type (Euler or Navier-Stokes), the simulation type (0D, 1D, 2D-Planar, or 2D-Axisymetric), and, for the case of a chemically reacting flow, an adequate kinetic model. Additionally, the file must state what are the chemical species to be considered, as well as the initial or upstream conditions of the flow. A mesh file must also accompany the input file, which defines the physical domain, whereas the boundary conditions are defined in the input file itself. Lastly, information regarding the solver may be included, namely temporal discretization, the Courant-Friedrichs-Lewy (CFL) condition, and criteria for convergence.

For all simulations conducted the mesh file that accompanies the input file was created using the open-source Gmsh software, which allowed for the creation of the structured meshes supported by SPARK.

4.2 Boundary Conditions

4.2.1 Upstream Conditions

In chapter 2, a key-trajectory point was identified, corresponding to an altitude of 33km and a dynamic pressure of 50kPa. Table 4.1 presents the atmospheric conditions for this trajectory point, considered as the upstream conditions in SPARK.

Ma	u[km/s]	p[Pa]	T[K]	$x_{\mathrm{N_2}}$	$x_{\mathrm{O_2}}$	Species Involved
10	3.11	714	240	0.79	0.21	N_2, O_2, N, O, NO

Table 4.1: Upstream conditions at an altitude of 33km and a dynamic pressure of 50kPa.

The values of table 4.1 are the ones presented in reference [10], allowing for a comparison of results, however a verification was also made to ensure that these values correspond to the defined trajectory point [28].

4.2.2 Wall Boundary Condition

In the case of a non-equilibrium chemically reacting flow, chemical interactions between the wall and the flow may occur, that is, when the particles of the flow collide with the wall, they might recombine to form new particles [29]. Because recombination results in heat release, this is a relevant issue in hypersonic flow, and is directly related to the thermal management limit described in chapter 2.

A material or wall which enhances recombination of reactive species, or else changes the chemical equilibrium, is termed a catalytic wall, whereas a surface which inhibits recombination is called a non-catalytic wall. Anything in between would be termed a partially catalytic wall. Figure 4.1 summarizes the possible particle recombinations according to wall catalycity.

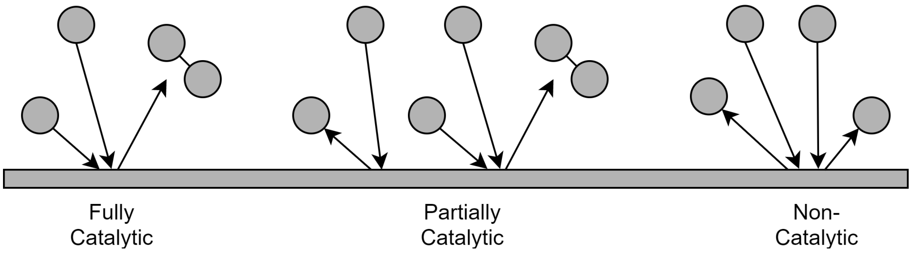

Figure 4.1: Particle recombination according to wall catalycity. Adapted from [29].

Because the fully catalytic case results in the greatest thermal loading, and therefore represents the worst-case scenario, all walls were set to fully catalytic, in a conservative approach, ensuring that we are below the thermal management limit.

In addition to defining wall catalicity, SPARK also allows defining a given wall as adiabatic or isothermal. Reference [10], from which the baseline geometry was selected, does not explicitly state which case was considered for the wall boundary condition, however Heiser [2] places the adiabatic wall temperatures between 3000K and 8000K, which is far above the maximum allowed temperature of 1500K, defined in chapter 2. Furthermore, both [2] and [10] place the maximum allowed temperature at the isolator exit (or combustor entrance) between 1440 and 1670K, to avoid high levels of dissociation. Finally, an analytical and experimental investigation of the internal flowfield characteristics of a two-dimensional scramjet inlet at Mach 10 is conducted in [30], where the subject of wall cooling is addressed. Here, a maximum wall temperature of six times the freestream temperature is considered, resulting in a wall temperature of approximately 1465K, which is below the working temperature allowed by the materials and within the range of maximum temperatures allowed at the combustor entry.

An isothermal, no-slip wall with its temperature set to $T_w = 1465$ was therefore applied to all wall boundaries.

4.2.3 Outlet Boundary Condition

Because the flow is supersonic at the isolator exit, a supersonic outlet boundary condition was set at this plane, where the properties at the boundary are extrapolated from the interior domain. Additionally, to account for flow spillage, the supersonic outlet boundary condition was favoured over the upstream boundary condition, for the northernmost boundaries, upstream of the cowl.

In the next section, a schematics of the grid configuration with the applied boundary conditions (figure 4.2) is provided to allow for a better visualisation of the contents described in the present section.

4.3 Mesh and Convergence Study

SPARK supports only structured meshes, which can be composed of several blocks. For the particular case of the two-dimensional compression system, a multiblock mesh, with a total of 14 blocks, was used. This configuration allowed for a better alignment between the cell faces and the flow preferential direction, at different regions of the flow. Additionally a near wall refinement was applied to capture boundary layer behaviour. Figure 4.2 presents the mesh configuration for the two-dimensional compression system, corresponding to the geometry presented in section 2.2, and a cowl length of 0.5m, as well as the applied boundary conditions.

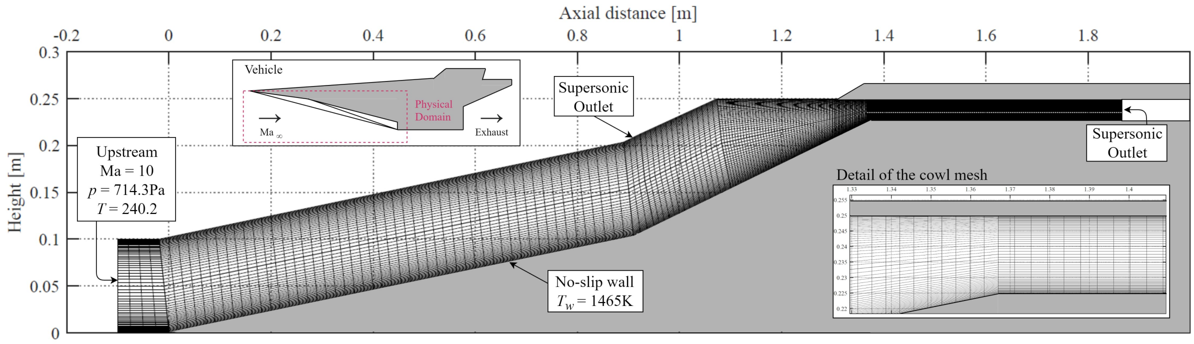
Axial distance [m]
-0.2
0
0.2
0.4
0.6
0.8
1
1.2
1.4
1.6
1.8
Height [m]
0.3
0.25
0.2
0.15
0.1
0.05
0
Vehicle
Physical Domain
Ma ∞
Exhaust
Supersonic Outlet
Upstream
Ma = 10
p = 714.3Pa
T = 240.2
No-slip wall
T_w = 1465K
Supersonic Outlet
Detail of the cowl mesh

Figure 4.2: Two-dimensional compression system mesh and boundary conditions (not to scale).

To reduce computational costs the normal distance between the inlet ramp wall and the farthermost cell, was tailored to the strict minimum necessary to fully capture the first oblique shock.

4.3.1 Grid Convergence Study

To settle on a grid configuration that appropriately captured all phenomena present in the compression system and isolator components, four different grid resolutions (115x28, 175x40, 175x60 and 250x60) were considered to solve the viscous (Navier-Stokes) frozen flow. Figure 4.3 presents the velocity and temperature profiles at the isolator exit, as a function of the normal distance from the lower wall, whereas figure 4.4 presents the pressure and temperature profiles as a function of the vertical distance from the second ramp wall, at 1.1m.

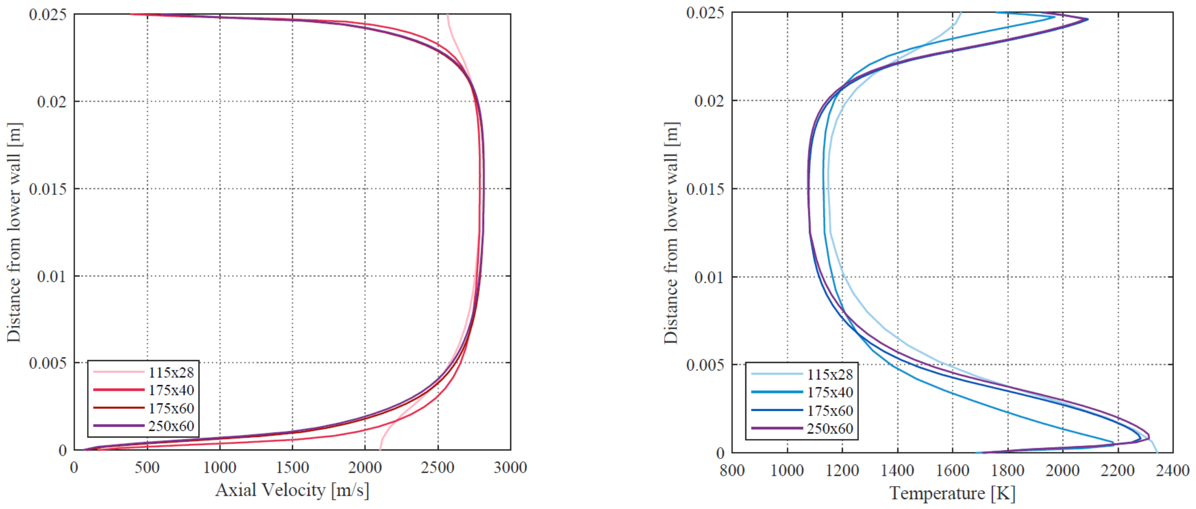

(a) Velocity profile at x=1.867m

(b) Temperature profile at x=1.867m

Figure 4.3: Velocity and temperature profiles as a function of the normal distance from the lower wall, at the isolator exit, for the different two-dimensional grid resolutions considered.

From the figures presented above, it becomes clear that the coarser mesh does not properly reproduce boundary layer behaviour, hence it was discarded. Nevertheless, the obtained results from this grid were considered in the dimensioning of the near wall refinement in order to attain a maximum Reynolds number of 20 at the wall surface, which is expected to be sufficient to properly capture wall heat transfer [31]. With that in mind, while the 175x40 configuration displays the expected boundary layer behaviour, when compared with the finer meshes, it does not fully capture the shock region (figure 4.4). Furthermore, regarding the temperature profiles at the isolator exit, this configuration over predicts the temperature at the flow core by 5.12%, and under predicts the temperature near the wall with a maximum relative error of 5.66% (figure 4.3).

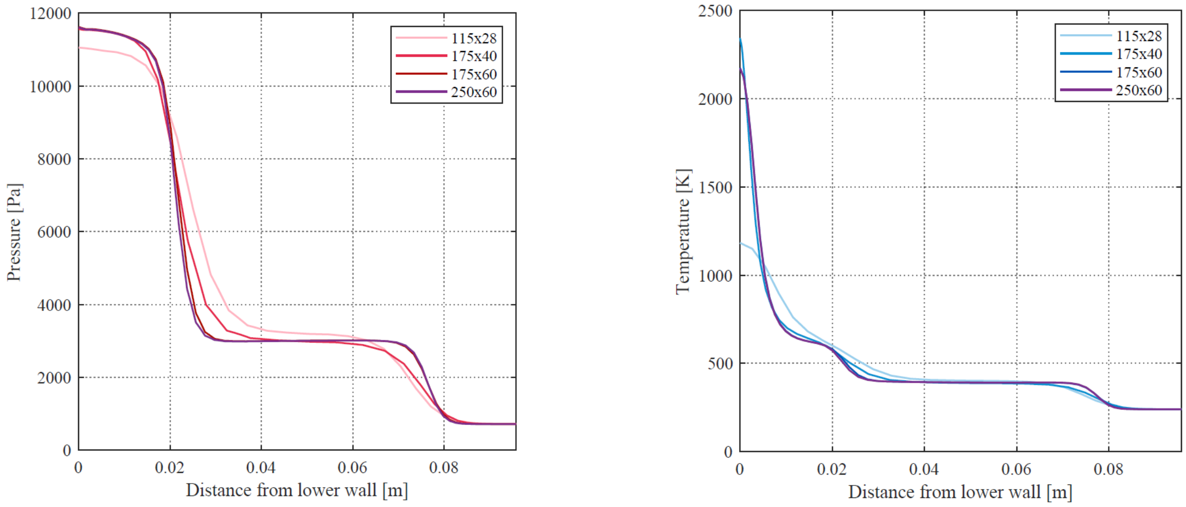

(a) Pressure profile at x=1.1m

(b) Temperature profile at x=1.1m

Figure 4.4: Pressure and temperature profiles as a function of the vertical distance from the second ramp wall, at x=1.1m, for the different two-dimensional grid resolutions considered.

The 175x60 grid configuration, when compared to the finest grid, reduces the maximum relative error, in terms of temperature profile, to 1.38% (figure 4.3b), while the maximum relative error of the remaining property profiles presented is below 1%. Since 250x60 grid configuration resulted in a much greater computational cost, which would prove impractical for the geometry parametric study, the 175x60 grid was deemed sufficiently accurate for further simulations. In terms of cell distribution in the axial direction, this configuration consists of 90 equally spaced cells along the isolator, where the gradients are higher, while the remaining 85 cells are distributed along the remaining physical domain.

4.3.2 Axisymmetric geometry

In light of the equations presented in 3.2.1, an axisymmetric geometry was dimensioned with the goal of comparing the originated flowfield within the two configurations considered. For that purpose, the axisymmetric layout presents the same compression ratio, i.e. the same ratio of pressure between the compression system inlet and outlet, and, as a first approach, the same contraction ratio, i.e. the same H/h, as the two-dimensional inlet. This resulted in the values for ϑ_1, ϑ_2, H and H/h presented in table 4.2, The cowl length was maintained at L=0.5m.

$\vartheta_1[^\circ]$	$\vartheta_2[^\circ]$	H [m]	H/h
8.6	11.3	0.250	10

Table 4.2: Design parameters for the baseline axisymmetric compression system.

A grid convergence study, similar to the one conducted in 4.3.1, was then applied to the geometry described in table 4.2 to four different grid configurations (160x28, 230x40, 230x60 and 350x60). The choice of a greater number of cells in the axial direction, when compared with the grids used in the two-dimensional geometry, was not arbitrary. Because the angle of an oblique shock wave over a conical surface is smaller than that obtained for a two-dimensional wedge, the required height to fully capture the first oblique shock was smaller, resulting in a reduction of the necessary height for the physical domain, and, consequently, in cells with a higher aspect ratio. The high aspect ratio made convergence difficult, hence, to counter this effect, a higher number of cells in the axial direction was applied.

Figure 4.5 presents the velocity and temperature profiles at the isolator exit, as a function of the normal distance from the lower wall, whereas figure 4.6 presents the pressure and temperature profiles as a function of the vertical distance from the second ramp wall, at 1.2m. In terms of mesh convergence study, the behaviour of the different grids considered was very similar to the one obtained for the two-dimensional meshes, hence, for the same reasons presented before, it was found that the appropriate grid configuration was the one with 230x60 cells. In terms of cell distribution in the axial direction, this configuration has 110 equally spaced cells within the isolator while the remaining 120 cells are distributed along the rest of the physical domain.

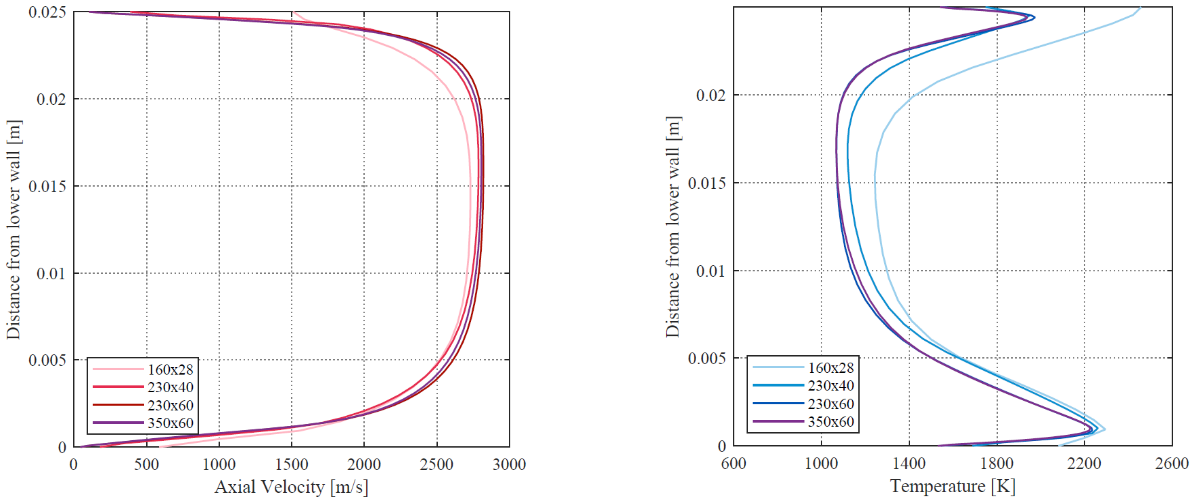

(a) Velocity profile at x=1.792m

(b) Temperature profile at x=1.792m

Figure 4.5: Velocity and temperature profiles as a function of the normal distance from the lower wall, at the isolator exit, for the different axisymmetric grid resolutions considered.

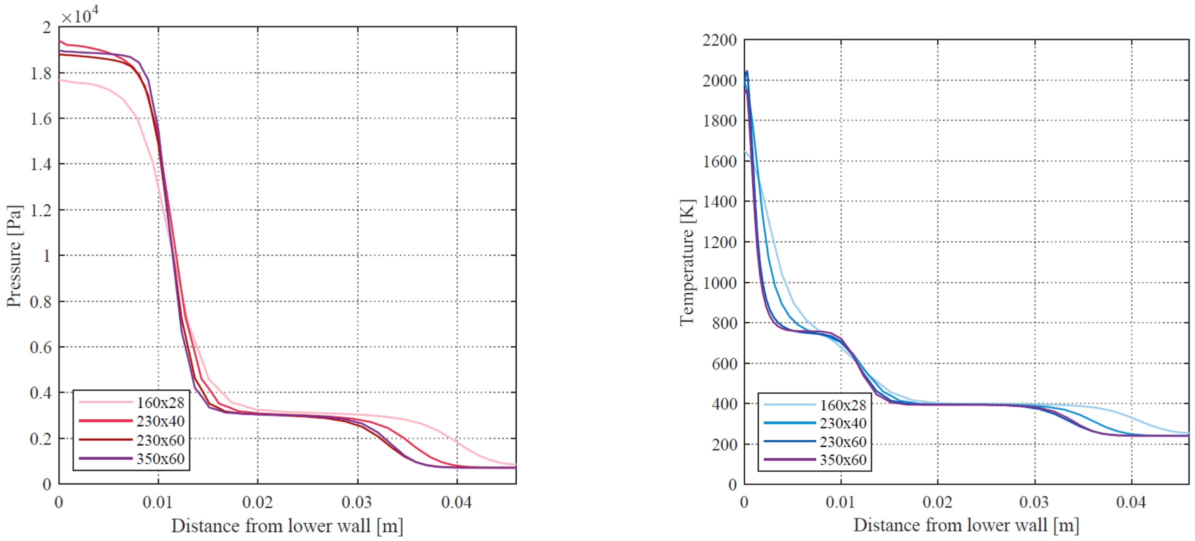

(a) Pressure profile at x=1.2m

(b) Temperature profile at x=1.2m

Figure 4.6: Pressure and temperature profiles as a function of the vertical distance from the second ramp wall, at x=1.2m, for the different axisymmetric grid resolutions considered.

4.4 Simulation Strategy

The simulation strategy employed had the main goal of reducing computational costs. This strategy consisted on an implicit time discretization, which, when compared to the explicit time discretization, resulted in a longer period of time to solve each iteration, but less necessary iterations overall. Additionally, before any chemical reactions or non-equilibrium effects were taken into consideration, the viscous (Navier-Stokes) frozen flow was first solved. Lastly, the CFL condition was gradually increased, accelerating convergence. The converged solution was considered as the point when the root-mean-square of the residuals of the system of equations dropped below 10^{-4}. Whenever possible, and particularly for frozen flow solutions, the simulation was kept running for a few more iterations, after it crossed the 10^{-4} threshold to ensure that the residual did not rise again.

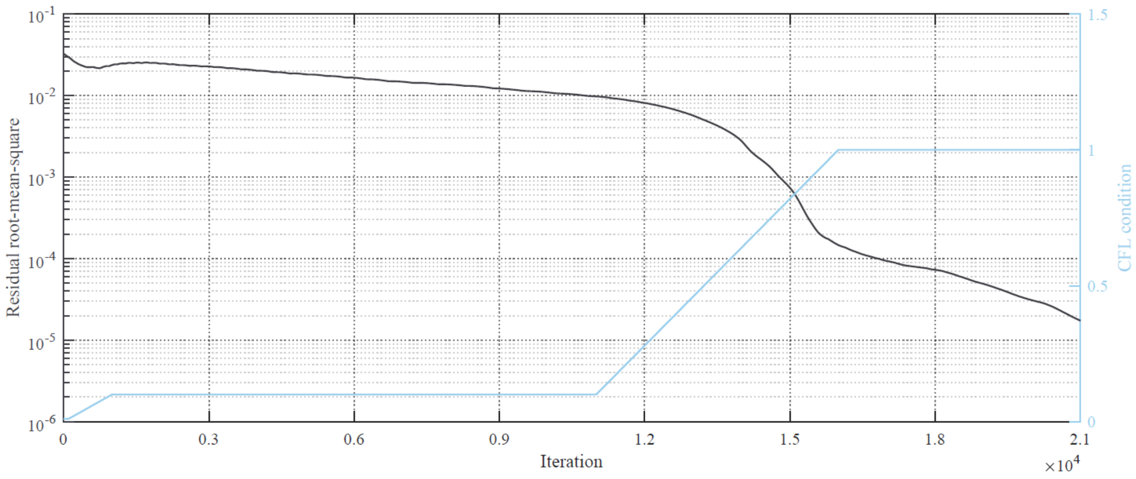

Figure 4.7: Residual root-mean-square and CFL condition as a function of the iteration number.

Figure 4.7, presents the residual history, as function of the iteration number, for the viscous (Navier-Stokes) frozen flow used in the mesh convergence study of the two-dimensional compression system. Additionally, the CFL condition at each iteration is displayed. During the simulation, the CFL condition was kept at no more than 0.1, until the shock train inside the isolator began to take shape, at around 10000 iterations. After this, the CFL was increased from 0.1 to 1 in the span of 5000 iterations, after which it was kept constant until the simulation was terminated. This strategy allowed for a significant reduction of the required total computational time from several weeks to only a few days. Furthermore, because reactive or multi-temperature simulations require even more computational power, they were usually initialized as a restart from a converged frozen flow solution, with CFL numbers that typically ranged from 0.5 to 1.

4.5 Flow Visualization and Data Treatment

Because SPARK was developed for atmospheric re-entry problems, whose phenomena are mostly one-dimensional, where typically monoblock grids are used, the plotting capabilities of SPARK do not properly allow for the visualization of the obtained flowfield. For this reason, the open-source *Paraview* software was favoured over the in-code plotter, while the *Matlab 2018a* software was used for data treatment. So as not to have excessively large files, the solution was typically only saved every one thousand iterations.

4.6 Model Shortfalls

One last comment that must be made before proceeding to the obtained results, is the identification of the shortfalls associated with the numerical implementation.

The first identified shortfall concerns the number of cells used in the discretization of the domain. At the time that the presented simulations were conducted, SPARK did not possess parallel computing capabilities, which greatly increased the computational times, when compared to most commercial codes. This effect was amplified when considering a chemically reacting gas and thermal non-equilibrium. That being said, to have feasible computational times, the considered grids possess a number of cells that is at least one order of magnitude lower than the ones found across the literature. Moreover, because only structured meshes were allowed, the non-disturbed flow upstream of the isolator presents an unnecessary refinement, which further contributed to increase computational costs.

Secondly, and as already stated, SPARK does not incorporate turbulence models, however Heiser [2] states that turbulent flow is expected to dominate lower freestream Mach numbers (of up to 10). Furthermore, turbulence is modelled in the case study chosen from the literature and against which the obtained results will be compared to. It is therefore important to keep in mind that this will constitute a discrepancy between the simulated parameters of reference [10] and the simulations conducted in this work. It is also worth noting that turbulence plays an important role in delaying boundary layer separation, which, as will be shown in the next chapter, can have a serious impact on the performance of an hypersonic airbreathing engine compression system.

Lastly, SPARK does not allow for the simulation of a three-dimensional geometry. While this does not constitute a discrepancy between the selected case study and the simulations conducted in this work, it does present a shortfall towards reality. The three-dimensional sidewall is expected to allow for higher compression in the axial direction and therefore aid in inlet start [32].

Chapter 5

Results

This chapter is divided into four main sections. The first section will begin by comparing the results obtained for the two-dimensional compression system and isolator against those presented in the selected case study. Next, and in light of some discrepancies found, the effect of wall temperature on the obtained flow field will be addressed, followed by the investigation of non-equilibrium effects, with special attention to conditions at the isolator exit, since they correspond to the conditions that will be present at the entrance to the combustor. A second section will present the obtained results for the axisymmetric geometry and highlight the differences in the flow behaviour between axisymmetric and two-dimensional configurations. A third section will vary some aspects of both geometries to clearly establish their influence on the behaviour of the flow within the compression system. The considered parameters include the number of ramps, the ramp angles, the isolator length and the isolator height, and, finally, the shape of the expansion corner. Furthermore, for the different considered geometries, the performance parameters of section 3.3 will be determined. Lastly, the results of the simulations conducted for the selected off-design Mach number will be presented.

5.1 Two-dimensional Configuration

5.1.1 Frozen Flow solution

The solution of the viscous (Navier-Stokes) frozen flow served multiple purposes. For starters, it allowed for the choice of an appropriate grid configuration, established in the previous chapter. Secondly, this solution corresponded to the results presented in the case study of reference [10], thus allowing for a verification and validation of the SPARK code's capability to solve the flow within an hypersonic airbreathing engine's compression system and isolator components. Lastly, it served as a baseline solution, against which the next simulations will be compared to. Figure 5.1 presents the pressure, density and temperature fields obtained for the viscous frozen-flow simulation; figure 5.2a compares the pressure variations across the first two oblique shock waves and at the cowl tip against the theoretical values; and figure 5.2b plots the pressure profile at the isolator exit.

A first observation that can be made, regarding the results presented below, is that, instead of con-

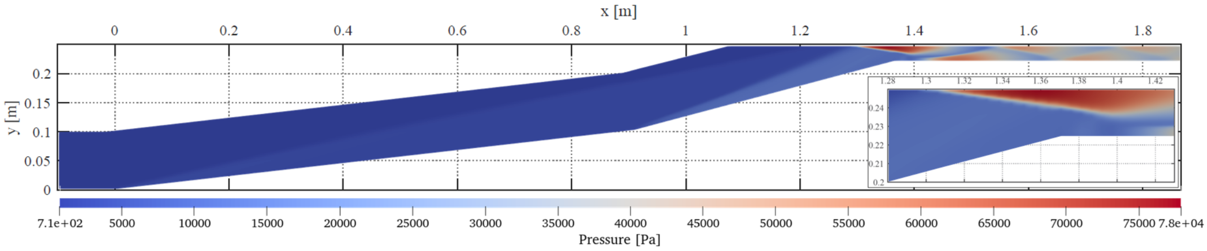

(a) Pressure field

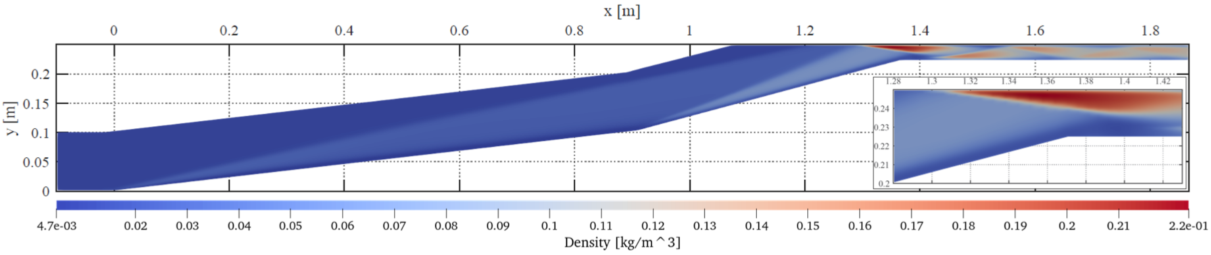

(b) Density field

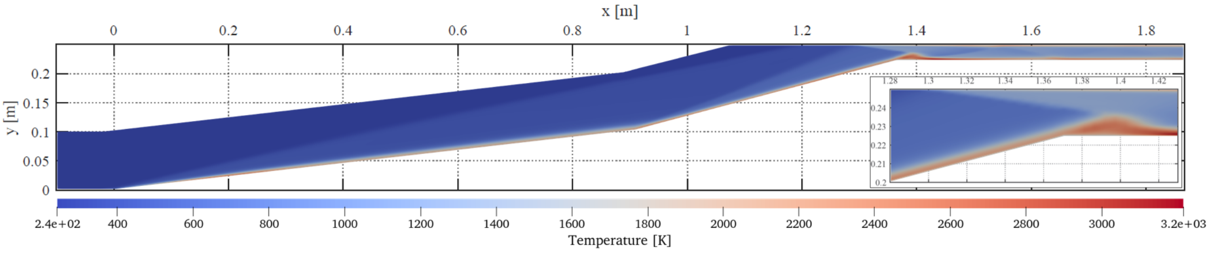

(c) Temperature field

Figure 5.1: Pressure, density and temperature fields obtained for the viscous (Navier-Stokes) frozen-flow simulation of the two-dimensional compression system.

verging to the cowl tip, the oblique shock waves generated by each of the compression system ramps present a wave angle that is higher than that predicted by oblique shock wave theory, resulting in flow spillage and in the absence of the shock-on-lip condition. This divergence from oblique shock-wave theory also transpires in the results of reference [10] and is analysed in detail in reference [25]. Both authors attribute it to the thickness of the viscous boundary layer, and in [10] it is further claimed that it is a desirable effect since it avoids a hot spot on the cowl tip. Another postulated advantage of this result is that, should the vehicle be required to accelerate, at the present atmospheric conditions, it will simply meet the shock-on-lip condition, instead of incurring in the unnecessarily high heat loads and flow instabilities associated with flight above the design Mach number (refer to section 1.3.1). Nonetheless, for the purpose of verification and validation of the SPARK code, it was deemed fit for this work to assess if, in the absence of viscous forces, the shock-on-lip condition would be met. To that end, an inviscid (Euler) frozen flow solution was obtained and will be discussed further ahead in this section.

The behaviour of the flow within the isolator, on the other hand, is in accordance with what is described across the literature and in 1.3.2. At the entry, the flow expands, resulting in flow separation and in the formation of a small recirculation zone. Within the isolator itself, a shock train forms, across which pressure is increased in a controlled manner.

Regarding the pressure variations across the first two oblique shocks (figure 5.2a), the results ob-

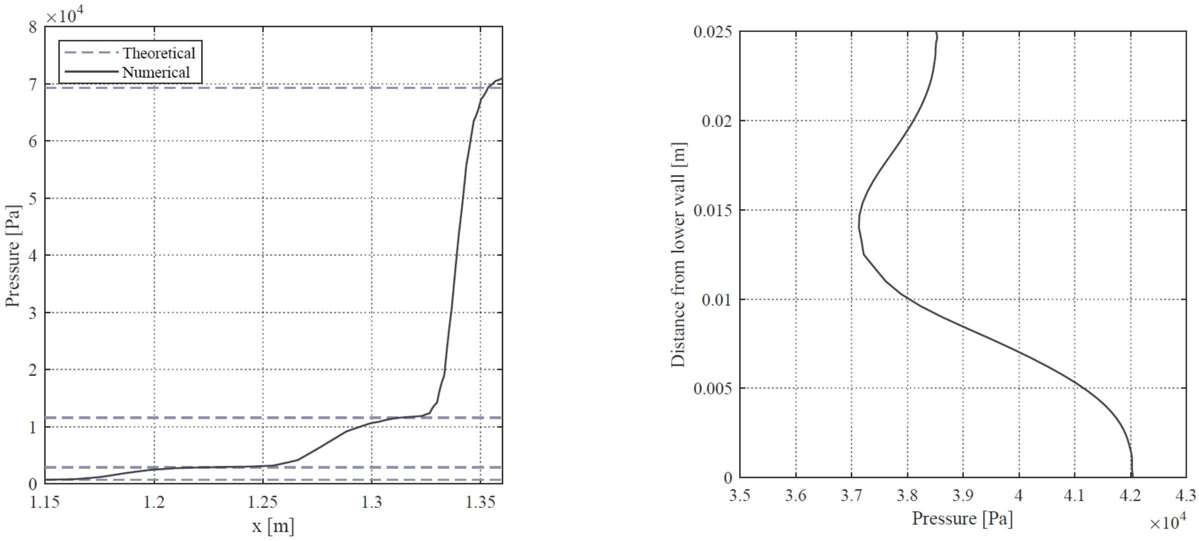

(a) Pressure variations at y=0.245m.

(b) Pressure profile at x=1.867m

Figure 5.2: Pressure variations across the first two oblique shock waves and at the cowl tip (a) and pressure profile at the isolator exit (b), for the frozen flow solution, for the two-dimensional configuration.

tained using SPARK were very similar to those presented in the case study from the literature, in the sense that, for both cases, the pressure after each of the first two oblique shocks nearly coincides with what is predicted by oblique shock wave theory. At the cowl tip, however, the pressure obtained using SPARK was 78006Pa, circa 4000Pa lower than that presented in [10], which corresponds to a local relative error of around 4.87%. Additionally, in the same reference, it is stated that the compression system provides the necessary conditions at the combustor entry, i.e. a temperature of at least 1000K, and a pressure of no less that 50kPa. Contrarily, and as is presented in figure 5.2b, the obtained values for pressure at the isolator exit fall just below that threshold, with a maximum exit pressure of 42039Pa at the lower wall and an average exit pressure of 38960Pa. As previously discussed (section 2.2), it was considered that a lower pressure did not impede supersonic combustion, but merely reduced its efficiency.

Besides turbulence not being considered, the only other discrepancy between the input parameters described in reference [10] and the ones used to obtain the presented results was in terms of the temperature selected for the wall boundary condition. This led us to conduct further simulations to assess if this parameter could significantly alter the obtained flowfield. This will be addressed in the following section.

Performance

For the frozen flow solution, the performance parameters of section 3.3 were obtained and are presented in table 5.1. Compared to the examples presented in reference [2], the obtained values fall within the expected range. As for the mass flow rate ratio, table 5.1 shows that nearly 30% of the mass flow is lost due to flow spillage and the blockage induced by the recirculation zone.

Case	π_c	η_{KE}	η_c	$\dot{m}_c/\dot{m}_\infty$
Baseline	0.0793	0.9442	0.7898	0.7921

Table 5.1: Performance parameters obtained for the frozen flow solution for the two-dimensional configuration.

Euler frozen flow solution

As aforementioned, the inviscid (Euler) frozen flow solution was obtained to assess if, in the absence of viscous effects, the shock-on-lip condition would be met. Figure 5.3 presents the density field of the inviscid frozen flow solution obtained.

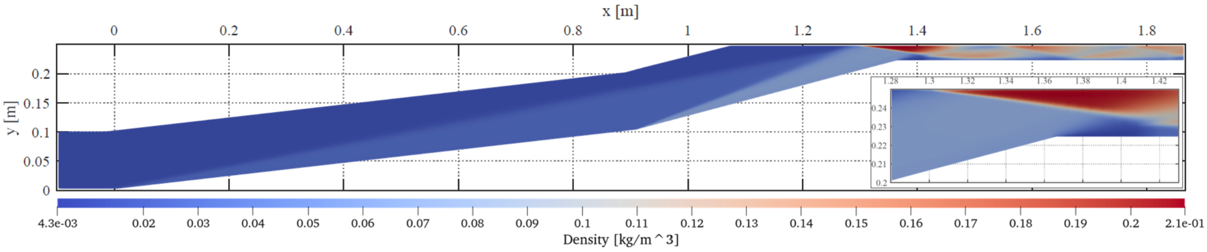

Figure 5.3: Density field obtained for the inviscid frozen flow simulation, for the two-dimensional configuration.

As evidenced in the figure, the absence of the thick, viscous boundary layer yields angles for each of the oblique shock waves which match those predicted by oblique shock theory. As such, the shock-on-lip condition is met.

5.1.2 Impact of Wall Temperature

In the previous section a discrepancy between the results presented in the case study from the literature and those obtained by SPARK was found. A possible cause for this discrepancy was identified as the chosen temperature for the wall boundary condition. This hypothesis was based on the fact that this parameter was not clearly defined in reference [10], and instead, as described in 4.2.2, a value from [30] was used. In the latter, two distinct wall temperatures are considered: around six times the freestream temperature, which gives the previously considered 1465K, and around three times the freestream temperature, which results in a wall temperature of 745K. Figure 5.4 presents the temperature and pressure profiles for each of the wall temperatures of reference [30] and also for the case of an adiabatic wall, while figure 5.5 presents the obtained temperature field for the case of an adiabatic wall boundary condition.

The results presented in figure 5.4a show that lowering the temperature of the wall boundary condition from $T_w = 1465$K to $T_w = 745$K, shifts the pressure at the entry to the combustor further away from the ideal value of 50kPa for supersonic combustion. Contrarily, setting the wall to be adiabatic, results on an isolator exit pressure that approximates the desired criteria. As is evidenced in 5.4b, this is attained at the cost of impossibly high wall temperatures, that none of the materials considered in 2.1.1 could withstand, therefore violating the thermal management limit.

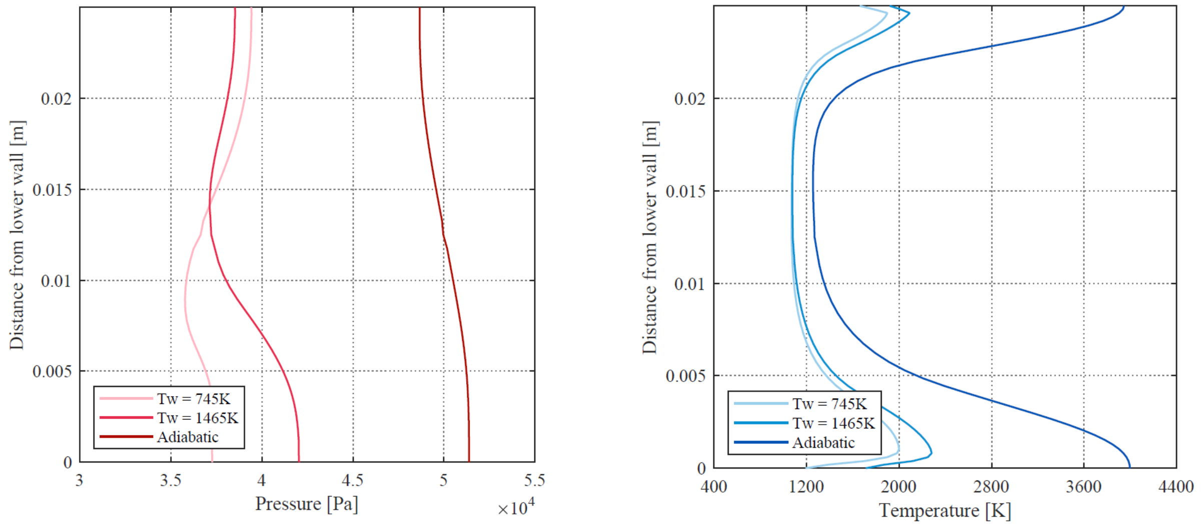

(a) Pressure profile at x=1.867m

(b) Temperature profile at x=1.867m

Figure 5.4: Pressure and temperature profiles at the isolator exit for different wall boundary conditions, for the two-dimensional configuration.

Figure 5.5 further emphasizes the repercussions of considering an adiabatic wall in terms of thermal loading, which becomes excessive not only in the isolator component, but along the entire compression system. Comparing this temperature field with the one presented in figure 5.1, another consequence of choosing an adiabatic wall boundary condition is the increase of the thickness of the boundary layer and separation region, which contributes to total pressure loss and reduces the available mass flow at the combustor entrance.

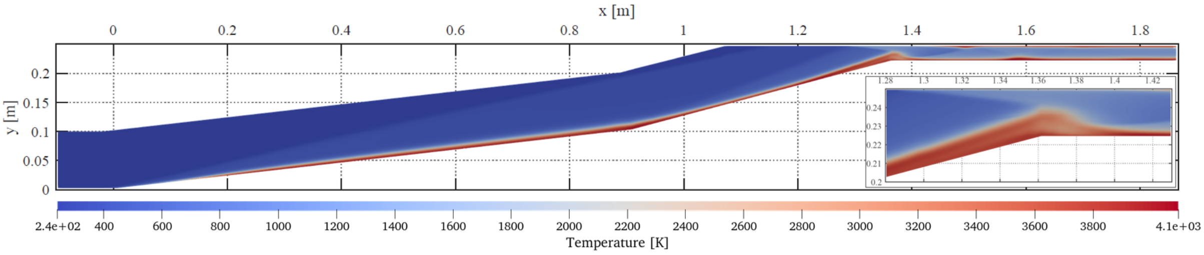

Figure 5.5: Temperature field obtained for the adiabatic wall boundary condition, for the two-dimensional configuration.

Lastly, table 5.2 shows how the performance parameters are affected by wall temperature, where the obtained values for the baseline solution ($T_w = 1465$K) are repeated here for convenience.

Case	π_c	η_{KE}	η_c	$\dot{m}_c/\dot{m}_\infty$
$T_w = 1465$K	0.0793	0.9442	0.7898	0.7921
$T_w = 745$K	0.0908	0.9495	0.7956	0.8127
Adiabatic	0.0332	0.9035	0.7661	0.6925

Table 5.2: Performance parameters obtained for the considered wall temperatures for the two-dimensional configuration.

Table 5.2 shows that performance increases for a lower wall temperature, and decreases when considering an adiabatic wall. The reader's attention should be drawn to the mass flow rate ratio which is reduced significantly for the case of an adiabatic wall. This is in excellent agreement with figure 5.5, which showed the bigger separation region at the isolator entry, for the adiabatic wall case, and which is expected to contribute to flow blockage.

5.1.3 Non-Equilibrium Chemically Reacting Flow Solution

This section will step outside what is covered in the case study of reference [10] by considering a non-equilibrium chemically reacting flow. As was discussed in previous chapters, high temperature effects can result in chemical dissociation, which can be accompanied by thermal non-equilibrium. To address chemical dissociation Park's kinetic model [33] was used to determine the forward reaction rate constants of equation 3.3, and to address thermal non-equilibrium Park's two-temperature model [20] was considered. Figure 5.6, plots the O and NO mass fraction distribution at the isolator exit for the case where only chemical dissociation was considered, while figure 5.7 compares the temperature and pressure profiles at the isolator exit for the reactive and frozen flow solutions.

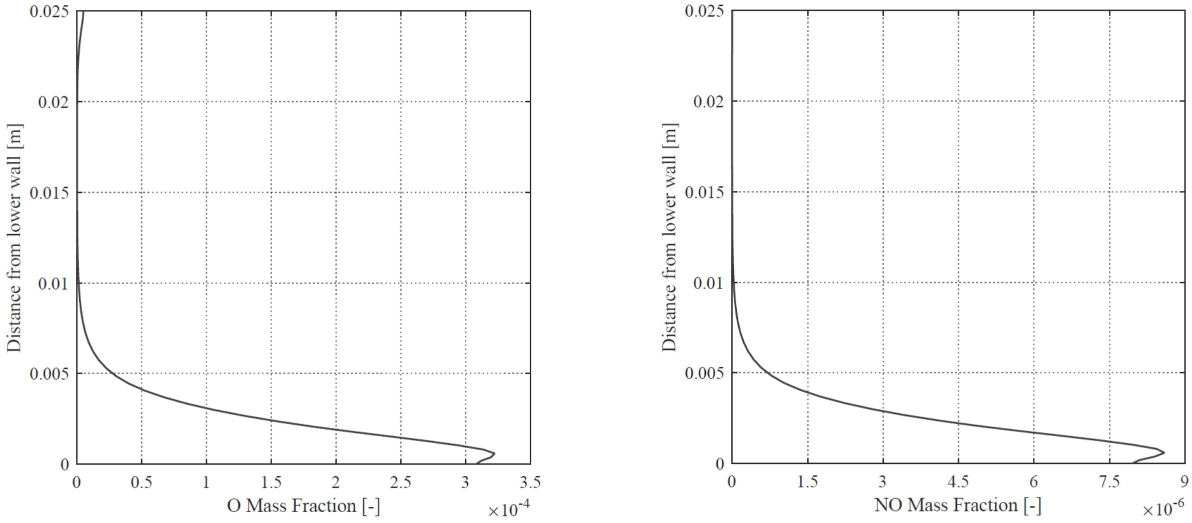

(a) O mass fraction profile at x=1.867m

(b) NO mass fraction profile at x=1.867m

Figure 5.6: O and NO mass fraction distribution at the isolator exit, for the two-dimensional configuration.

Figure 5.6 shows that the temperatures found within the isolator boundary layer are sufficient to cause dissociation of molecular oxygen, O_2. This is an expected result, given that oxygen dissociation is expected to start at 2000K, and figure 4.3b showed that the temperatures within the boundary layer, at the isolator exit, peak at around 2300K. Additionally traces of nitric oxide, NO, were also found at the isolator exit. This result is also predicted by Heiser, who further claims that the formation of NO is an undesirable consequence of high-temperature effects, since NO contributes to the formation of smog and to the destruction of the ozone layer [2].

Figure 5.7a shows that dissociation slightly shifts the pressure at the isolator exit, whereas figure 5.7b shows that the amount of energy consumed in the dissociation process was not sufficient to significantly alter the temperature profile in the same location.

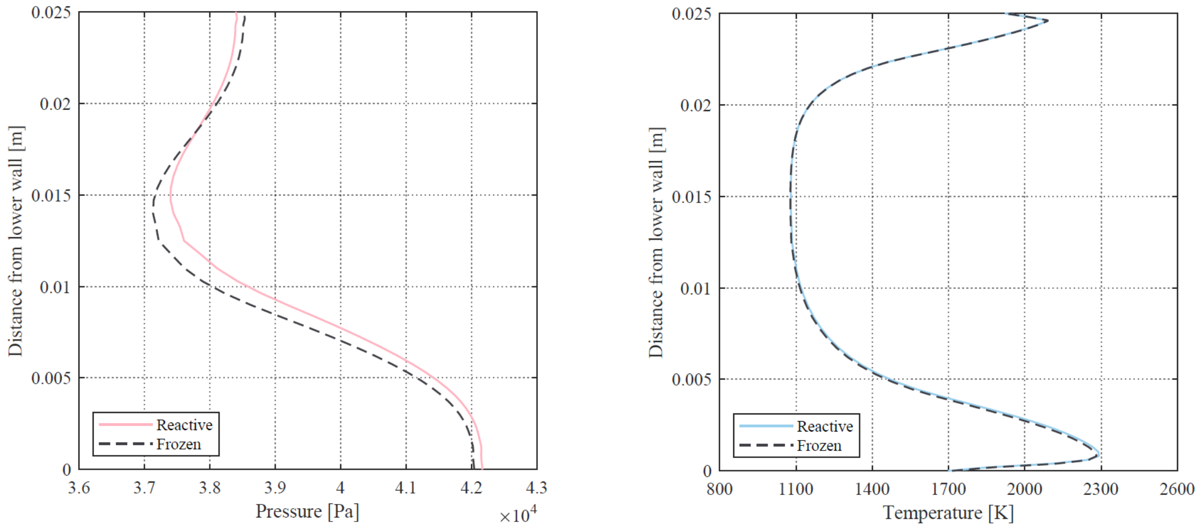

(a) Pressure profile x=1.867m

(b) Temperature profile x=1.867m

Figure 5.7: Pressure and temperature profiles of the reactive flow solution compared against the frozen flow solution, for the two-dimensional configuration.

The performance parameters for the reactive case are presented in table 5.3, where the obtained values for the baseline case (Frozen) are repeated here for convenience.

Case	π_c	η_{KE}	η_c	$\dot{m}_c/\dot{m}_\infty$
Frozen	0.0793	0.9442	0.7898	0.7921
Reactive	0.0781	0.9440	0.7897	0.7916

Table 5.3: Performance parameters obtained for the reactive flow solution for the two-dimensional configuration.

Expectedly, because the amount of dissociation observed was very small, the performance parameters obtained for the frozen and reactive cases are very similar.

Thermal Non-Equilibrium: Two-Temperature Model

As previously stated, thermal non-equilibrium is a typical outcome of a low-pressure, high-temperature chemically reacting viscous flow. Figure 5.8 compares the pressure and temperature distribution obtained at the isolator exit for the case of a chemically reacting flow with and without thermal equilibrium.

Figure 5.8a shows that the pressure profile at the isolator exit is significantly affected by thermal non-equilibrium, presenting a different shape altogether. It is thought that this is a result of the change in specific heats, which, in a multi-temperature model, are given as a sum of the specific heats for each of the thermal modes. Figure 5.8b further confirms that thermal non-equilibrium is present at the isolator exit, with translational-rotational and vibrational-electronic temperatures that differ by a maximum of 309.4K at the core of the flow. The vibrational-electronic temperatures lag behind the translational-rotational temperatures, because these are excited through exchanges with the translational-rotational

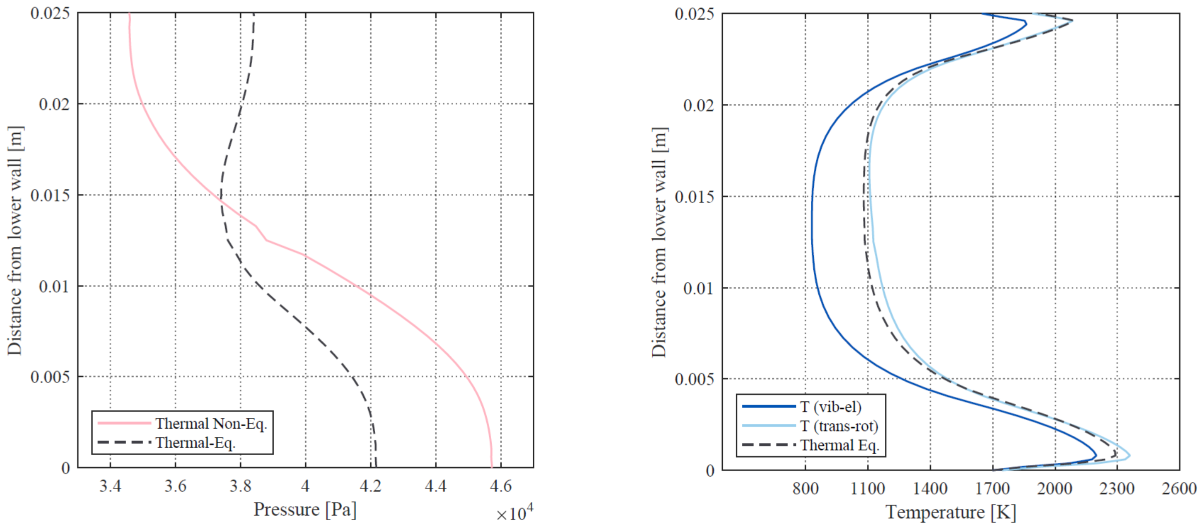

(a) Pressure profile x=1.867m

(b) Temperature profile x=1.867m

Figure 5.8: Pressure and temperature profiles of the reactive flow solution, at the isolator exit, compared against the case where thermal non-equilibrium was considered, for the two-dimensional configuration.

mode. These energy exchanges are slower than the excitation of the translational-rotational temperatures through the different oblique shock waves, which explains their lower temperatures at the isolator exit. Lastly, in the same location, the peak translational-rotational temperature in thermal non-equilibrium at the lower wall boundary layer is higher than the equilibrium peak-temperature by 2.88%.

Table 5.4 presents the performance parameters obtained for thermal equilibrium (frozen and reactive) and thermal non-equilibrium. For the case of thermal non-equilibrium the translational-rotational temperature was used to calculate the performance parameters.

Case		π_c	η_{KE}	η_c	$\dot{m}_c/\dot{m}_\infty$
Thermal Equilibrium	Frozen	0.0793	0.9442	0.7898	0.7921
	Reactive	0.0781	0.9440	0.7897	0.7916
Thermal Non-equilibrium		0.0652	0.9596	0.8183	0.7858

Table 5.4: Performance parameters obtained for the thermal equilibrium and non-equilibrium solutions for the two-dimensional configuration.

The results of table 5.4 show that the total pressure ratio decreases for the thermal non-equilibrium case, however, the kinetic energy efficiency as well as the the compression efficiency increase when thermal non-equilibrium is considered. Lastly, when thermal non-equilibrium was taken into account, the mass flow rate ratio was observed to be slightly lower (circa 0.5%).

Overall, one may conclude that thermal and chemical non-equilibrium effects have a limited impact over the global flow parameters and performance for the inlet.

5.2 Axisymmetric Configuration

5.2.1 Frozen Flow solution

As was the case for the two-dimensional geometry, the frozen flow solution for the axisymmetric configuration was obtained. This solution, too, will serve as the baseline solution against which any proceeding simulations will be compared to. Figure 5.9 presents the pressure, density and temperature fields obtained for the viscous frozen-flow solution; while figure 5.10 compares the pressure and temperature distributions at the isolator exit, for the two-dimensional and axisymmetric configurations.

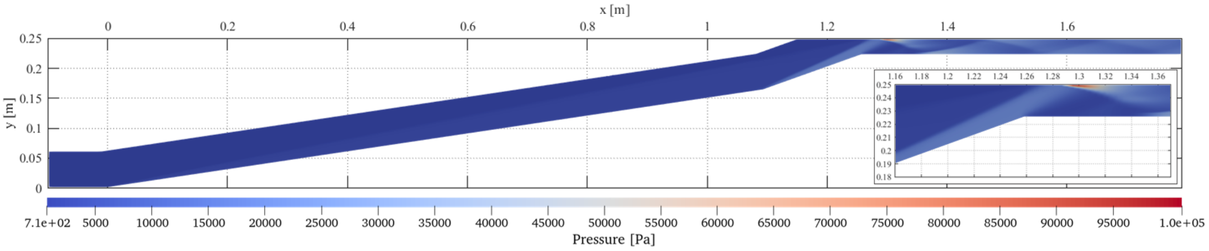

(a) Pressure field

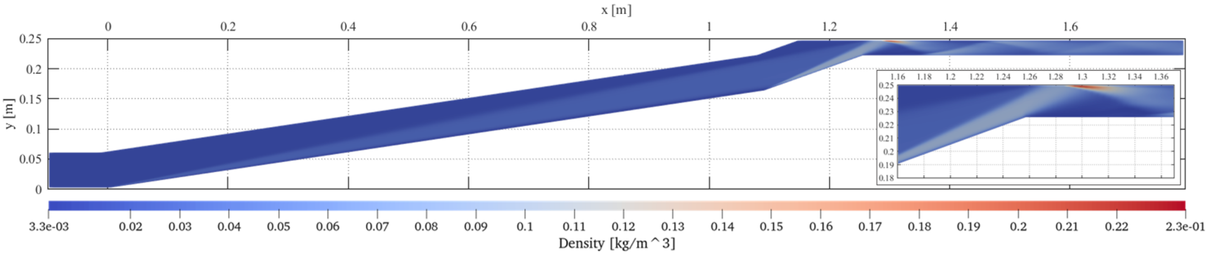

(b) Density field

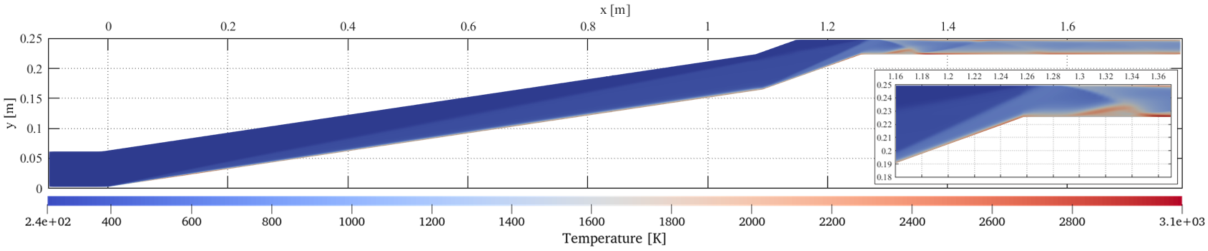

(c) Temperature field

Figure 5.9: Pressure, density and temperature fields obtained for the viscous (Navier-Stokes) frozen-flow simulation of the axisymmetric compression system.

Figure 5.9 shows that, while spillage occurs for the case of an axisymmetric geometry, it is not as significant as it was for the two-dimensional case. This validates the usage of the Taylor-Maccoll analysis to properly dimension the compression system geometry. On the other hand, as will be recalled from section 3.2.1, for the case of hypersonic flow around a conical surface, properties vary with distance to the cone surface. As a result, to ensure that the imposed compression ratio occurred for all rays, the obtained pressures after the second oblique shock were higher than those obtained for the two-dimensional flow. This is particularly distinguishable at the cowl tip, where the pressure peaks at 105282.16Pa, 34.97% more than the value obtained for the two-dimensional geometry in the same location.

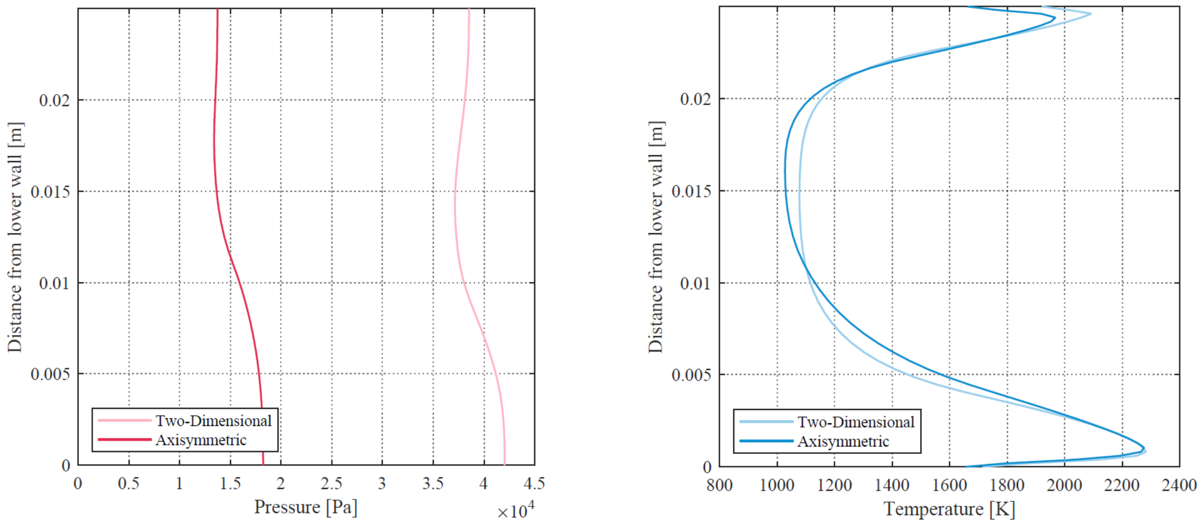

(a) Pressure profile

(b) Temperature profile

Figure 5.10: Comparison of the pressure and temperature profiles at the isolator exit for the two-dimensional and axisymmetric configurations.

Another remark that can be made regarding the behaviour of the flow obtained for axisymmetric geometry, when compared to the two-dimensional one, concerns the chosen contraction ratio. Figure 5.10a shows that, while a contraction ratio, H/h, of 10 assures, for the two-dimensional geometry, an average isolator exit pressure that falls just short to the ideal pressure for supersonic combustion, the average pressure at the same location, for the axisymmetric geometry, is of only 15359.61Pa, which is less than the 20kPa that reference [18] found necessary for ignition to occur. This means that this configuration might require a higher contraction ratio than the one used for the two-dimensional geometry. In contrast, figure 5.10b shows that the obtained temperature distributions fall within the same range for both the two-dimensional and axisymmetric configurations.

Performance

As for the two-dimensional geometry, the performance parameters defined in section 3.3 were obtained for the frozen flow solution of the baseline axisymmetric geometry and are presented in table 5.5. Moreover, they are also compared against the ones obtained for the two-dimensional baseline solution, repeated here for convenience.

Case	π_c	η_{KE}	η_c	$\dot{m}_c/\dot{m}_\infty$
Two-Dimensional	0.0793	0.9442	0.7898	0.7921
Axisymmetric	0.0327	0.9181	0.6833	0.6276

Table 5.5: Performance parameters obtained for the two-dimensional and axisymmetric frozen flow solutions.

Table 5.5 shows that all performance parameters present a lower value for the axisymmetric geometry than they did for the two-dimensional geometry. This is not an unexpected result, given that the obtained compression was much lower for this geometry. Furthermore, this table shows that despite having seemingly less spillage, the axisymmetric geometry presents a lower mass flow rate ratio at the isolator exit, than the two-dimensional geometry, with approximately 17% less mass flow rate ratio obtained for the axisymmetric case).

5.2.2 Non-Equilibrium Chemically Reacting Flow Solution

As in 5.1.3, Park's kinetic and two temperature models were used to assess chemical dissociation and thermal non-equilibrium, respectively. Figure 5.11 plots the O and NO mass fraction distributions at the isolator exit when only chemical dissociation was considered, while figure 5.12 compares the temperature and pressure profiles at the isolator exit for the reactive and frozen flow solutions.

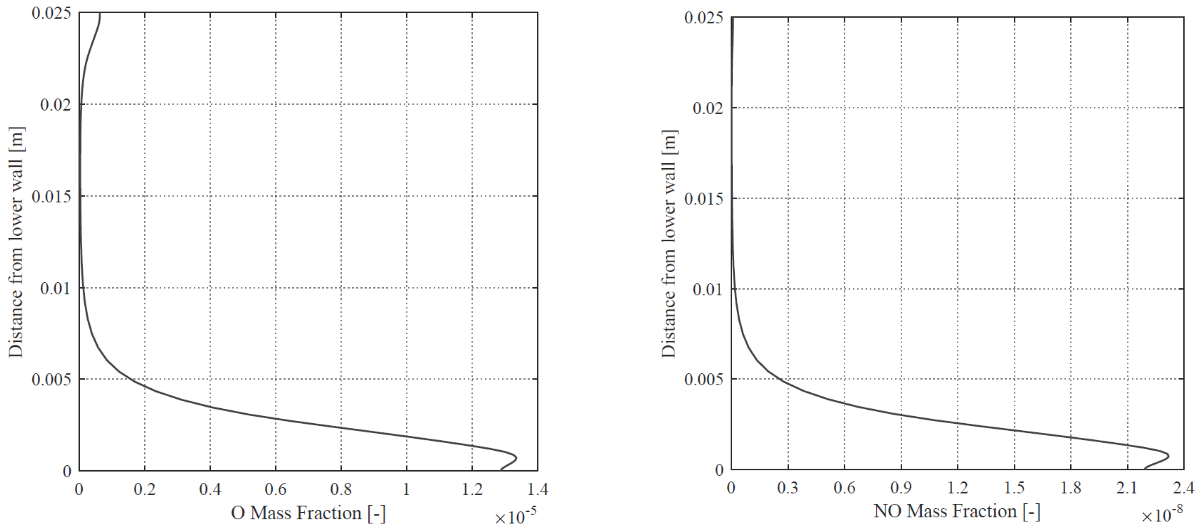

(a) O mass fraction profile at x=1.792m

(b) NO mass fraction profile at x=1.792m

Figure 5.11: O and NO mass fraction distribution at the isolator exit for the axisymmetric configuration.

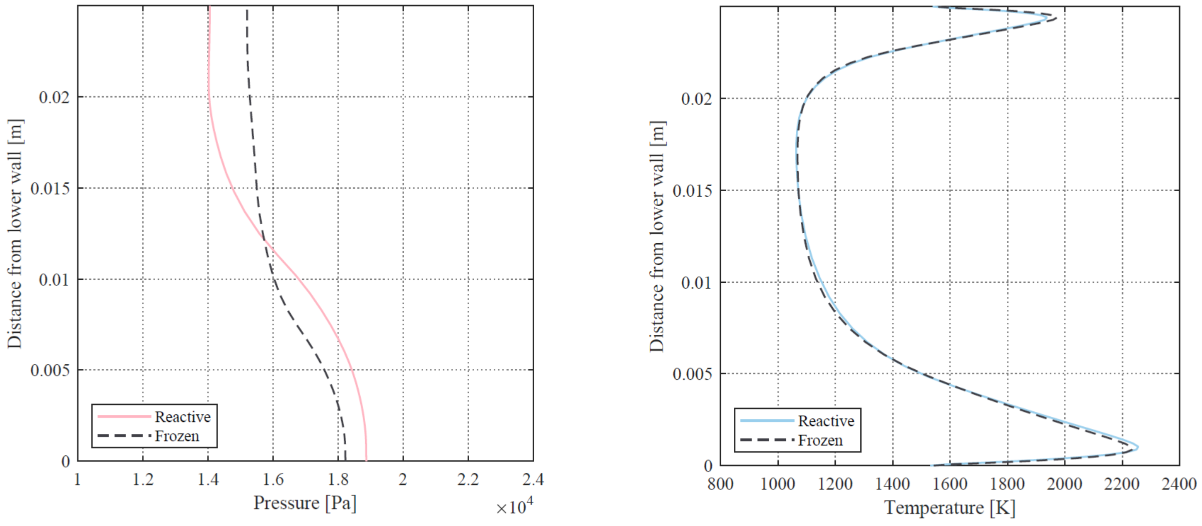

(a) Pressure profile x=1.792m

(b) Temperature profile x=1.792m

Figure 5.12: Pressure and temperature profiles of the reactive flow solution compared against the frozen flow solution for the axisymmetric configuration.

Figure 5.11, when compared to figure 5.6, shows that a smaller amount of dissociation occurs at the axisymmetric isolator exit, with the atomic oxygen mass fraction being one order of magnitude lower and the mass fraction of nitric oxide being two orders of magnitude lower than the ones obtained for the two-dimensional geometry. Nonetheless, the shape of the obtained profiles is similar for both configurations, with dissociation occurring mostly near the lower wall.

Regarding the pressure and temperature profiles at the isolator exit, figure 5.12 presents a similar behaviour to that encountered for the two-dimensional geometry, i.e. a small shift in pressure occurs, but the temperature profile does not significantly change from the one obtained for the frozen flow solution.

Thermal Non-Equilibrium: Two-Temperature Model

Similarly to what was done for the two-dimensional geometry, figure 5.13 compares the pressure and temperature distributions at the isolator exit obtained for the case of a chemically reacting flow in thermal equilibrium, with the case where thermal non-equilibrium was considered.

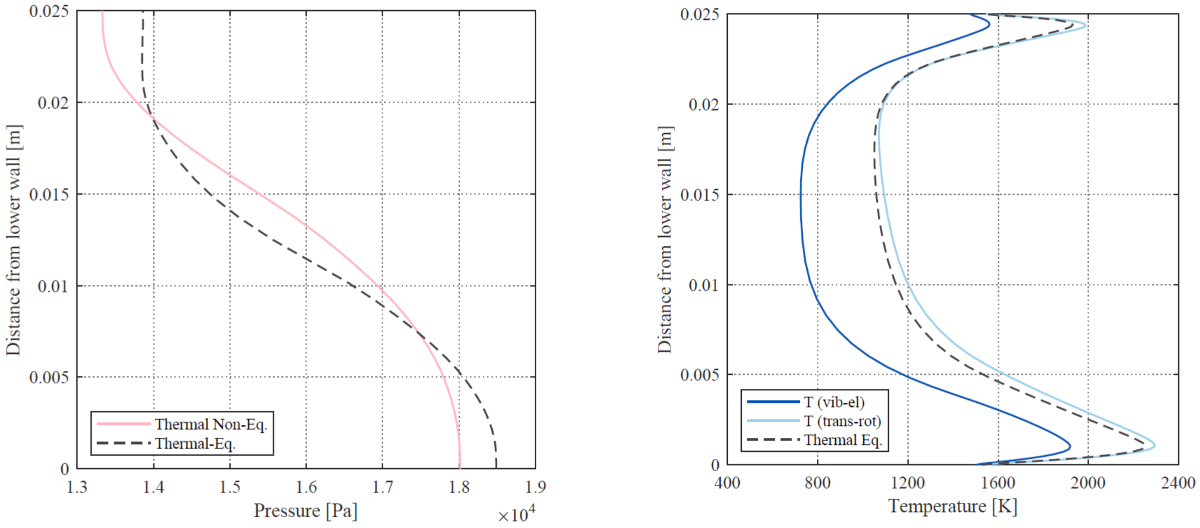

(a) Pressure profile x=1.792m

(b) Temperature profile x=1.792m

Figure 5.13: Pressure and temperature profiles of the reactive flow solution in thermal equilibrium at the isolator exit compared against the case where thermal non-equilibrium was considered for the axisymmetric configuration.

Thermal non-equilibrium is also present in the axisymmetric configuration, with translational-rotational and vibrational-electronic temperatures that differ by a maximum of 431K at the flow core (figure 5.13b), which is more than the difference obtained for the two-dimensional case. Contrarily, the translational-rotational peak-temperature, in comparison to the case of thermal equilibrium peak-temperature, is 1.83% higher, less than the obtained difference for the two-dimensional case. Lastly, regarding the pressure profile, it is shown once more in figure 5.13a that thermal non-equilibrium shifts the pressure profile at the isolator exit, although not as significantly as it did for the two-dimensional case.

The performance parameters obtained for thermal equilibrium (frozen and reactive) and thermal non-equilibrium, for the axisymmetric configuration, are presented in table 5.6. Once again, for the case of thermal non-equilibrium, the cross-sectional averaged translational-rotational temperature was used in the calculation of the performance parameters.

Case		π_c	η_{KE}	η_c	$\dot{m}_c/\dot{m}_\infty$
Thermal Equilibrium	Frozen	0.0327	0.9181	0.6833	0.6276
	Reactive	0.0305	0.9172	0.6803	0.6068
Thermal Non-equilibrium		0.0243	0.9492	0.7274	0.5906

Table 5.6: Performance parameters obtained for the thermal equilibrium and non-equilibrium solutions for the axisymmetric configuration.

Table 5.6 shows that the differences between the frozen and reactive cases are slightly higher for the axisymmetric case, with lower performance obtained for the reactive case. The same trend is observed when thermal non-equilibrium is considered, with an increase in kinetic energy efficiency and compression efficiency, and a decrease in total pressure ratio and mass flow rate ratio, the latter which is circa 1.5% lower and circa 3.5% lower, when compared to the frozen and reactive flow solutions, respectively.

A last comment that can be made is that, in general, and similarly to the two-dimensional configuration, thermal and chemical non-equilibrium effects remain limited.

5.3 Geometry Parametric Study

The previous sections assessed whether chemical dissociation and thermal non-equilibrium were present inside a two-dimensional or axisymmetric scramjet inlet, and the influence of these effects on the performance parameters and mass flow rate ratio was evaluated. In the present section, high-temperature effects will be cast aside, while the influence of geometric changes to baseline layout will be investigated. Once more, special attention will be given to the conditions at the isolator exit, since they correspond to the conditions available for combustion, and the performance parameters will be calculated and compared against the baseline geometry.

5.3.1 Two-Dimensional Configuration

Variation of the Number of Ramps

The first considered parameter was the number of ramps, as done in reference [10]. We consider the same reference three ramp geometry, with a compression/contraction ratios similar to the baseline geometry. Table 5.7 presents the design parameters for the three ramp inlet.

$\theta_1[^\circ]$	$\theta_2[^\circ]$	$\theta_3[^\circ]$	H [m]	H/h	L [m]
4.3	5.0	6.0	0.250	10	0.5

Table 5.7: Design parameters for a two-dimensional compression system with three ramps.

For this geometry, a grid similar to the one considered for the two-ramp geometry was chosen, with 175 cells in the axial direction and 60 cells in the normal direction. Moreover, the isolator was equally refined, with 90 cells along the length of this component.

The main difference between the two and three ramp inlet concerned the pressure at the isolator entry, which was higher for the three ramp inlet, despite it presenting a similar overall compression ratio. Figure 5.14 presents a detail of the pressure field, at the isolator entry, for the three ramp inlet.

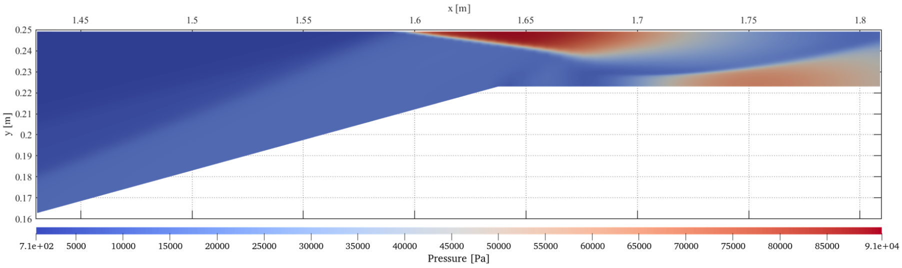

Figure 5.14: Detail of the pressure field obtained for the two-dimensional three ramp compression system, at the isolator entry.

Figure 5.14 shows that the pressure is highest at the isolator entry, as was the case for the two ramp inlet, with a maximum value of 90810.2Pa at this location. In the case of reference [10] the pressure at this location was of around 99300Pa, which represents a relative error of approximately 8.55%. Once more, this difference is expected to be a result of the identified discrepancies between how the problem was modelled in this work and in the literature (namely, wall temperature and turbulence modelling).

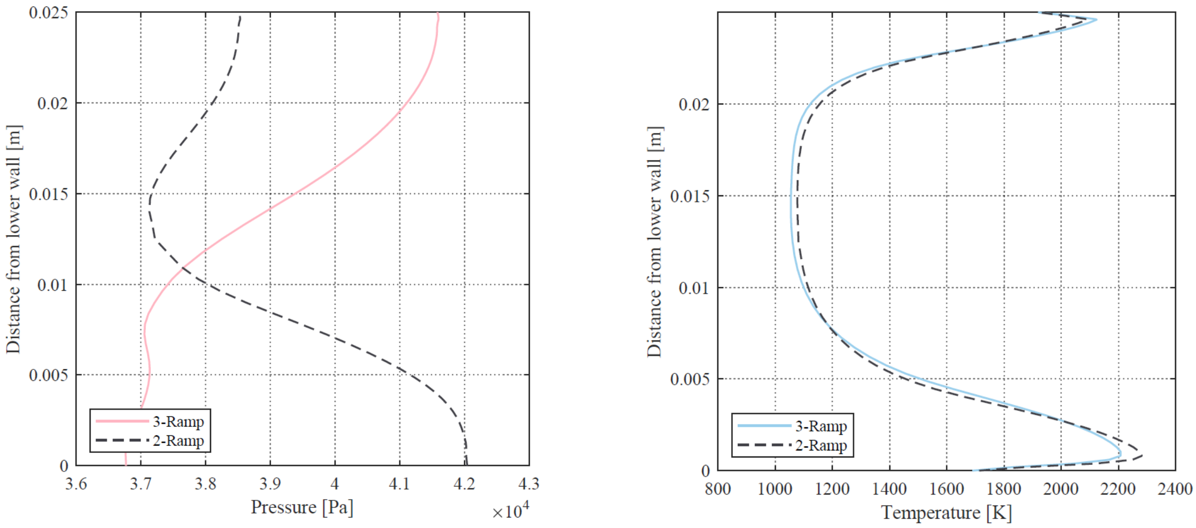

(a) Pressure profile

(b) Temperature profile

Figure 5.15: Pressure and temperature profiles at the isolator exit, for different number of ramps, for the two-dimensional configuration.

Figure 5.15 compares the pressure and temperature distributions for the different number of ramps considered. Here, it is shown that increasing the number of ramps for the same contraction and compression ratios result in a range of pressures at the isolator exit that is similar to the one obtained for the two ramp inlet. However, due to the slight change in the angle of the reflected shock waves inside the isolator, the resulting pressure profile for the three ramp inlet is shifted, with the maximum pressure being found at the upper wall, rather than the lower wall. Regarding figure 5.15b, both geometries present similar temperature profiles, with the maximum temperature being 3.24% lower for the three ramp inlet.

Lastly, the performance parameters and the mass flow rate ratio were obtained for the three ramp inlet and are compared against the ones obtained for the two ramp inlet in table 5.8.

Case	π_c	η_{KE}	η_c	$\dot{m}_c/\dot{m}_\infty$
Two Ramp	0.0793	0.9442	0.7898	0.7921
Three Ramp	0.0813	0.9449	0.7906	0.8061

Table 5.8: Performance parameters obtained for the different number of ramps, for the two-dimensional configuration.

The results show that all performance parameters slightly increase for the three ramp inlet, which evidently also result in a slight increase of the available mass flow rate for combustion. This result is also predicted, although not quantified, in reference [10]. Nonetheless, it is expected that increasing the number of ramps indefinitely will have have a limited effect on the global performance parameters.

Variation of the Compression Ratio

Another variation that can be made to the compression system concerns the ramp angles, which can be changed to obtain a different compression ratio. The case study of reference [10] consisted of a compression ratio of 4 across each of the first two oblique shock waves (PRat $=$ 4). Table 5.9 presents the design parameters for an inlet with a compression ratio of 5 across each of the first two oblique shock waves (PRat $=$ 5).

$\theta_1[^\circ]$	$\theta_2[^\circ]$	H [m]	H/h
7.9	10.7	0.250	10

Table 5.9: Design parameters for a two-dimensional compression system with a compression ratio of 5 across each of the first two oblique shock waves.

Figure 5.16a shows that increasing the compression ratio has a gain in terms of isolator exit pressure, with the average pressure remaining just below the ideal value for supersonic combustion (50kPa), at 48245Pa. On the other hand, figure 5.16b shows an undesirable increase of temperature, not only incurring in the risk of high thermal loads, but approximating the maximum allowed temperature of 1670K at the entrance to the combustor, with an average temperature of 1628.8K at this location.

Another consequence of this geometry variation is the separation bubble at the isolator entry, which is thicker for this configuration, than it was for the one with a lower compression ratio. This is attributed to the higher incidence angle over the cowl, associated with the higher compression ratio. Figure 5.17 compares the velocity and temperature fields, at the isolator entry, for both cases.

As explained for the case of an adiabatic wall condition, a larger recirculation zone increases total pressure loss and contributes to flow blockage at the entrance to the isolator.

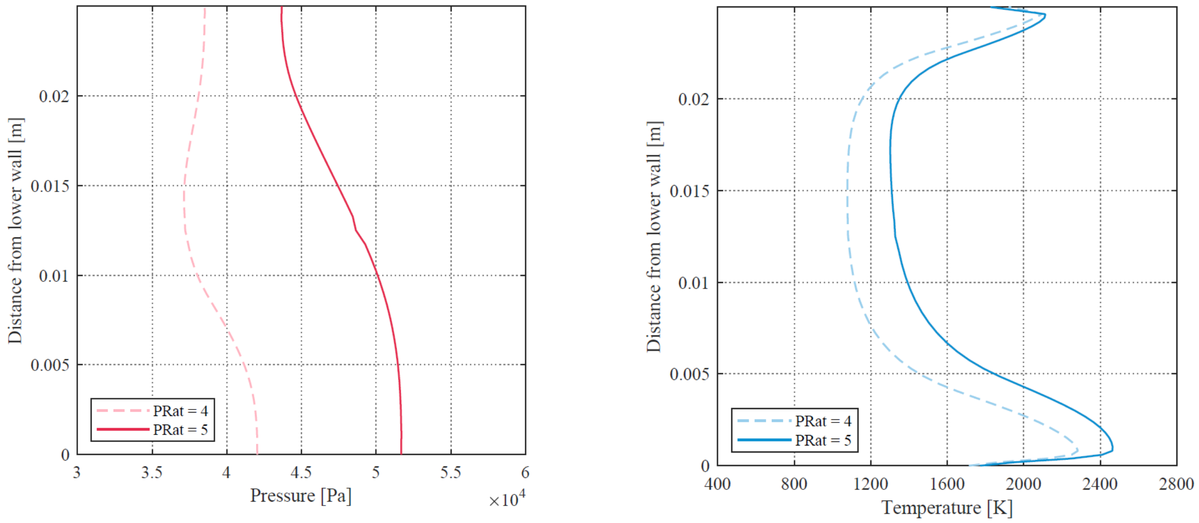

(a) Pressure profile (b) Temperature profile

Figure 5.16: Pressure and temperature profiles at the isolator exit, for different compression ratios, for the two-dimensional configuration.

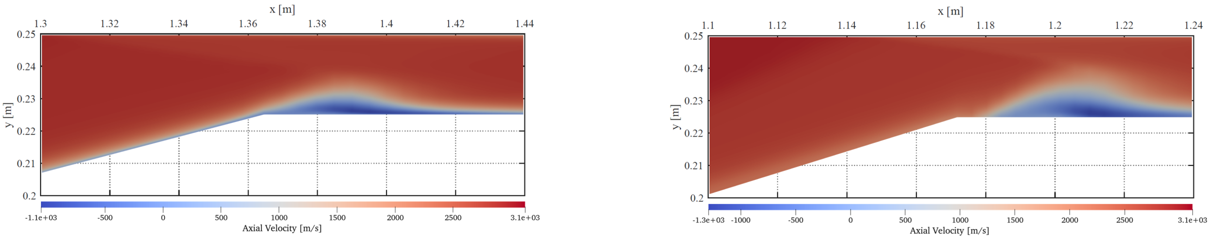

(a) PRat = 4 (b) PRat = 5

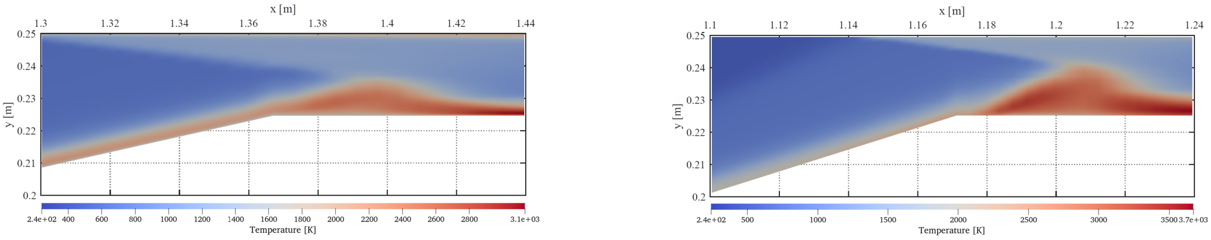

(c) PRat = 4 (d) PRat = 5

Figure 5.17: Flow separation and recirculation zones at the isolator exit for different compression ratios, for the two-dimensional configuration.

The performance parameters for the different compression ratios are presented in table 5.10, with PRat = 4 corresponding to the baseline geometry, and repeated here for convenience.

Case	π_c	η_{KE}	η_c	$\dot{m}_c/\dot{m}_\infty$
PRat = 4	0.0793	0.9442	0.7898	0.7921
PRat = 5	0.0489	0.9317	0.7878	0.7859

Table 5.10: Performance parameters obtained for the different number of ramps, for the two-dimensional configuration.

The results presented in table 5.10 are in good agreement with what was shown in figure 5.17, i.e.

a reduction of total pressure ratio is observed, a consequence of the thicker separation bubble; and accompanying it is a decrease in all other performance parameters. As expected, the mass flow rate ratio is also smaller for the geometry associated with a higher pressure ratio.

Variation of the Isolator Length

It has been previously stated (section 1.3.2) that inside the isolator pressure increases in a controlled manner, by means of an oblique shock train. Logically, increasing the length of the shock train should result in a higher exit pressure. However, and as will be shown, there is a limited amount of pressure increase that can be attained, simply by increasing the length of this component. Furthermore, excessively increasing the length of this component would only contribute to an increase of the weight and volume of the vehicle, reducing payload capabilities. Figure 5.18 presents the pressure along the centreline of the isolator, obtained for an isolator length of 1 meter, for the two-dimensional geometry. Note that, due to the increase in the physical domain, the number or cells in the isolator component had to be increased in the same amount, in order to maintain the grid resolution.

Figure 5.18 shows that, along the first 0.5 meters of the isolator, the centreline pressure increases from 12997Pa to 37223Pa, whereas in the second 0.5 meters, the increase of the centreline pressure is of only 2477Pa, from 37223Pa to 39700Pa. This shows that there is a limited amount of pressure increase that can be attained from increasing the length of the shock train, a result that is in accordance with the available literature [2].

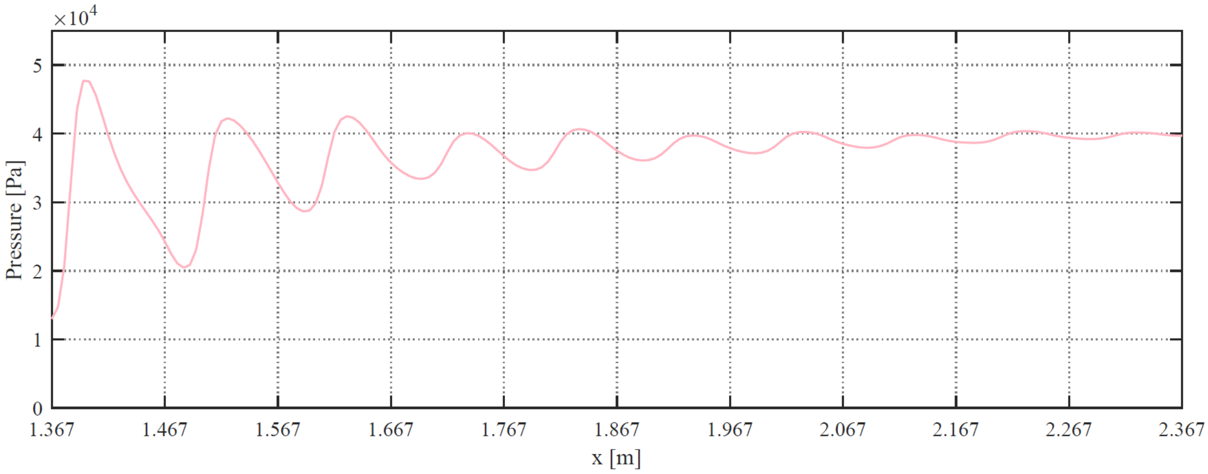

Figure 5.18: Pressure variations along the centreline of the isolator, at y=0.2375m, for an isolator length of 1m, for the two-dimensional configuration.

To assess how inlet length can affect the obtained flowfield at the isolator exit, the pressure and temperature profiles were obtained at x = 1.517m (corresponding to an isolator length of 0.15m), at x = 1.867 (corresponding to the baseline design) and at x = 2.376 (corresponding to an isolator length of 1m). The obtained results are presented in figure 5.19.

Figure 5.19 shows that for the case of a shorter isolator both the pressure and temperature profiles are still heavily affected by the impinging shock waves, resulting in very different profiles from the ones

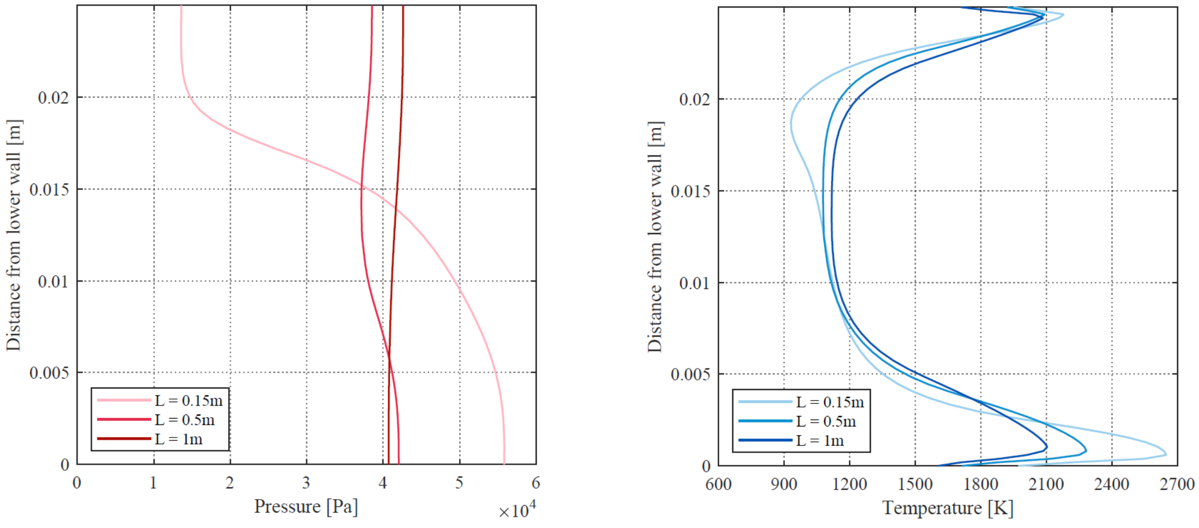

(a) Pressure profile

(b) Temperature profile

Figure 5.19: Pressure and temperature profiles at the isolator exit, for different isolator lengths, for the two-dimensional configuration.

obtained for longer isolators, with much higher pressures and temperatures near the lower wall. Contrarily, and in accordance with the results presented in figure 5.18, the longer isolator saturates, and no significant pressure increase is observed, when compared to the baseline isolator length.

The performance parameters and mass flow rate ratios were also calculated for the different isolator lengths considered and the obtained results are presented in table 5.11.

Case	π_c	η_{KE}	η_c	$\dot{m}_c/\dot{m}_\infty$
L = 0.15m	0.0983	0.9464	0.7919	0.8136
L = 0.5m	0.0793	0.9442	0.7898	0.7921
L = 1m	0.0697	0.9439	0.7915	0.7909

Table 5.11: Performance parameters obtained for the different isolator lengths, for the two-dimensional configuration.

All performance parameters and mass flow rate ratio are highest for the case of a shorter isolator. As was shown in figure 5.19, this comes at a cost of a less uniform flow at the combustor entry. Regarding the longer isolator, there is a decrease in total pressure ratio and kinetic energy efficiency, which is expected given that the flow saturates. On the other hand, the compression efficiency increases slightly, possibly a result of the slight increase in pressure, at the same approximate temperature. Lastly, mass flow rate ratio also decreases for the longer isolator length.

Variation of the Contraction Ratio

A variation of the contraction ratio may be obtained by reducing or increasing the isolator height, h. For the purpose of this work, only an increase of the contraction ratio was considered, since a decrease of this parameter would signify less compression, shifting the pressure at the combustor entrance further away from its ideal value (recall the case of the axisymmetric configuration, where the pressure at the combustor entry was not sufficient to assure ignition).

Before proceeding to the definition of a geometry with a higher contraction ratio, one must recall that the Mach number at the combustor entry must be greater than unit, for supersonic combustion to occur. To that end, an empirical formula for the Kantrowitz limit, obtained from a curve fit to the available experimental data [11], may be employed to determine the maximum contraction ratio for which the Mach number at the combustor entry is supersonic. Equation 5.1 presents that formula, which, for a freestream Mach number of 10, yields a maximum contraction ratio of 28.986.

$$\left\{\frac{\mathrm{h}}{\mathrm{H}}\right\}_{\mathrm{max}} = 0.05 - \frac{0.52}{\mathrm{Ma}_\infty} + \frac{3.65}{\mathrm{Ma}_\infty^2} \tag{5.1}$$

As described in table 2.1, the baseline geometry presented a contraction ratio, H/h, of 10. Table 5.12 gives the design parameters for a contraction ratio of 15.

Case	$\theta_1 [^\circ]$	$\theta_2 [^\circ]$	H [m]	h [m]	L [m]
H/h = 15	6.5	8.4	0.250	0.0167	0.5

Table 5.12: Design parameters for a compression system with a contraction ratio of 15, for the two-dimensional configuration.

For this geometry, it was found that the shock wave generated at the cowl tip reflected on the second ramp, rather than inside the isolator lower wall. Figure 5.20 exemplifies the generated shock wave structure for contraction ratios of 10 and 15.

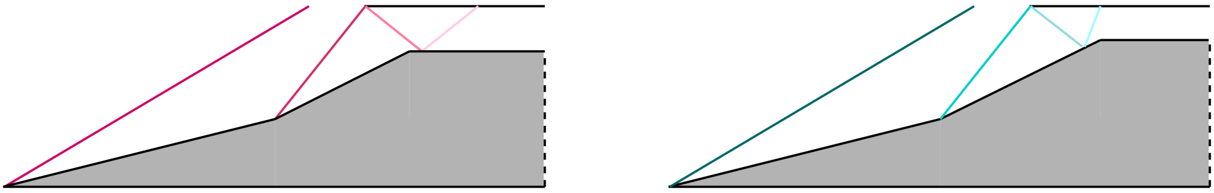

(a) H/h = 10

(b) H/h = 15

Figure 5.20: Schematics of the oblique shock wave structure for different contraction ratios, for the two-dimensional configuration (not to scale).

The reflected shock wave interacted with the boundary layer of the second ramp, which was very close due to the high contraction ratio, and originated a large flow separation bubble. The continued interaction between the reflected shock and the thick separation bubble originated a vortex, that blocked the flow at the entry to the isolator, and caused the separation bubble oscillate back and forth, just upstream the expansion corner. To better capture this phenomena, a local refinement was applied to the isolator entry, and the simulation was re-run. Due to the oscillating nature of the flow, however, the residual root mean square was found to never meet the convergence criteria, instead oscillating indefinitely around 10^{-3}. Figure 5.21 presents a detail of the pressure and temperature fields, at the isolator entry, over one time period, T, identified as 0.53 milliseconds.

While the in-depth study of this phenomena is outside the scope of this work, it was deemed impor-

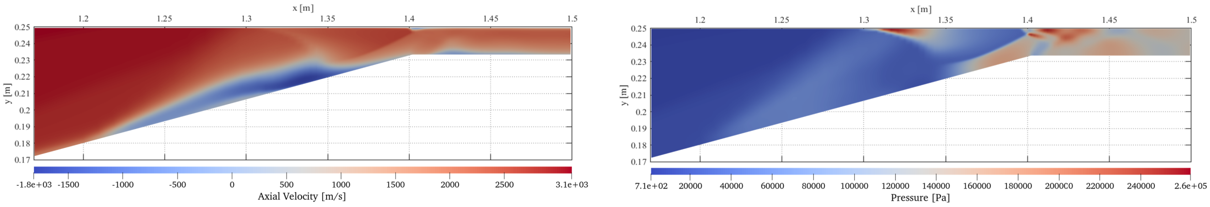

(a) Velocity at $t = 0$ (b) Pressure at $t = 0$

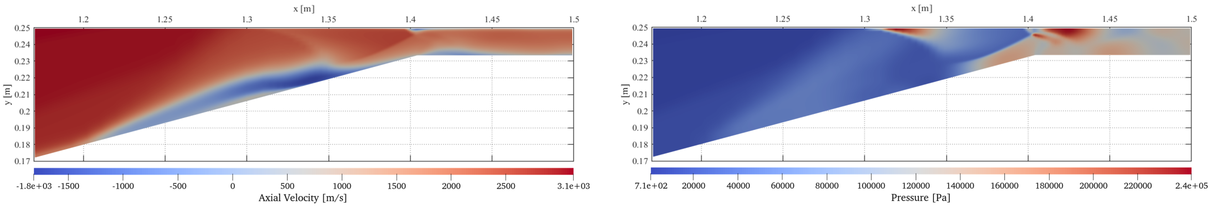

(c) Velocity at $t = 0.2T$ (d) Pressure at $t = 0.2T$

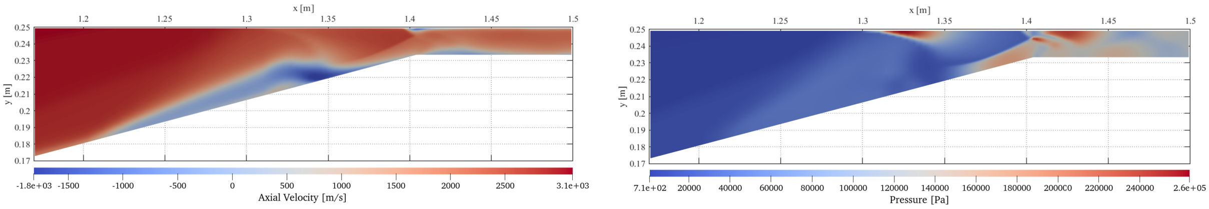

(e) Velocity at $t = 0.4T$ (f) Pressure at $t = 0.4T$

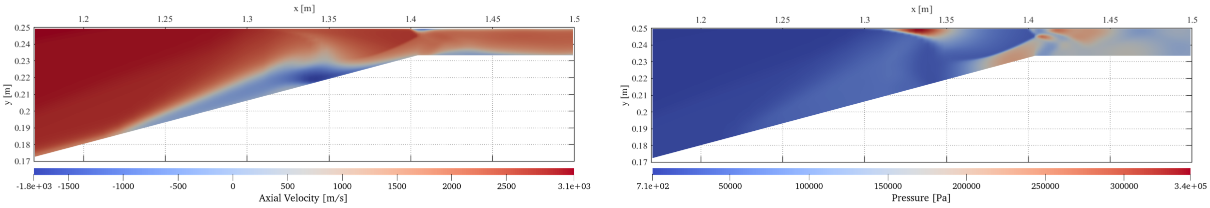

(g) Velocity at $t = 0.6T$ (h) Pressure at $t = 0.6T$

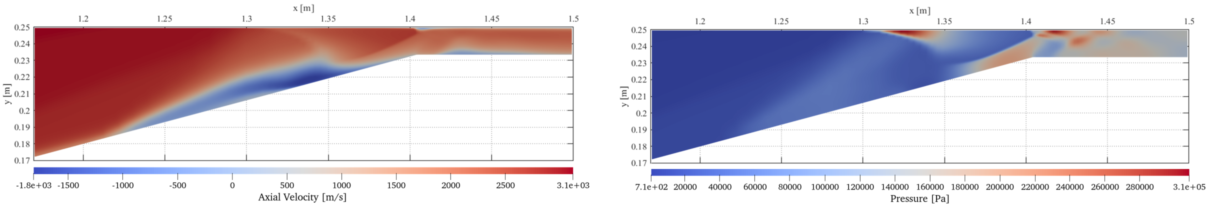

(i) Velocity at $t = 0.8T$ (j) Pressure at $t = 0.8T$

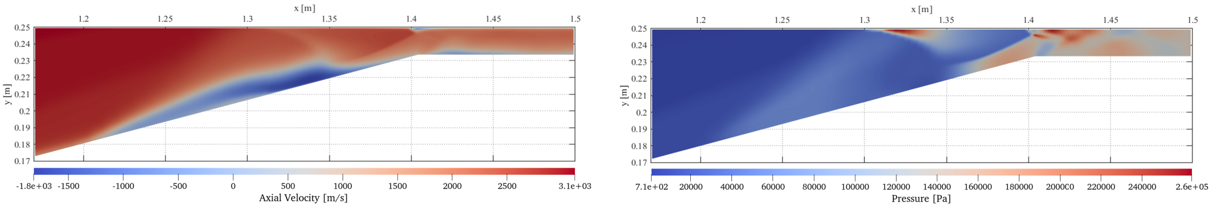

(k) Velocity at $t = T$ (l) Pressure at $t = T$

Figure 5.21: Detail of the pressure and temperature fields, at the isolator entry, over one time period, for a two-dimensional configuration with a contraction ratio of 15.

tant to search the literature for this type of instabilities in order to rule out the possibility of the obtained result to be a sole consequence of the numerical solver. Reference [34] addresses this issue experimentally for the case of a ramjet inlet, while reference [35] addresses this issue numerically for an hypersonic inlet with different throttle ratios. In both references this phenomena is referred to as inlet buzzing and is expected to cause inlet unstart, i.e. to impede the normal operation of the engine. This is in good agreement with the results presented in figure 5.21, since, as is shown for the different pressure fields presented, the shock train structure is completely destroyed due to the generated instability. Furthermore, due to oscillations at the isolator entry, the flow conditions at the entrance to the combustor also vary periodically with time. Lastly, since the inlet is unstarted, evaluating its performance had no practical value, and therefore, for this configuration, the performance parameters were not calculated.

Absence of an Expansion Corner Edge

So far, changes were made to the compression system and isolator individually, through changes in the number of ramps, ramp angles, isolator length or isolator height. The last considered geometry change focused on the location where this two components come together and where the recirculation bubble is formed: the expansion corner. Rather than having a clearly defined edge, a rounded corner, of radius 0.155m, was considered. The obtained results are presented in figures 5.22 and 5.23.

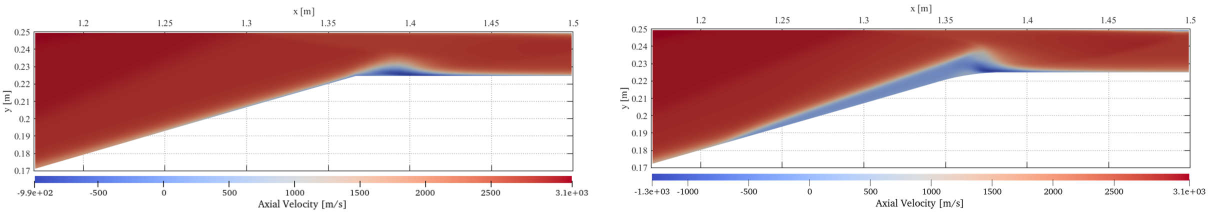

(a) With edge

(b) Without edge

Figure 5.22: Detail of the velocity field, at the isolator entry, with and without an expansion corner edge, for the two-dimensional configuration.

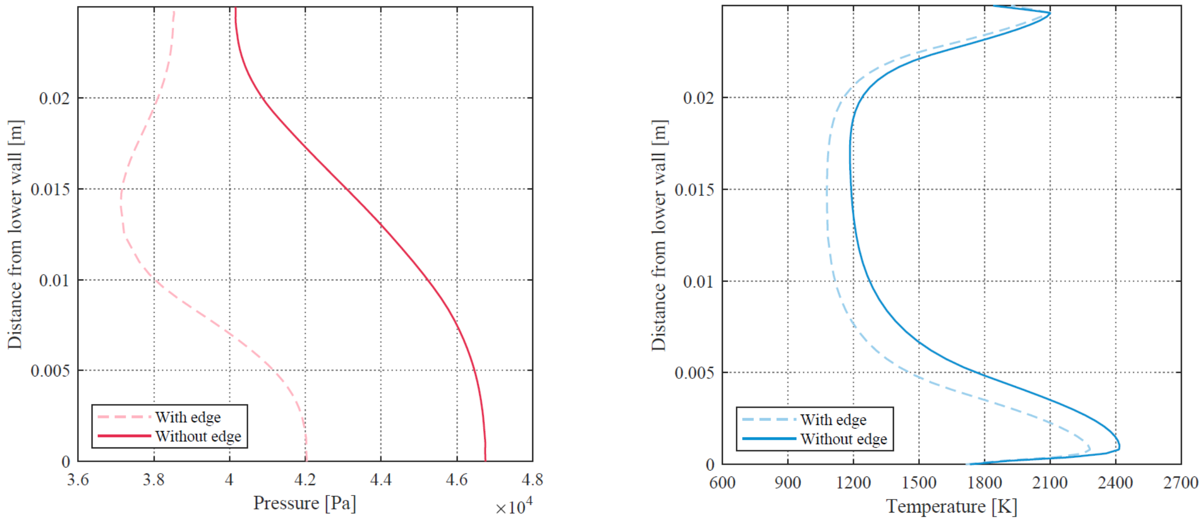

(a) Pressure profile

(b) Temperature profile

Figure 5.23: Pressure and temperature profiles at the isolator exit, with and without an expansion corner edge, for the two-dimensional configuration.

Figure 5.22 shows that, in the absence of an expansion corner edge, the flow starts to separate earlier, resulting in a thicker separation bubble at the isolator entry. Furthermore, the separation region behaves as a third ramp that generates an additional shock wave, increasing the obtained compression. This is in good agreement with the results presented in figure 5.23, where a higher pressure is displayed, at the isolator exit, for the case without an expansion corner edge. The temperature profile at this location is also affected by the geometry change, with an increase of maximum temperature of 5.87%, and an increase of average temperature of 10.57%.

The performance parameters and mass flow rate ratio at the isolator exit were also obtained for this configuration and are presented in table 5.13. The results obtained for the baseline geometry (with edge) are also repeated here for convenience.

Case	π_c	η_{KE}	η_c	$\dot{m}_c/\dot{m}_\infty$
With edge	0.0793	0.9442	0.7898	0.7921
Without edge	0.0598	0.9362	0.7869	0.7838

Table 5.13: Performance parameters obtained for the different expansion corners, for the two-dimensional configuration.

Table 5.13 shows that all performance parameters are lower for the case without an expansion corner edge. Once more, this is expected to be associated with the generated separation region at the isolator entry, which contributes to total pressure loss and increases flow blockage at this location.

While it cannot be said for sure, it is known that turbulence aids to delay separation, which means that, under a turbulence model, this geometry might have presented better performance than the geometry with a clearly defined edge. The recalculation of this solution, once an appropriate turbulence model has been implemented in SPARK, will be left as a suggestion for future work.

5.3.2 Axisymmetric Configuration

For the axisymmetric configuration, it was expected that all geometry variations presented a similar behaviour to the ones encountered for the two-dimensional layout, except for the case where the contraction ratio was varied. As will be recalled, for the two-dimensional configuration, when the contraction ratio was increased, the oblique shock wave generated at the cowl tip reflected on the second ramp, upstream the isolator entry, interacted with the thick boundary layer, and caused inlet unstart (figure 5.21). For the axisymmetric configuration, however, when a contraction ratio, H/h, of 10 was used, it was found that the cowl tip shock reflected well inside the isolator (figure 5.9). Therefore, there is still a comfortable margin for increasing the contraction ratio, without risking the chance of inlet unstart. Table 5.14 presents the design parameters for an axisymmetric inlet with contraction ratios of 15 and 25.

In table 5.14, all chosen contraction ratios fall below the maximum contraction ratio defined by the Kantrowitz limit (equation 5.1). Furthermore, the smallest contraction ratio considered, corresponded to an isolator height of 10mm, approximating that of the HyShot-2 supersonic combustion test, which presented an isolator height of 9.8mm [36]. Since the flow conditions for the HyShot-2 experiment combustor entrance fall within the expected values presented in section 2.2, it was considered that an isolator

Case	ϑ_1[°]	ϑ_2[°]	H [m]	h [m]	L [m]
H/h = 15	8.6	11.3	0.250	0.0167	0.5
H/h = 25	8.6	11.3	0.250	0.0100	0.5

Table 5.14: Parameters for the considered cowl heights for the axisymmetric configuration.

height of 10mm did not prevent supersonic combustion from taking place and therefore constituted a feasible option.

Pressure along the isolator centreline is plotted in figure 5.24, for the three considered contraction ratios; figure 5.25 plots the pressure and temperature profiles at the isolator exit, and figure 5.26 shows a detail of the axial velocity fields, at the isolator entry, obtained for the contraction ratios of 15 and 25.

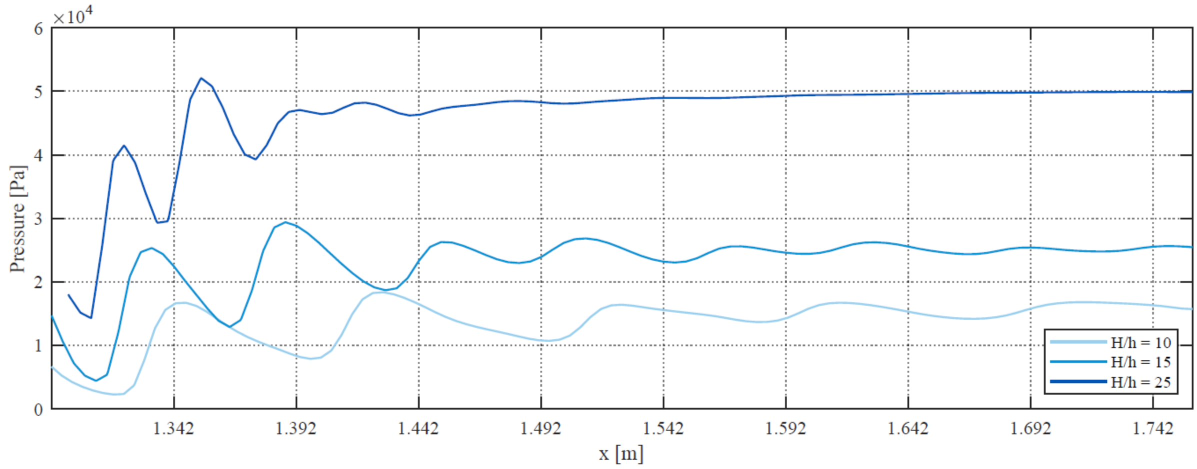

Figure 5.24: Pressure variations along the centreline of the isolator for different contraction ratios, for the axisymmetric configuration.

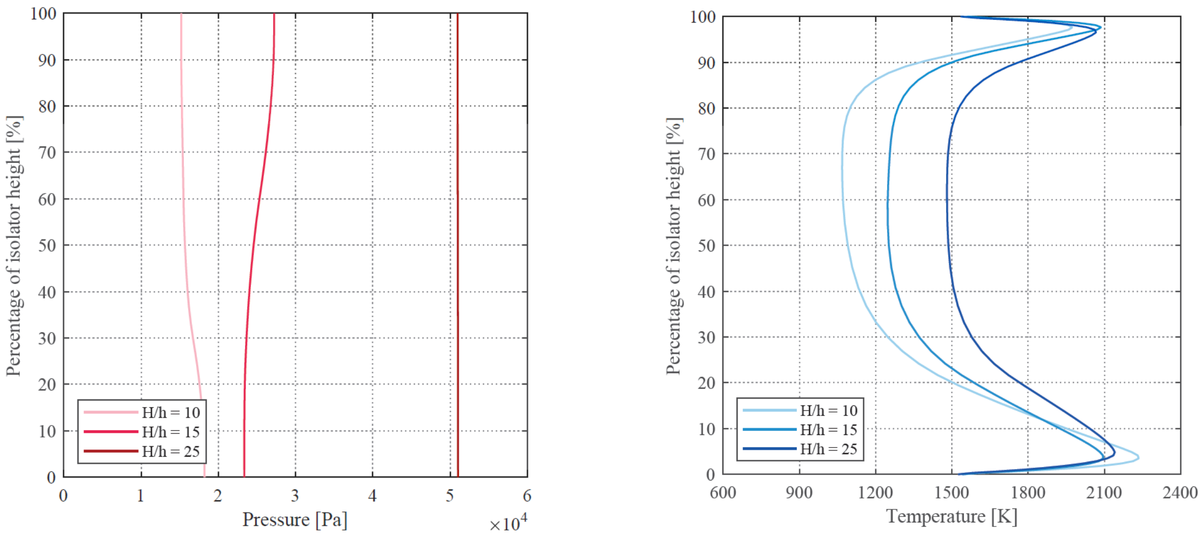

(a) Pressure profile

(b) Temperature profile

Figure 5.25: Pressure and temperature profiles at the isolator exit, for different contraction ratios used in the axisymmetric geometry.

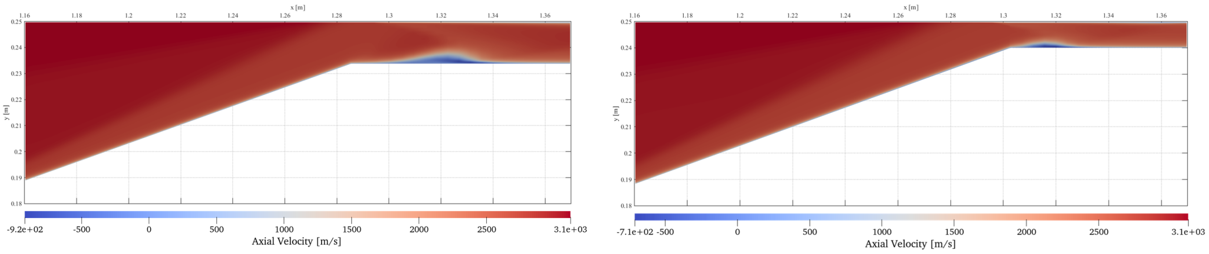

(a) H/h = 15 (b) H/h = 25

Figure 5.26: Flow separation and recirculation zones at the isolator entry for different compression ratios, for the axisymmetric configuration.

Figure 5.24 shows that, expectedly, increasing the contraction ratio, i.e. decreasing the isolator height, results in an increase of the frequency at which the shock waves reflect inside the isolator. Furthermore, as the contraction ratio increases, so does the pressure in the isolator, mostly near the entry. This means that a smaller isolator height might require a shorter isolator length, and therefore constitute a lighter vehicle.

Figure 5.25 shows that the increase of contraction ratio leads to a desirable increase in pressure at the isolator exit, which falls within the necessary values for ignition for the cases of H/h of 15 and 25, but also an increase of the flow core temperature. For the highest contraction ratio, the flow core temperature was of 1500K, and the flow average temperature was of 1662K, much closer to the high end of the range of maximum allowed temperatures at the combustor entrance, defined in section 4.2.2.

Lastly, figure 5.26 shows that, as the contraction ratio is increased, the separation bubble moves upstream, towards the isolator entry. This suggests that, had we increased the contraction ratio further, an instability similar to the one found for the two-dimensional configuration might have occurred.

The performance parameters of section 3.3 and mass flow rate ratio were also calculated for each of the contraction ratios considered and are presented in table 5.15.

Case	π_c	η_{KE}	η_c	$\dot{m}_c/\dot{m}_\infty$
H/h = 10	0.0327	0.9181	0.6833	0.6276
H/h = 15	0.0350	0.9226	0.7285	0.5885
H/h = 25	0.0382	0.9314	0.7913	0.5975

Table 5.15: Performance parameters for the considered cowl heights for the axisymmetric configuration.

The results of table 5.15 show that the increase of contraction ratio is accompanied by an increase of compression system efficiency, with improvement across all three performance parameters. Regarding the mass flow rate ratio, the results show that, despite the decrease of exit area, the efficiency increase allowed for similar mass flow rate ratios among the different contraction ratios considered. Lastly, it can be noted that despite the overall increase in performance, even at the highest contraction ratio, the performance of the axisymmetric inlet still remains below that of the baseline geometry for the two-dimensional configuration.

5.4 Off-Design Conditions

In section 2.1 it was stated that a typical required operating range for a supersonic combustion ramjet falls in the Mach 6-10 range. The present section assesses how the performance is affected for a different trajectory point. For that purpose, the baseline geometry for the two-dimensional configuration will be used, whereas for the axisymmetric configuration, the geometry with a contraction ratio H/h = 25 was chosen, since the baseline geometry did not allow for fuel ignition at the combustor.

5.4.1 Off-design trajectory point: Mach 7

Table 5.16 presents the upstream boundary conditions for off-design trajectory points for freestream Mach numbers ranging from 6 to 10, obtained for an atmospheric dynamic pressure of 50kPa.

Ma	u[km/s]	p[Pa]	T[K]	x_{N_2}	x_{O_2}	Species Involved
6	1.80	1987	225	0.79	0.21	N_2, O_2, N, O, NO
7	2.13	1460	229	0.79	0.21	N_2, O_2, N, O, NO
8	2.42	1118	233	0.79	0.21	N_2, O_2, N, O, NO
9	2.78	883	237	0.79	0.21	N_2, O_2, N, O, NO
10	3.11	714	240	0.79	0.21	N_2, O_2, N, O, NO

Table 5.16: Upstream conditions for off-design trajectory points, for freestream Mach numbers ranging from 6 to 10, for a dynamic pressure of 50kPa [10, 28].

The table presented above shows that the freestream conditions can vary significantly along the expected trajectory for scramjet operation, and therefore it is of relevance to assess how the compression system behaves under these conditions. For that purpose, the selected geometries were simulated at freestream conditions corresponding to a trajectory point of Mach 7.

Two-Dimensional Configuration

A few adjustments must be made before proceeding to the obtained solution for the off-design trajectory point. As will be recalled from section 4.3, the grid configuration selected for all previous simulations presented a physical domain that was the minimum necessary to fully capture the first oblique shock. For different freestream Mach numbers, the angle of the first oblique shock will vary, and it no longer makes sense to use the grid configuration displayed in figure 4.2. Instead, another grid configuration was chosen to assess the behaviour of the flow at off-design conditions (figure 5.27). This configuration retains the same 175x60 cell distribution defined in the mesh convergence study for the two-dimensional geometry, which allowed for the resolution of the isolator to remain unchanged.

Figure 5.28 compares the pressure and temperature profiles as a function of the vertical distance from the second ramp wall, at x = 1.1m, for the two grid configurations, for the trajectory point of Mach 10, while figure 5.29 presents the pressure and temperature profiles at the isolator exit, for the same trajectory point.

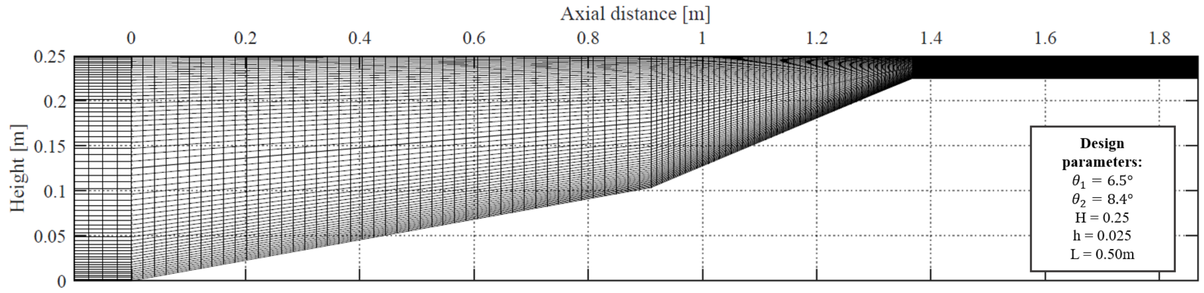
Axial distance [m]
0
0.2
0.4
0.6
0.8
1
1.2
1.4
1.6
1.8
Height [m]
0.25
0.2
0.15
0.1
0.05
0
Design parameters:
$\theta_1 = 6.5°$
$\theta_2 = 8.4°$
H = 0.25
h = 0.025
L = 0.50m

Figure 5.27: Adapted grid configuration used to assess performance at different freestream conditions, for the two-dimensional configuration.

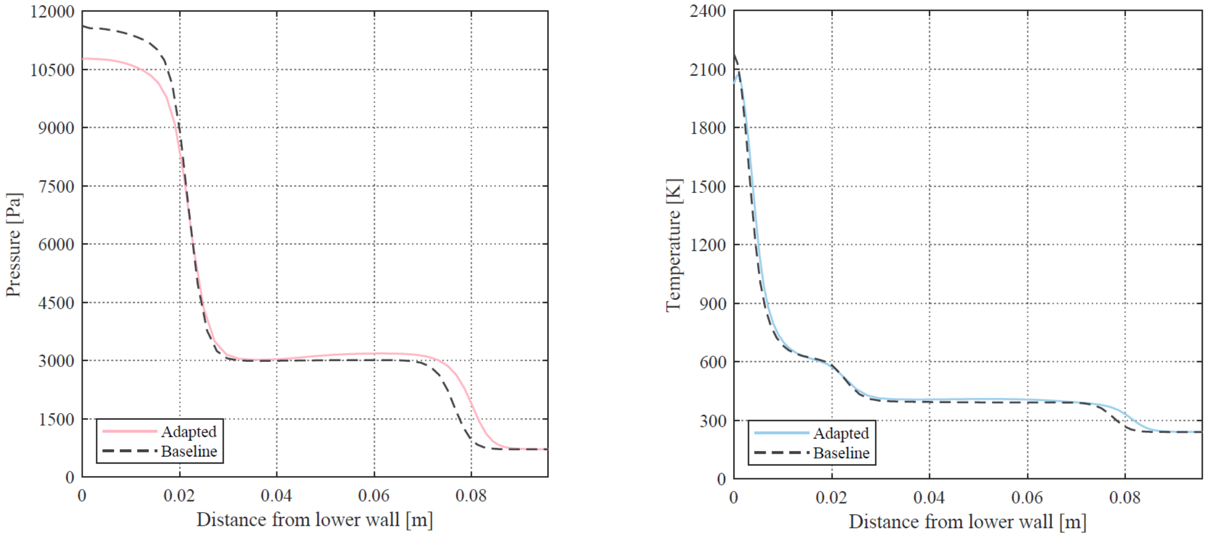

(a) Pressure profile

(b) Temperature profile

Figure 5.28: Pressure and temperature profiles, at x=1.1m, for the baseline and adapted grid for the two-dimensional configuration.

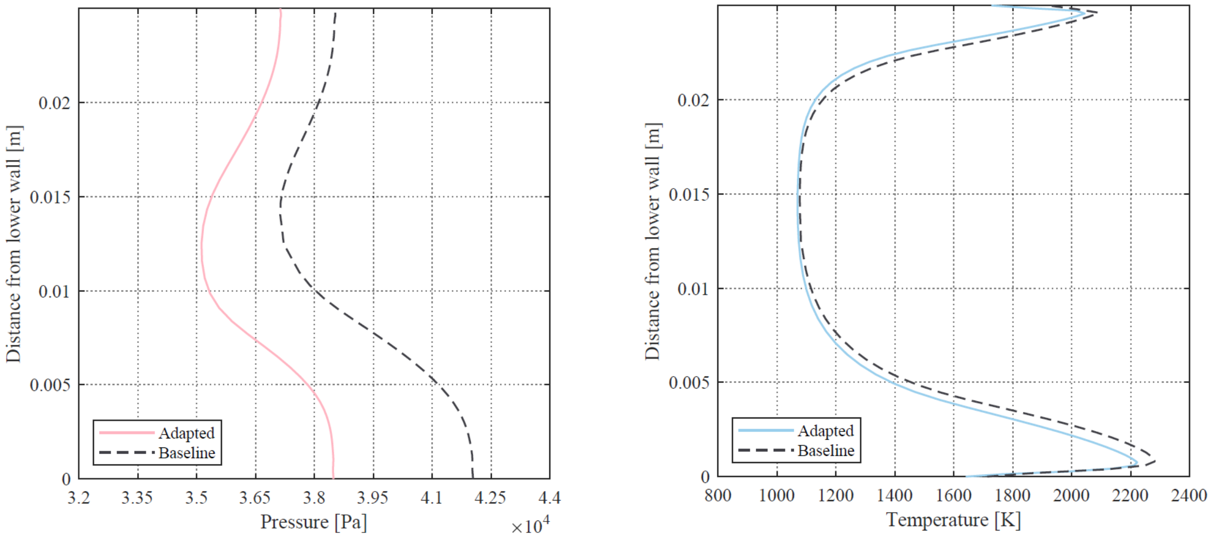

(a) Pressure profile

(b) Temperature profile

Figure 5.29: Pressure and temperature profiles at the isolator exit for the baseline and adapted grid, for the two-dimensional configuration.

As expected, figure 5.28 shows that the adapted grid configuration resulted in an error in terms of the position of the oblique shock waves, generated by the compression system ramps, and, consequently, an associated error at the obtained temperature and pressure after each oblique shock, with a maximum relative error of 7.31% obtained for the value of the pressure after the second oblique shock.

Figure 5.29 compares the pressure and temperature profiles at the isolator exit, and shows that, as a result of the grid adaptation, the conditions at this location, which will be used to determine performance, also present an error relative to the baseline grid. This error is most relevant in terms of pressure, which is under predicted by 8.45% at the lower wall of the isolator. The obtained temperature profile incurs in a smaller maximum error, of circa 2.59%, at the lower wall thermal boundary layer.

For the purpose of this work, it was found that the obtained errors were acceptable, as we are mainly interested in providing a qualitative estimative of how performance is affected by operation at off-design conditions. Figure 5.30 presents the pressure, density and temperature fields obtained for a trajectory point of Mach 7, while in figure 5.31 the pressure and temperature profiles, at the isolator exit, obtained for the trajectory point of Mach 7 are compared against the results obtained for the trajectory point of Mach 10, for the same grid configuration.

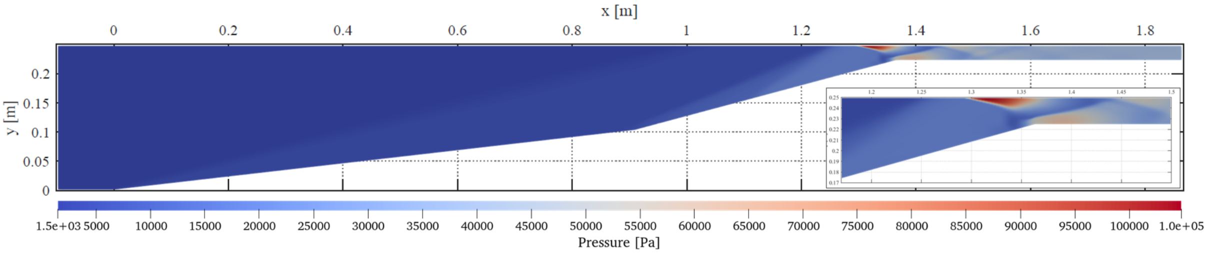

(a) Pressure field

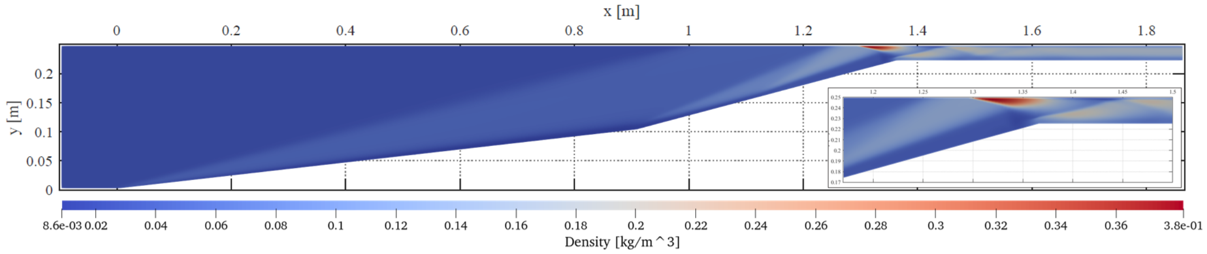

(b) Density field

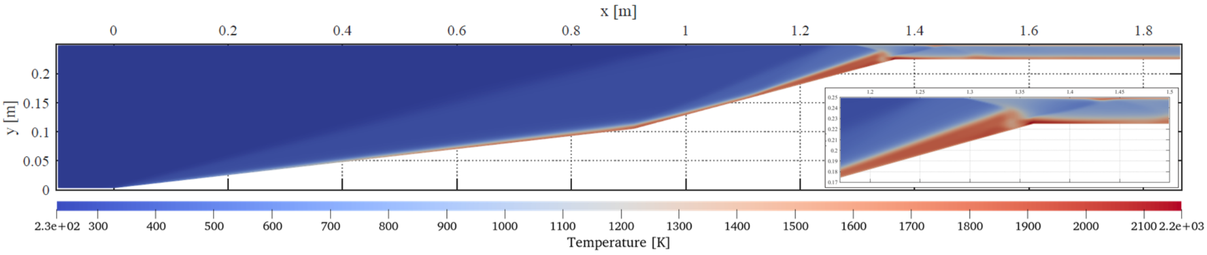

(c) Temperature field

Figure 5.30: Pressure, density and temperature fields obtained for the viscous (Navier-Stokes) frozen-flow simulation of the two-dimensional compression system, at a trajectory point of Mach 7.

As expected, for an off-design Mach number which is lower than the design Mach number, a greater amount of spillage occurs. Nonetheless, it was found possible to have a started inlet for the selected trajectory point, with the generated recirculation region at the isolator entry being very similar to the one obtained for the rounded expansion corner.

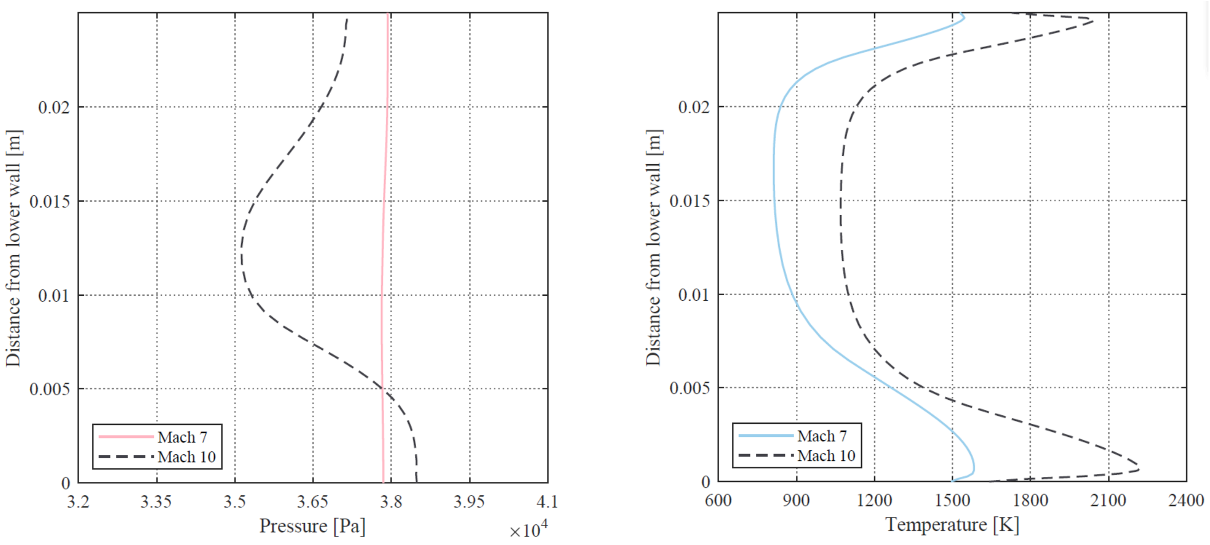

(a) Pressure profile

(b) Temperature profile

Figure 5.31: Pressure and temperature profiles at the isolator exit, for different trajectory points, for the two-dimensional configuration, obtained from the adapted grid.

Figure 5.31 shows that, for freestream conditions of Mach 7, the flow is at a nearly constant pressure, at the isolator exit, which indicates that the flow is saturated. With this said, the average pressure at this location falls within the necessary values for ignition to occur, once more showing that this configuration is capable of operating for the selected trajectory point. On the other hand, the obtained temperatures at the isolator exit are much lower for this trajectory point. While this may imply a lesser chance of incurring in high thermal loads, it may also mean that a greater combustor length may be necessary to ensure that sufficient thrust is generated for this trajectory point.

The performance parameters and mass flow rate ratios were calculated for the different trajectory points and are presented in table 5.17. It is worth noting that the values presented for Mach 10 were recalculated from the data obtained for the adapted grid, to allow for a proper comparison.

Case	π_c	η_{KE}	η_c	$\dot{m}_c/\dot{m}_\infty$
Mach 10	0.0833	0.9458	0.7880	0.7718
Mach 7	0.0896	0.8920	0.7370	0.4381

Table 5.17: Performance parameters obtained for different trajectory points, for the adapted grid, for the two-dimensional configuration.

The results show that, for freestream conditions of Mach 7 there is an increase of total pressure ratio, and a decrease of kinetic energy efficiency and compression efficiency. The loss in mass flow rate ratio is more significant, being over 30% lower for the trajectory point of Mach 7. To counter this effect, variable geometries are typically considered, which help reduce flow spillage and therefore increase the available mass flow rate at the combustor entry, at the cost of a heavier, more complex vehicle.

Axisymmetric Configuration

As was done for the two-dimensional configuration, an adapted grid was employed for the study of the selected off-design trajectory point for the axisymmetric configuration with a contraction ratio H/h of 25. Figure 5.32 plots the pressure and temperature profiles, at x = 1.2m, as function of the vertical distance from the ramp wall, while figure 5.33 presents the pressure and temperature profiles, at the isolator exit, obtained for the baseline and adapted grid, at a trajectory point corresponding to Mach 10.

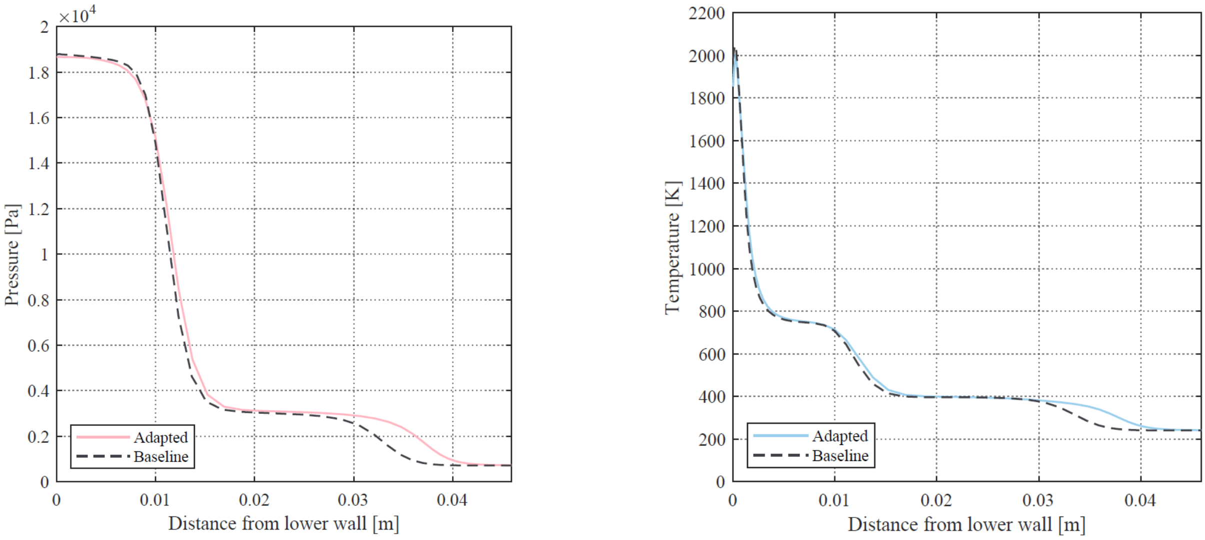

(a) Pressure profile

(b) Temperature profile

Figure 5.32: Pressure and temperature profiles, at x = 1.2m, for the baseline and adapted grid, for the axisymmetric configuration.

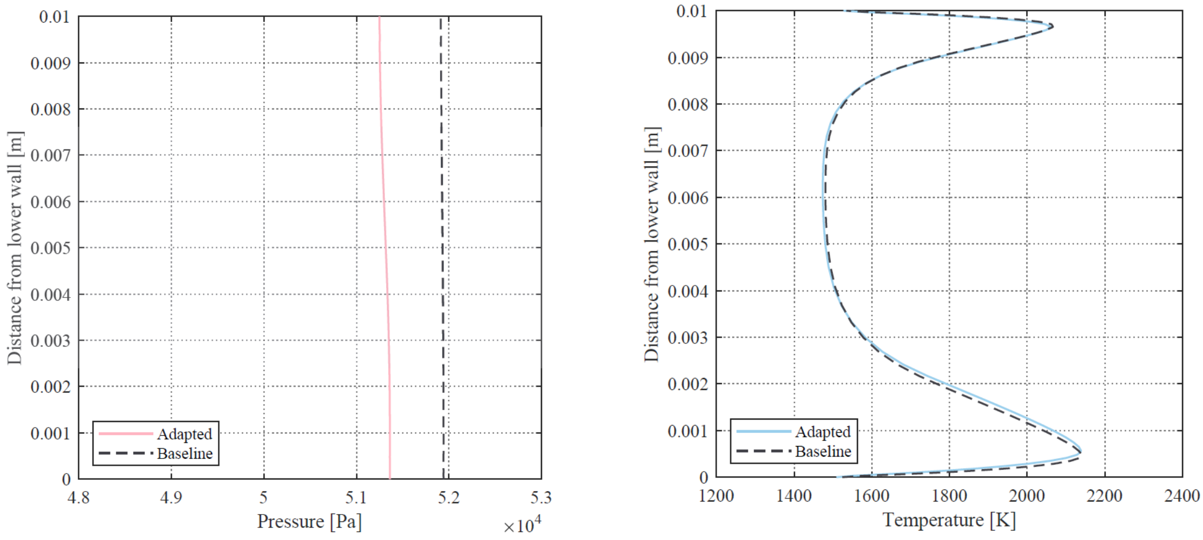

(a) Pressure profile

(b) Temperature profile

Figure 5.33: Pressure and temperature profiles at the isolator exit for the baseline and adapted grid, for the axisymmetric configuration.

As was the case for the two-dimensional geometry, it was found that a small error in terms of the position of the oblique shock waves occurs for the case of the adapted grid. Contrarily to what happened for the two-dimensional configuration, the pressure after the second ramp remains approximately the same for both considered grids. This was attributed to the fact that the axisymmetric configuration possesses a greater number of cells in the axial direction than the two-dimensional configuration. Regarding the property profiles at the isolator exit, results similar to the ones presented for the two-dimensional configuration were obtained, i.e. the temperature profile is nearly coincidental with the one obtained obtained for the baseline grid, while the pressure is slightly lower.

Once more, for the purpose of this work, the obtained relative errors were found to be acceptable to allow for a qualitative estimative of how performance is affected by operation at off-design conditions. Figure 5.34 presents the pressure, density and temperature fields obtained for a trajectory point of Mach 7, while figure 5.35 plots the pressure and temperature profiles, at the isolator exit, for the operating point of Mach 7 against those obtained for the design point Mach number, for the same grid configuration.

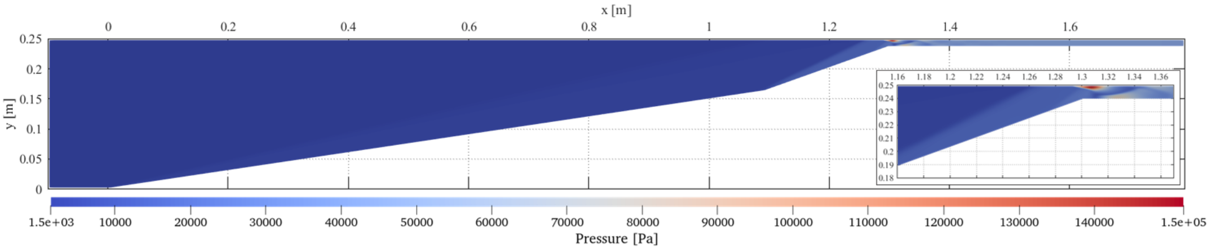

(a) Pressure field

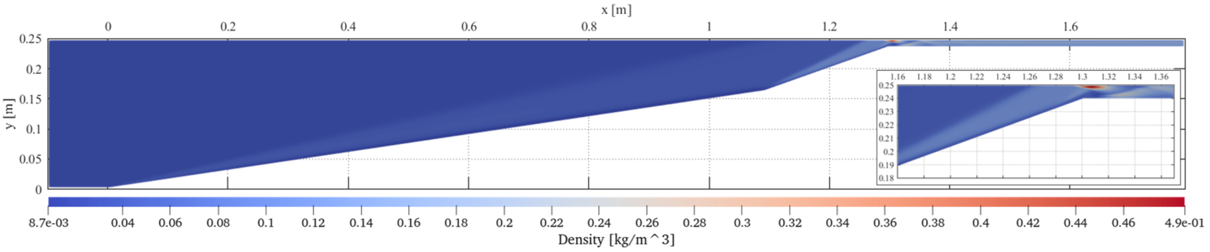

(b) Density field

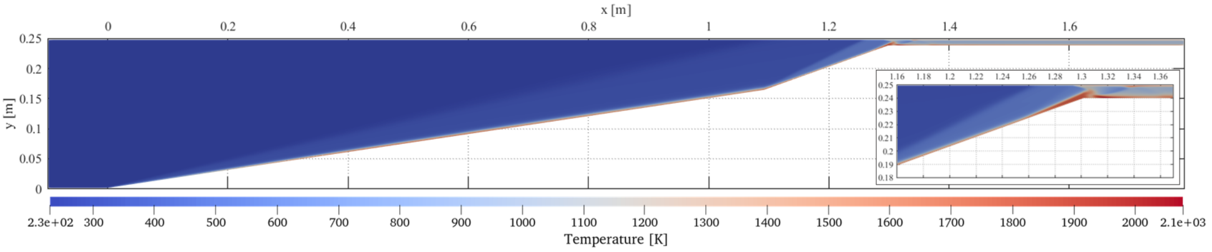

(c) Temperature field

Figure 5.34: Pressure, density and temperature fields obtained for the viscous (Navier-Stokes) frozen-flow simulation of the axisymmetric compression system, at a trajectory point of Mach 7.

As was the case for the two-dimensional configuration, figure 5.34 shows that, for a trajectory point of Mach 7, a greater amount of spillage occurs. For this configuration, a thicker recirculation zone is also formed at the entry to the isolator, however this does not seem to lead to inlet unstart. Lastly, for both configurations, the obtained maximum pressures at Mach 7 were higher than the ones obtained for the design point freestream conditions, whereas the obtained maximum temperatures were lower. This may mean that, as pertains to the structural design, it might be relevant to consider the lower end of the operating range, so as to ensure that the vehicle withstands all mechanical loads for the trajectory.

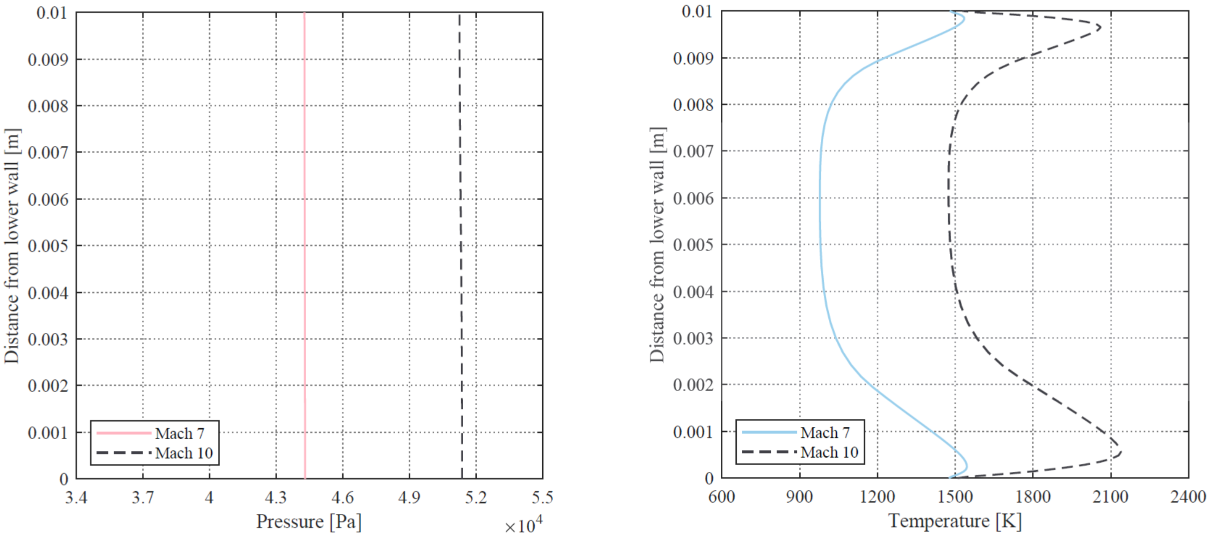

(a) Pressure profile

(b) Temperature profile

Figure 5.35: Pressure and temperature profiles at the isolator exit, for different trajectory points, for the axisymmetric configuration, obtained from the adapted grid.

For a trajectory point of Mach 7, figure 5.35a shows that the pressure profile is constant at the isolator exit. This indicates that the flow is saturated and it is not an unexpected result, given that the same occurred for the two-dimensional configuration. Furthermore, the pressure is slightly lower for this trajectory point than it was for the design Mach number. This was not considered to be problematic, since the obtained value is considered to still allow for ignition to occur. Figure 5.35b shows that, as was the case for the two-dimensional configuration, the obtained temperatures at the isolator exit are lower for a trajectory point of Mach 7.

The performance parameters obtained for the axisymmetric configuration at an operating point of Mach 7 are compared in table 5.18 against the obtained values for the design point Mach number, which have been recalculated here for the adapted grid configuration, to allow for comparison.

Case	π_c	η_{KE}	η_c	$\dot{m}_c/\dot{m}_\infty$
Mach 10	0.0358	0.9316	0.7920	0.5922
Mach 7	0.0884	0.8914	0.7350	0.3355

Table 5.18: Performance parameters obtained for different trajectory points, for the adapted grid, for the axisymmetric configuration.

Once more, table 5.18 presents similar trends to the ones obtained for the two-dimensional configuration. At a trajectory point of Mach 7, the total pressure ratio increases, much more significantly than it did for the two-dimensional case, while all other performance parameters decrease, with particular attention drawn to the mass flow rate ratio, which is nearly halved for the selected trajectory point. Once more, a variable geometry might help to increase the available mass flow rate at the combustor entry.

Chapter 6

Conclusions

This chapter summarizes the results and achievements that were presented throughout the rest of the present document, and provides some recommendations for future work.

6.1 Achievements

This work provided an insight of what it is like to work with a CFD code that is still under development. As a consequence, it was important to bear in mind the limitations of such a code when analysing the obtained results. Identified model shortfalls include the discretization of the domain, which had to be a compromise between sufficient refinement to capture all present phenomena and computational times; the absence of a turbulence model, which could have played a significant role in delaying separation at the isolator entry; and, finally, the impossibility to test three-dimensional geometries.

In spite of these shortfalls, it was possible to model the flow inside the compression system of a scramjet engine at Mach 10, and to reproduce a case study from the literature, with some minor discrepancies in terms of the peak pressure at the cowl tip, and exit pressure at the combustor entry, but with the same overall behaviour of the flow. It was found that the thick boundary layer increases the angle of the oblique shock waves, generating spillage for the design point Mach number, a result which is in good agreement with the literature, where it is suggested that this result might avoid a hot spot on the cowl tip, and therefore be beneficial for the overall endurance of the aircraft.

The impact of wall temperature, dissociation and thermal non-equilibrium was also studied for the two-dimensional configuration extracted from the literature. It was found that the choice of an adiabatic wall leads to unrealistically high temperatures, and decreases the efficiency of the inlet, whereas a lower wall temperature benefits performance. Chemical dissociation was also found to be present within the studied compression system, however the obtained mass fractions were of low orders of magnitude, and were found to not significantly affect performance, which indicates that such effects might be neglected to spare computational power. One must, however, still keep in mind that the formation of nitric oxide occurs and will contribute to the destruction of the ozone layer. Thermal non-equilibrium was, on the other hand, found to be significant, with translational-rotational and vibrational-electronic temperatures that differed by a maximum of 309.4K. Thermal non-equilibrium was also found to affect performance through the reduction of total pressure ratio and mass flow rate ratio, and increase of kinetic energy and compression efficiencies.

Similar studies were conducted for an axisymmetric configuration, whose design parameters were obtained through the Taylor Maccoll analysis in order to attain the same compression and contraction ratios as the two-dimensional configuration from the literature. From the frozen flow solution for this layout, it was found that the conditions at the isolator exit did not meet the criteria for fuel ignition at the combustor, with pressure being significantly lower than the one obtained for the two-dimensional configuration. Regarding the chemically reactive and thermal non-equilibrium solutions, the same conclusion than for the two-dimensional case apply, with dissociation being of low orders of magnitude, but with prominent thermal non-equilibrium, with translational-rotational and vibrational-electronic temperatures that differed by a maximum of 431K. Lastly, regarding performance, the main conclusion was that for the same compression and contraction ratios, the axisymmetric configuration presented worse performance parameters than the two-dimensional one. Dissociation and thermal non-equilibrium effects were found to affect performance in a similar manner to the one encountered for the two-dimensional configuration.

The conducted geometry parametric study discussed the impact of several geometric parameters on the behaviour of the flow within the compression system, as well as their impact on performance. It was found that an increase in the number of ramps slightly improves performance and increases the available mass flow rate ratio at the combustor entry, whereas an increase of the compression ratio, achieved by an increase of the ramp angles, was found to decrease all performance parameters and mass flow rate ratio. Regarding the variations applied to the isolator, it was found that a shorter isolator length presents an overall better performance, at the cost of a less uniform flow at the combustor entry, whereas a longer isolator leads to a limited amount of pressure increase, and does not necessarily translate into better performance. In terms of the increase in contraction ratio, which was achieved by decreasing the isolator height, it was found that a contraction ratio H/h of 15 resulted in a strong shock boundary layer interaction, which led to inlet unstart. For the axisymmetric inlet, the increase in contraction ratio did not present such a severe outcome, and it was found that for a contraction ratio of 25, it was still possible to have a started inlet, which further complied with the necessary criteria for fuel ignition. For this configuration, the increase in contraction ratio was also seen to improve performance, but not necessarily increase the mass flow rate ratio. Lastly, the absence of an expansion corner edge was also considered for the two-dimensional configuration, however a rounded corner was found to increase the separation region and adversely affecting performance.

Finally, operation at an off-design trajectory point corresponding to freestream conditions of Mach 7 was studied. It was found that both the two-dimensional and axisymmetric configurations were able to start at the selected off-design trajectory point, having obtained a total pressure ratio for this trajectory point that was higher than for the design-point Mach number. Contrarily, the remaining performance parameters and particularly the mass flow rate ratio decreased significantly.

6.2 Future Work

Future work should simultaneously try to improve on what has already been developed and move past it. To that end, it is thought that the re-study of a scramjet compression system, within the framework of an appropriate turbulence model is due, given that, for the identified range of operation, the flow is expected to be fully turbulent. It is also expected that, in the presence of a turbulence model, some of the problems that arose due to boundary layer separation will be delayed or even avoided.

An analysis of the drag force that is generated for the different considered geometries, and particularly, a comparison between the axisymmetric and two-dimensional configurations is also thought to present an interesting topic which could build on the already developed work.

As for thematics that have not been addressed in this work, but that can be conducted for the present version of the SPARK code, the study of the remaining scramjet components is recommended, but particularly the study of supersonic combustion. Typical code-validation test cases that are advised to be conducted before the application to a real scramjet problem include the Burrows-Kurkov experiment [37] or the combustion experiments conducted at the German Aerospace Center [38].

Bibliography

[1] J. D. Anderson. *Hypersonic and High-Temperature Gas Dynamics*. AIAA Education Series, 2006. ISBN:978-1563477805.

[2] W. H. Heiser and D. T. Pratt. *Hypersonic Airbreathing Propulsion*. AIAA Education Series, 1994. ISBN:978-1563470356.

[3] J. Lacroze and P. Ricco. *René Leduc. Pionnier de la propulsion à réaction*. Editions Larivière, 2000. ISBN:978-2907051255.

[4] NASA photo. The ramjet: past, present or future? Aérostories, 2000. Retrieved September 30th, 2020, at `http://aerostories.free.fr/constructeurs/leduc/griffonvol.JPG`.

[5] NASA. X-15 photo collection. Dryden Flight Research Center. Retrieved October 1st, 2020, at `https://www.dfrc.nasa.gov/Gallery/Photo/X-15/Small/EC68-1889.jpg`.

[6] U. S. Air Force. X-51a waverider. Retrieved October 2nd, 2020, at `https://media.defense.gov/2010/May/20/2000360693/-1/-1/0/100520-F-9999B-111.JPG`.

[7] R. S. Fry. A century of ramjet propulsion technology evolution. *Journal of Propulsion and Power*, 20(1):27–58, Jan-Feb 2004. doi:10.2514/1.9178.

[8] A. Pauli, H. Alesi, and S. Anderson. The development of the HyShot flight program. In *Jiang Z. (eds) Shock Waves*. Springer, Berlin, Heidelberg, Jan. 2005.

[9] The compression, combustion, and expansion regions of turbojet, ramjet, and scramjet engines. Retrieved October 8th, 2020, at `https://en.wikipedia.org/wiki/Scramjet`.

[10] L. H. Quan, N. P. Hung, L. D. Quang, and V. N. Long. Analysis and design of a scramjet engine inlet operating from Mach 5 to Mach 10. *International Journal of Mechanical Engineering and Applications*, 4(1):11–23, Feb. 2016. doi: 10.11648/j.ijmea.20160401.12.

[11] E. Curran and S. Murthy. *Scramjet Propulsion*. Progress in Astronautics and Aeronautics. American Institute of Aeronautics and Astronautics, 2000.

[12] R. Weber and J. McKay. An analysis of ramjet engines using supersonic combustion. *NACA Technical Note 4386*, Sept. 1958.

[13] J. Urzay. Supersonic Combustion in Air-Breathing Propulsion Systems for Hypersonic Flight. *Annual Review of Fluid Mechanics*, 50(1):593–627, Jan. 2018. doi: 10.1146/annurev-fluid-122316-045217.

[14] D. Andreadis. Scramjet engines enabling the seamless integration of air and space operations. Pratt and Whitney, 2004.

[15] P. M. R. da Costa Simões Gonçalves. Hypersonics: Laying the road ahead. Master's thesis, Instituto Superior Técnico, may 2018.

[16] G. Choubey, L. Suneetha, and K. M. Pandey. Composite materials used in Scramjet - A Review. *International Conference on Processing of Materials, Minerals and Energy*, July 2016. doi: 10.1016/j.matpr.2017.11.217.

[17] M. K. Smart. Scramjet inlets. Centre for Hypersonics, The University of Queensland.

[18] A. Tahsini. Combustion efficiency and pressure loss balance for the supersonic combustor. *Proceedings of the Institution of Mechanical Engineers, Part G: Journal of Aerospace Engineering*, 234 (6):1149–1156, 2019. doi: 10.1177/0954410019895885.

[19] T. A. Heppenheimer. *Facing the Heat Barrier: A History of Hypersonics*. National Aeronautics and Space Administration, 2007.

[20] C. Park. Two-temperature interpretation of dissociation rate data for N_2 and O_2. *26th Aerospace Sciences Meeting*, Jan. 1988.

[21] S. Chapman, T. G. Cowling, and D. Burnett. *The Mathematical Theory of Non-uniform Gases: An Account of the Kinetic Theory of Viscosity, Thermal Conduction and Diffusion in Gases*. Cambridge University Press, 3^{rd} edition, 1970. ISBN:978-0521408448.

[22] G. E. Palmer and M. J. Wright. Comparison of methods to compute high-temperature gas viscosity. *Journal of Thermophysics and Heat Transfer*, 17(2):232–239, 2003. doi: 10.2514/2.6756.

[23] F. G. Blottner, M. Johnson, and M. Ellis. Chemically reacting viscous flow program for multicomponent gas mixtures. Jan. 1971. doi: 10.2172/4658539.

[24] G. Palmer and M. Wright. *A Comparison of Methods to Compute High-Temperature Gas Thermal Conductivity*. doi: 10.2514/6.2003-3913.

[25] A. F. Moura and M. A. P. Rosa. A computer program for calculating normal and oblique shock waves for airflows in chemical and thermodynamic equilibrium. *22nd International Congress of Mechanical Engineering*, Nov. 2013. doi: 10.13140/2.1.1737.0243.

[26] J. C. F. Pereira. *Aerodinâmica Compressível*. AEIST - Instituto Superior Técnico, 2018. Sebenta de Aerodinâmica II.

[27] B. Lopez and M. L. da Silva. SPARK: a Software Package for Aerodynamics, Radiation and Kinetics. *46th AIAA Thermophysics Conference*, June 2016. doi: 10.2514/6.2016-4025.

[28] NASA. U.S. Standard Atmosphere, 1976. *Technical Memorandum NASA-TM-X-74335*, Oct. 1976.

[29] C. M. da Cunha Teixeira. Gas-surface interaction models in hypersonic flows. Master's thesis, Instituto Superior Técnico, dec 2015.

[30] D. M. V. Wie and D. A. Ault. Internal Flowfield Characteristics of a Two-Dimensional Scramjet Inlet at Mach 10. *32nd Aerospace Sclences Meeting and Exhibit*, Jan. 1994. doi: https://doi.org/10.2514/6.1994-584.

[31] R. A. Thompson and P. A. Gnoffo. Application of the LAURA code for slender-vehicle aerothermodynamics. *Journal of Spacecraft and Rockets*, 29(1):16–23, 1992. doi:10.2514/3.26309.

[32] H. Scott D. Mach 10 computational study of a three-dimensional scramjet inlet flow field. Technical report, 1995.

[33] C. Park. Review of chemical-kinetic problems of future NASA missions. I - Earth entries. *Journal of Thermophysics and Heat Transfer*, 7(3):385–398, 1993. doi: 10.2514/3.431.

[34] D. Herrmann, F. Siebe, and A. Gülhan. Pressure fluctuations (buzzing) and inlet performance of an airbreathing missile. *Journal of Propulsion and Power*, 29(4):839–848, 2013. doi: 10.2514/1.B34629.

[35] K. R. Sekar, S. K. Karthick, S. Jegadheeswaran, and R. Kannan. On the unsteady throttling dynamics and scaling analysis in a typical hypersonic inlet–isolator flow. *Physics of Fluids*, 32(12):126104, 2020. doi: 10.1063/5.0032740.

[36] R. Seleznev, S. Surzhikov, and J. Shang. A review of the scramjet experimental data base. *Progress in Aerospace Sciences*, 106:43–70, 2019. doi: 10.1016/j.paerosci.2019.02.001.

[37] M. C. Burrows and A. P. Kurkov. An analytical and experimental study of supersonic combustion of hydrogen in vitiated air stream. *AIAA Journal*, 11(9):1217–1218, 1973. doi: 10.2514/3.50564.

[38] F. Alff, U. Brummund, W. Clauss, M. Oschwald, J. Sender, and W. Waidmann. Experimental investigation of the combustion process in a supersonic combustion ramjet (scramjet) combustion chamber. pages 629–638, 01 1994.

Appendix A

Physical Models

This Appendix complements the mathematical formulation discussed in chapter 3.

A.1 Thermodynamic Relations

A.1.1 Gas Mixture

The composition of a chemically reacting gas mixture may be uniquely described through a series of properties, of which are included the mass fraction, c, and the mole fraction, x.

The mass fraction of a given species, c_s, is given as the mass density of that species ρ_s divided by the mass density, ρ, of the mixture, as given by equation A.1.

$$c_s = \frac{\rho_s}{\rho}. \tag{A.1}$$

The mole fraction of a given species, x_s, is given either as the ratio of the number of moles of that species n_s to the number of moles of the mixture n, or as the number of particles of the species, N_s, divided by the number of particles of the mixture, as given by equation A.2.

$$x_s = \frac{n_s}{n} = \frac{N_s}{N}, \tag{A.2}$$

where the number of moles and number of particles can be related through Avogrado's constant, N_A, as given by equation A.3.

$$N_s = N_A n_s. \tag{A.3}$$

For a given gas mixture, the mass and mole fractions must also obey the relations of equations A.4a and A.4b, respectively.

$$\sum_s c_s = 1, \tag{A.4a}$$

$$\sum_s x_s = 1. \tag{A.4b}$$

Lastly, the mass and mole fractions may be related to one another through the expression of equation A.5, where M_s, as will be recalled, stands for the molar mass of a given species and M stands for the molar mass of the gas mixture.

$$c_s = x_s \frac{M_s}{M}. \tag{A.5}$$

A.1.2 Equation of State

In an hypersonic flow subject to very high temperatures, the molecules are widely spaced apart and intermolecular forces can be neglected, which signifies that the ideal gas assumption may be applied. In light of this, Dalton's Law of partial pressures, given by equation A.6, may be used to relate the pressure of the gas mixture, p, to the partial pressure of each individual species, p_s.

$$p = \sum_s p_s \tag{A.6}$$

The partial pressure of each individual species must also obey the equation of state in any of its forms A.7, where R_s is the specific gas constant of a given species, R is the universal gas constant, and k_B is the Boltzmann constant.

$$p_s = \rho_s R_s T_{\text{trans},s}, \tag{A.7a}$$

$$p_s V = N_s k_B T_{\text{trans},s}, \tag{A.7b}$$

$$p_s V = n_s R T_{\text{trans},s}. \tag{A.7c}$$

Furthermore, the specific gas constant is given as function of the universal gas constant, according to equation A.8.

$$R_s = \frac{R}{M_s}. \tag{A.8}$$

A.1.3 Internal Energy

The internal energy per unit mass e, of a single-species s, was defined, in equation 3.5 as the sum of the internal energy associated with each thermal energy mode, with the effective zero-point energy of the species.

The set of equations A.9 presents the mathematical expressions used to determine the internal energy for the translational, rotational and vibrational thermal modes, where for this case, h exceptionally refers to Planck's constant and ω_{e_s} is the fundamental vibrational frequency of a given species [1].

$$e_{\text{trans},s} = \frac{3}{2} R_s T_{\text{trans},s}, \tag{A.9a}$$

$$e_{\text{rot},s} = R_s T_{\text{rot},s}, \tag{A.9b}$$

$$e_{\text{vib},s} = \frac{h\omega_{e_s}/k_B T_{\text{vib},s}}{\exp\left(h\omega_{e_s}/k_B T_{\text{vib},s}\right) - 1} R_s T_{\text{vib},s}. \tag{A.9c}$$

For the electronic thermal mode, no simple expression can be given [1], and therefore it will continue to be denoted simply as $e_{\text{el},s}$.

Finally, the internal energy of the gas mixture is given as the sum of the internal energy for the different species present, according to equation A.10.

$$e = \sum_s c_s e_s. \tag{A.10}$$

A.1.4 Enthalpy

The enthalpy of a given species is defined in a similar manner to the internal energy, as a sum of the enthalpy associated with each thermal mode (equation A.11).

$$h_s = h_{\text{trans},s} + h_{\text{rot},s} + h_{\text{vib},s} + h_{\text{el},s} + (\Delta \mathsf{h}_s)^\circ. \tag{A.11}$$

Which can be written as a function of the internal energy, according to equation A.12.

$$h_s = e_{\text{trans},s} + R_s T_{\text{trans},s} + e_{\text{rot},s} + e_{\text{vib},s} + e_{\text{el},s} + (\Delta \mathsf{h}_s)^\circ. \tag{A.12}$$

Lastly, the enthalpy of the gas mixture, is given as a sum of the enthalpy for the different species present, according to equation

$$h = \sum_s c_s h_s. \tag{A.13}$$

A.1.5 Specific Heats

The gas specific heat at constant volume or at constant pressure is defined as the rate of change of internal energy with temperature or the rate of change of enthalpy with energy, respectively (set of equations A.14).

$$c_v = \left(\frac{\partial e}{\partial T}\right)_V, \tag{A.14a}$$

---

[1] Assuming an harmonic oscillator distribution for the vibrational levels.

$$c_p = \left(\frac{\partial h}{\partial T}\right)_p . \tag{A.14b}$$

However, and as previously discussed, both internal energy and enthalpy are a function of the different thermal modes, which results in the set of equations A.15.

$$c_v = \sum_k c_{v\,k} = \sum_k \left(\frac{\partial e_k}{\partial T_k}\right), \tag{A.15a}$$

$$c_p = \sum_k c_{p\,k} = \sum_k \left(\frac{\partial h_k}{\partial T_k}\right). \tag{A.15b}$$

Applying the previous definitions of e and h, results then, for thermal mode k of a given species, on the set of equations A.16.

$$c_{v\,k} = \sum_s \left(c_s \frac{\partial e_{k,s}}{\partial T_{k,s}} + e_{k,s} \frac{\partial c_s}{\partial T_{k,s}}\right), \tag{A.16a}$$

$$c_{p\,k} = \sum_s \left(c_s \frac{\partial h_{k,s}}{\partial T_{k,s}} + h_{k,s} \frac{\partial c_s}{\partial T_{k,s}}\right). \tag{A.16b}$$

For a frozen flow, the mass fractions of each species does not vary and equation A.17 is valid.

$$\frac{\partial c_s}{\partial T_{k,s}} = 0. \tag{A.17}$$

This simplifies the expressions for the specific heats of different thermal modes into the set of equations A.18.

$$c_{v\,k} = \sum_s \left(c_s \frac{\partial e_{k,s}}{\partial T_{k,s}}\right), \tag{A.18a}$$

$$c_{p\,k} = \sum_s \left(c_s \frac{\partial h_{k,s}}{\partial T_{k,s}}\right). \tag{A.18b}$$

Finally, and once more in light of the previously defined equations for the internal energy and enthalpy with respect to the different thermal modes, it is possible to write the specific heats for the different the translational and rotational modes as the set of equations A.19 for the specific heat at constant volume and the set of equation A.20 for the specific heat at constant pressure.

$$c_{v\,\text{trans},s} = \frac{3}{2} R_s, \tag{A.19a}$$

$$c_{v\,\text{rot},s} = R_s. \tag{A.19b}$$

$$c_{p\,\text{trans},s} = \frac{5}{2} R_s, \tag{A.20a}$$

$$c_{p_{\text{rot},s}} = R_s. \tag{A.20b}$$

The above expressions yield, for a calorically perfect gas a ratio of specific heats $\gamma = 1.4$.

A.1.6 Gas Constants

Lastly, it is possible to write the species gas constant or the universal gas constant as a function of the previously described specific heats, according to the set of equations A.21.

$$R_s = c_{p_{\text{trans},s}} - c_{v\text{trans},s}, \tag{A.21a}$$

$$R_u = c_p - c_v. \tag{A.21b}$$